Development of Mid-Infrared Coherent Sources Based on Novel Nonlinear Devices

by

Melisa Natali Çizmeciyan Sözüdoğru

A Thesis Submitted to the
Graduate School of Engineering
in Partial Fulfillment of the Requirements for
the Degree of

Doctor of Philosophy
in
Materials Science and Engineering

Koç University

August 2014

Koç University

Graduate School of Sciences and Engineering

This is to certify that I have examined this copy of a doctor of philosophy thesis

by

Melisa Natali Çizmeciyan Sözüdoğru

and have found that it is complete and satisfactory in all respects,

and that any and all revisions required by the final

examining committee have been made.

Committee Members:

Alphan Sennaroğlu, Ph. D. (Advisor)

Menderes Işkın, Ph. D.

Funda Yağcı Acar, Ph. D.

Coşkun Kocabaş, Ph. D.

Sarper Özharar, Ph. D.

Date:

ABSTRACT

This thesis investigates the development of an efficient and robust femtosecond laser which produces mid infrared pulses by employing different mode locking techniques. In particular, Kerr lens mode locking and graphene saturable absorber mode locking techniques were successfully applied to the Cr:ZnSe laser which operates around 2.45 μm. In the second part of the thesis, linear and non-linear optical properties of a gated graphene based supercapacitor were experimentally characterized, and voltage dependent optical and ultrafast properties were discussed.

The first part of the thesis is the demonstration of a Kerr lens mode-locked Cr:ZnSe laser and evaluation of the performance of four different cost-effective and practical dispersion compensation methods. The highest pulse energy was obtained with a 6% output coupler and a CaF_2 prism pair, where as high as 1.81 nJ was obtained with 2 W of pump power. When a 1% output coupler was used with the CaF_2 prism pair, higher intracavity energy led to the generation of pulses as short as 92 fs. Based on the mode locking parameters of the laser, the nonlinear refractive index (n_2) of ZnSe was estimated as $(1.2\pm0.2)\times10^{-18}$ m^2/W by using the soliton area theorem.

The second part of the thesis involves the demonstration of graphene saturable absorber mode-locked operation of a stable femtosecond Cr:ZnSe laser. The laser produced 176-fs pulses at a repetition rate of 78 MHz with an average power of 80 mW. The measured time-bandwidth product was 0.39 with a 3% output coupler. With a 6% output coupler, 2.4-nJ, 200-fs pulses were generated near 2.4 μm at a pulse repetition frequency of 78 MHz. The average mode-locked output power was 185 mW. This work was the first demonstration of a femtosecond Cr:ZnSe laser passively mode locked with a graphene saturable absorber.

The third part of the thesis focuses on the optical characterization of graphene samples grown on quartz, YAG and CaF$_2$. We determined the saturation fluence and modulation depth of the samples as 34 μJ/cm^2 and 0.6%, 60 μJ/cm^2 and 0.8%, 39 μJ/cm^2 and 0.6% for graphene on quartz, YAG and CaF$_2$, respectively. The final part is the linear and non-linear characterization of the optical properties of a voltage controlled saturable absorber based on graphene super capacitors. Pump-probe measurements revealed that the ultrafast response of the graphene has similar dynamics with an average fast and slow time constants of 283 fs and 1.9 ps up to 1V of applied voltage. The saturation fluence at 1250 nm monotonically increases with the applied bias, becoming 456 μJ/cm^2 at 1V and the modulation depth decreases from 1.09% at 0V to 0.69% at 1V. Hence, the modulation depth of the device was adjusted in the range of 1.1-0.7%.Our results indicate that, utilization of cost effective dispersion techniques as well as novel saturable absorbers such as graphene will lead to the development of practical sources of mid-infrared femtosecond pulse sources suitable for spectroscopic, medical and nonlinear optical applications.

ÖZET

Bu doktora tezinde farklı kip kilitleme teknikleri kullanılarak geliştirilen, kızıl altı bölgesinde çalışan ve femtosaniye süreli darbeler üreten bir laser geliştirilmiştir. Deneylerde Kerr odaklamalı kip kilitleme ve doyabilen soğurucu vasıtasıyla elde edilen kip kilitleme yöntemleri Cr:ZnSe laserine başarıyla uygulanmıştır. Tezin ikinci bölümünde, grafen tabanlı üretilen süper kapasitör yapısına sahip ve optik özellikleri uygulanan voltaj ile değiştirilebilen bir doyabilen soğurucunun doğrusal ve doğrusal olmayan optik özellikleri incelenmiştir.

Tezin ilk bölümünde, Kerr odaklamalı kip kilitleme yöntemi kullanılarak çalıştırılan Cr:ZnSe laserinin farklı dispersiyon kaynakları kullanılarak çalıştırılması gösterilmiştir. Laserden elde edilen en yüksek darbe enerjisi 1.8 nJ olup, %6 geçirgenliğe sahip çıkış aynası ile CaF_2 malzemesinden yapılmış prizma çifti ile elde edilmiştir. Laser %1 çıkış aynası ile çalıştırıldığında elde edilen darbe uzunluğu 92 fs olarak ölçülmüştür. Kip kilitleme deneylerinden elde edilen değerler kullanılarak Cr:ZnSe malzemesinin doğrusal olmayan kırılma indisi $(1.2\pm0.2)\times10^{-18}$ m^2/W olarak hesaplanmıştır. Aynı laser düzeneği bu sefer grafen kullanılarak kip kilitli rejimde çalıştırılıp femtosaniye süreli darbeler başarıyla üretilmiştir. Laserden, %3 geçirgenliğe sahip çıkış aynası kullanılarak, 78 MHz darbe tekrar frekansında, 176 fs süreli ve 80mW ortalama güce sahip kararlı darbeler elde edilmiştir. Çıkış aynası geçirgenliği %6 olduğunda, laserin çıkışında elde edilen darbe enerjisi 1.4 nJ'den 2.4 nJ'e yükselmiştir. Grafen kullanılarak kip kilitli rejimde çalıştırılan Cr:ZnSe laseri, literatürde bu yöntemle çalıştırılmış en uzun dalgaboyuna sahip laserdir.

Tezin sonraki bölümünde farklı alttaşlar (kuvartz, YAG ve CaF_2) üzerine kaplanmış grafen örnekleri, optik yöntemler kullanılarak karakterize edilmiştir. Bu örnekler için belirlenen doyum akısı ve modülasyon derinliği kuvartz için 34 $\mu J/cm^2$ /%0.6, YAG için 60 $\mu J/cm^2$ %0.8, ve son olarak CaF2 için 39 $\mu J/cm^2$ %0.6 olarak belirlenmiştir. Bu bölümün devamında voltaj ayarlamalı grafen süperkapasitör cihazın doğrusal ve doğrusal olmayan optik özellikleri araştırılmıştır. Pompa sonda yöntemi kullanılarak yapılan ölçümlerde, cihazın yaşam süresinin voltaja çok bağımlı olmadığı gözlenmiştir ve yaşam süresi ortalama 1.9 ps olarak ölçülmüştür. Cihazın doyum akısının, uygulanan voltajla monotonik olarak artış gösterdiği ve uygulanan voltaj 1V olduğunda en fazla 456 $\mu J/cm^2$ değerine çıktığı saptanmıştır. Uygulanan voltaj aralığında (0-3V), cihazın modülasyon derinliği %1.1 ile %0.7 değer aralığında ölçülmüştür. Bu tez çalışmasında geliştirilen ucuz dispersiyon dengeleme teknikleri ve grafen tabanlı kip kilitleme yöntemleri sayesinde, kızılatı bölgesinde darbe üretebilen ve birçok tıbbi ve spektroskopik uygulamada kullanılabilecek pratik femtosaniye darbe kaynaklarının geliştirilebileceğini öngörmekteyiz.

ACKNOWLEDGEMENTS

This part of my thesis is dedicated to honor the support of the people who had contributed in composing this thesis work. In this sense, I would like to mention a couple of names starting with my mentor, thesis advisor Prof. Alphan Sennaroğlu. It has been almost ten years since we met, during this time he was like a father to me. He constantly looked for the best interest in developing my career. He has always been an excellent role model in terms of his honest and ethic approach to everything. Similarly, I have to mention Adnan Kurt due to providing his endless experience on building electronic devices or any device. He assisted me in building and calibrating the scanning mid-infrared spectrometer, and controlling the temperature controlled cuvette holder, and many more. Besides, he is a great partner at coffee breaks where he taught us to look at things with different aspects. I also would like to thank Dr. Hüseyin Çankaya, in particular during the development of the femtosecond Cr:ZnSe laser, due to the helpful discussions on the femtosecond operation of lasers. I also have to mention Işınsu Baylam for the discussions that we had on the graphene work which extended my level of understanding the physical background of this fascinating material. Last but not least, my lab friends, Ferda Canbaz, Ersen Beyatlı, Can Cihan, Ismail Yorulmaz, have shown continuous support throughout the years. I also would like to thank Ibrahim Hocaoğlu, Hande Öztürk, Emre Polat who prepared some of the samples that were used in this thesis.

Funda Yağcı Acar, Menderes Işkın, Sarper Özharar from Bahçeşehir University and Coşkun Kocabaş from Bilkent University deserve special thanks as my thesis committee members. Their valuable comments helped me a lot during the revision of this thesis.

In this thesis work, we have collaborated with three groups: graphene sample on CaF_2 substrate from South Korea in collaboration with Prof. Fabian Rotermund, gated graphene sample from Bilkent University in collaboration with Dr. Coşkun Kocabaş, and near-Infrared emitting quantum dots in collaboration with Funda Yağcı Acar from the Chemistry

Department of Koç University. Without the support of our collaborators, it would not have been possible to realize our ideas.

Finally, I would like to thank the graduate school of science and engineering for providing the scholarship from Vehbi Koç Foundation which allowed me to carry out my research and gave me the opportunity to attend conferences. Part of this thesis work has been generously sponsored by Tübitak under the project 108T028 titled “Development of a High-Energy, Cr^{2+}:ZnSe Laser Pulse Amplifier at 2400 nm”.

Lastly I would like to thank to my parents and my husband who have been constantly supporting me all these years. Don't worry, no more schools!

Table of Content

List of Tables

List of Figures

Nomenclature

σ_a: Absorption cross-section
ω: Angular frequency
ω_0: Beam waist spotsize
L_R: Cavity length
τ_P: Cavity photon lifetime
λ_0: Central wavelength
β: Chirp parameter
L_C: Crystal length
A_{eff}: Effective area
E: Electric field amplitude
σ_e: Emission cross-section
N_2: Excited state population density
α: Fine structure constant
v_F: Fermi velocity
ν_P: Frequency of pump photons
ν_L: Frequency of laser photons
g: Gain
Ω_g: Gain bandwidth
N_1: Ground state population density
D: Group velocity dispersion (GVD)
τ_0: Initial pulsewidth
δ: Kerr coefficient
ω_L: Laser beam waist
I_L: Laser intensity
P_L: Laser power
P_{peak}: Peak power
φ_0: Phase
v_P: Phase velocity
h: Planck's constant
ΔN: Population inversion
P: Power
W: Pulse energy
τ_P: Pulsewidth
ω_P: Pump beam waist
I_P: Pump intensity
f_{rep}: Repetition rate
L_R: Resonator length
T_R: Roundtrip time
E_{sat}: Saturation energy
P_{sat}: Saturation power
J_{sat}: Saturation fluence
γ: Self amplitude modulation (SAM)
L_P: Separation between two prisms
η: Slope efficiency
g_0: Small signal gain
G_0: Small signal fractional power
η: Slope efficiency
L_S: Substrate length
c: Speed of light
G_s: Steady-state gain

L: Loss
ΔT: Modulation depth
T_{ns}: Non saturable loss
ΔA: Nonlinear absorbance
n_2: Nonlinear refractive index
N: Number of longitudinal modes
Z: Optical path
G_{th}: Threshold gain
P_{th}: Threshold power
T: Transmission
λ: Wavelength
k: Wave number

Chapter 1: Introduction

1.1 Near and Mid-Infrared Laser Applications

Nowadays there are many emerging applications, which require lasers to operate in the near- and mid-infrared portion of the electromagnetic spectrum, in many fields ranging from bio-medicine to spectroscopy and military applications. Near-infrared light sources have been extensively researched throughout the years and have been developed into well-established commercial products. However, in the case of the mid-infrared light sources, because of a lack of awareness together with the limited resources, it took longer for this field to gain attention. Soon after the first demonstration of optical frequency combs [1], the field of high-resolution molecular spectroscopy was revolutionized [2-5]. Especially the idea of making precise and real-time measurements in the molecular finger print region stimulated the development of ultrafast mid infrared laser sources based on non-linear optical conversion methods and direct generation of femtosecond pulses from solid state and fiber lasers [6-10]. Numerous applications are emerging, which are linked to the development of such sophisticated laser sources. Some of them are high harmonic generation [11-14], atmospheric gas sensing [15] and detection of hazardous gases [16-18].

The first frequency comb operating in optical frequencies was demonstrated in 1999 which led to the Nobel prize in 2005 [1]. Optical frequency combs based on mode-locked ultrafast lasers, generate thousands of evenly distributed sharp spectral components over a broad range, which are frequency calibrated. In other words, it can be regarded as an optical ruler. Use of optical frequency combs in the field of spectroscopy provides not only a broadband spectrum with high spectral resolution but also allows simultaneous, real-time data acquisition. Frequency combs based on mid-infrared laser sources are more advantageous in comparison with their visible or near-infrared counterparts which can only detect the overtone signals of the fundamental transitions with considerably lower excitation and emission efficiencies [19]. Figure 1.1.1 is direct evidence that most of the transitions of well-known substances occur at mid-infrared. Accordingly, this region is named the “finger print region” of molecules.

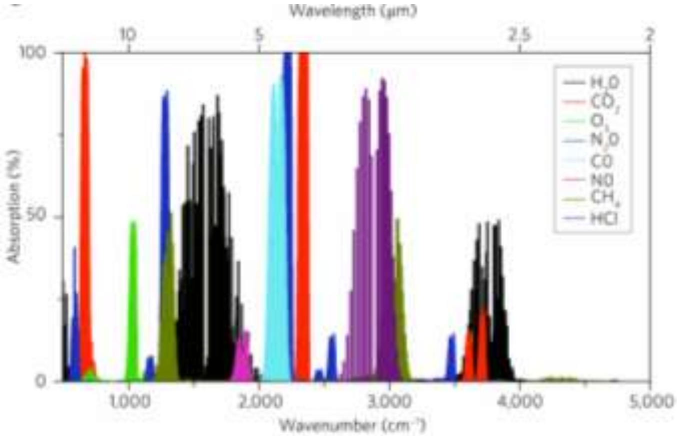

Figure 1.1.1: Absorption spectrum of some common gases in 2-15 μm region [20].

Operation wavelength of an optical frequency comb can be extended into mid-infrared through nonlinear optical conversion methods, difference frequency generation (DFG) [21], optical parametric oscillators (OPO) [7] or micro-resonator Kerr combs [22], or direct generation of femtosecond pulses from a frequency stabilized mid-infrared solid-state and fiber lasers (see Section 1.2 for a detailed description) [20]. It has been shown that the sensitivity of the spectroscopic measurement can be dramatically improved by coupling the output of optical frequency comb into a high finesse optical enhancement cavity, which contains the sample of interest. Cavity-enhanced direct frequency comb spectroscopy (CE-DFCS) is now used in the direct measurement of the rotational and vibrational transitions of molecules and it allows the detection of very small quantities in real time measurements [23].

Another potentially important application of ultrashort-pulsed mid-infrared lasers is the high harmonic generation (HHG) where coherent harmonics in the soft x-ray region are obtained by focusing intense laser pulses into a gas jet. As a result of the theoretical predictions, the spectral cutoff energy of the generated harmonics are strongly dependent on the center wavelength of the driving field [12]. Experimental results confirm that in comparison with near-infrared sources, use of mid-infrared sources has the potential of increasing the cut-off energy of the x-ray photons generated or attaining a particular cut-off energy with relatively lower excitation intensities. In a recent study, output of an infrared frequency comb is converted to deep ultraviolet (UV) light by means of high harmonic generation (HHG). They focused the high output power of Yb:fiber based frequency comb into a femtosecond enhancement cavity [24] and obtained harmonics at wavelengths as short as 40nm. As a result, they successfully measured the absolute transition of argon and neon atoms at 82nm and 63nm, respectively. [13].

1.2 Mid-Infrared Laser Sources

1.2.1 Nonlinear optical conversion methods

Due to recent advancements in the high-resolution molecular spectroscopy field, different approaches to generate mid-infrared femtosecond pulses have emerged to build frequency combs which also operate in the mid-infrared. As it was mentioned in the earlier section, nonlinear optical conversion methods such as difference frequency generation (DFG), optical parametric oscillation (OPO), micro-resonator Kerr combs, and direct generation from solid-state lasers are effectively used to produce femtosecond mid-infrared pulses. Figure 1.2.1 [20] illustrates the spectral coverage comparison of these methods. Although all the spectral coverage ranges seem similar, power per mode values differ dramatically. Depending on the application of interest, each technique has its own advantages and disadvantages. For example among these alternatives, the spectral coverage of DFG is the largest, however delivered power per mode is relatively low compared to the other techniques.

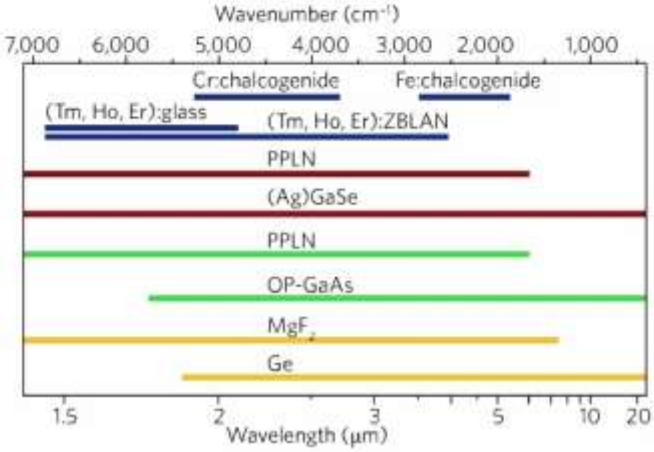

Figure 1.2.1: Wavelength coverage of different approaches to generate mid-infrared femtosecond pulses. Blue, red, green and yellow represents solid state lasers, DFG, OPO and micro-resonator based Kerr combs, respectively [20].

It has been shown that DFG can be utilized to convert the operation wavelength of a near infrared optical frequency comb to mid-infrared where the output of a near infrared frequency comb is combined with a continuous wave (cw) laser in a phase matched nonlinear crystal. Each spectral component of the comb undergoes DFG with the cw laser mode. Depending on the operation frequency of the cw laser the output can be tuned in the mid-infrared region as long as the phase matching condition is met. Spectral coverage of two nonlinear crystals, namely periodically poled lithium niobate (PPLN) and gallium selenide (GaSe) is shown in Figure 1.2.1 with red color. Although PPLN delivers a better average output power compared to the GaSe, the intrinsic absorption of PPLN restricts the access at longer wavelengths [25]. Figure 1.2.2 shows the operation ranges of both GaSe and PPLN nonlinear crystals where use of GaSe extends the long wavelength edge up to 10 μm.

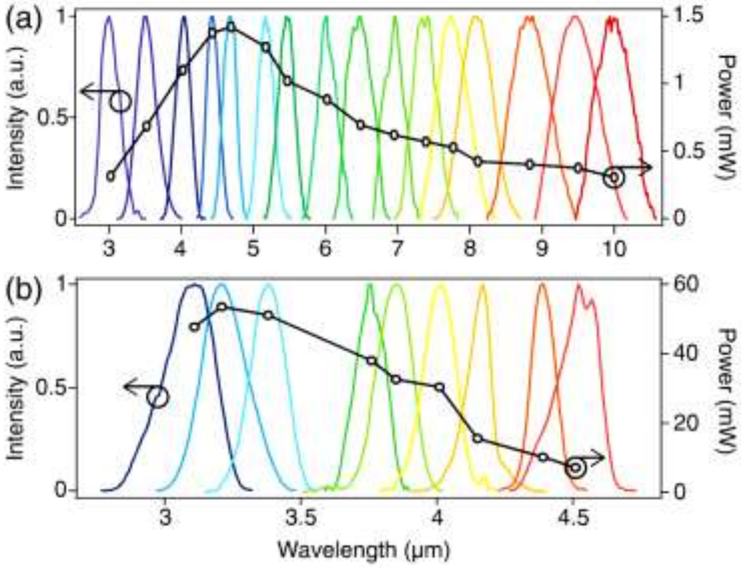

Figure 1.2.2: Tuning range comparison between PPLN and GaSe based DFG setups, where (a) GaSe (b) PPLN case [25].

In the case of optical parametric oscillators (OPO), the frequency of pump photons is divided as the signal and the idler, depending on the phase matching condition. For example, in order to obtain 1560nm output from a KTP based OPO, it is pumped with a 1064 nm laser where the idler has the wavelength around 3350 nm. Spectral coverage of PPLN [10] and orientation patterned gallium arsenide (OP-GaAs) [7] nonlinear crystals are shown in Figure 1.2.1 with green color. Broadest operation range was reported as 2.6 to

6.1 μm [7]. Even though the operation range of OPO systems seems limited compared to DFG, it delivers higher output power per mode.

1.2.2 Direct solid-state laser sources

The methods explained in the earlier section use nonlinear optical conversion techniques which usually have very low conversion efficiencies, i.e. 1-2% for DFG and around 40% for OPOs. One alternative is the direct generation of femtosecond pulses from a solid-state or fiber laser [26] to enhance the delivered power per mode. Because the subject of this thesis is the femtosecond Cr:ZnSe lasers, first I would like to provide a historical overview about the developments in this field.

The first mid-infrared solid-state laser source was a pulsed uranium doped calcium fluoride laser (U:CaF_2) which was operating at 2.6 μm [27]. Until 1963 rare earth active ions were preferred to provide optical gain, which was later replaced with vibronically broadened transition metal ions. Electronic transitions of these materials are strongly coupled to lattice phonons, in other words, gain medium supports larger gain bandwidth which enables tunable laser operation. The first tunable vibronic mid-infrared lasers were Ni:MgF_2, and Co:MgF_2, where the broadest tuning was achieved from 1.63 μm to 2.08 μm for Co:MgF_2 laser [28]. At the time, people faced two main challenges: i) the gain crystals had low emission cross-section which necessitated cryogenic cooling; ii) flashlamp pumping scheme was inefficient due to losing excess amount of energy to the non-radiative decay routes, which caused over heating of the gain medium. In 1978 Moulton's group proposed to use laser pumping scheme which improved the over-heating of the gain crystals and provided a much higher power conversion efficiency. Consequently, the first tunable and continuous-wave mid-infrared laser which operates at 200K temperature was demonstrated and tuned between 1.63μm and 1.75μm [29]. For a long time, the most popular mid-infrared tunable laser was cryogenically cooled Co:MgF_2, until DeLoach and co-workers proposed that tetrahedral ZnSe crystal structure provides higher transition probabilities than the octahedral fluorides. Based on the careful spectroscopic studies they performed on numerous combinations of hosts (ZnS, ZnSe and ZnTe) and dopants (Cr, Co, Ni and Fe), they concluded that chromium doped zinc selenide/sulfide (Cr:ZnSe/ZnS) were the most promising combination for room temperature operation [30, 31]. The ZnSe crystal has an emission cross-section of $90\text{x}10^{-20}\text{cm}^2$ [30], and a thermal conductivity of 18W/m.°C [32]. Additionally, its low excited state absorption cross section enables efficient pumping of the crystal [33]. As a result, the first laser operation of Cr:ZnSe as a laser gain medium was demonstrated in 1996 [31]. The only disadvantage is the fact that dn/dT value of Cr:ZnSe is relatively high ($70\text{x}10^{-6}$/K) which leads to thermal lensing inside the gain medium [32]. However, a passive water-cooling of the crystal is sufficient to eliminate possible thermal effects. The broadest continuous-wave tuning range was obtained from 1.97 μm to 3.35 μm range for Cr:ZnSe and from 1.96 to 3.20 μm for Cr:ZnS at less than 10 GHz linewidth [34]. Broad gain bandwidth of Cr:ZnSe/ZnS lasers allow the direct generation of femtosecond pulses. The first mode locking results were obtained with the Cr:ZnSe laser. An active mode locking technique called acousto-optic mode locking, generated 4.4 ps pulses with MHz repetition rate [35]. Theoretical models suggest that careful dispersion management inside the laser cavity may lead to further pulse shortening. As a result the first dispersion compensated semiconductor saturable absorber mode locked Cr:ZnSe laser produced pulses around 100fs [36]. After the first demonstration, other mode locking techniques were successfully applied to the laser by using Kerr effect [37, 38] and graphene as a saturable absorber [39]. Parallel to the developments in Cr:ZnSe, similar results were obtained for Cr:ZnS as well. First tunable cw operation was reported in 2002, it was tuned from 2.19 μm to 2.47 μm [40]. Kerr lens mode locking, [41] semiconductor saturable absorber mode locking [42] and recently graphene saturable absorber mode locking [43] were demonstrated, and pulses as short as 41fs were produced from the graphene mode-locked Cr:ZnS laser.

Another spectral region of interest is covered by iron doped zinc selenide (Fe:ZnSe) laser which operates in the range of 3-5 micron wavelength. Although the laser transition energy gap is relatively small and allows multi phonon quenching, by using cryogenic cooling, the first laser operation was demonstrated in 1999 [44]. Following the first gain switched operation at cryogenic tempertures, room temperature pulsed operation was obtained and the output of the laser was tuned from 3.9-4.5 μm [45]. Even though it has a broad gain bandwidth, and operated in cw regime [46], due to practical issues, to date, it has not been possible to generate femtosecond pulses with Fe:ZnSe lasers.

1.3 Scope of the Thesis

This thesis work consists of five chapters titled as Introduction, Theoretical Background, Development of the Femtosecond Cr:ZnSe Laser, Non-Linear Optical Characterization of Graphene, and finally the Collaborative Works, which were done with our group members and other groups. The theoretical background chapter includes the concepts of optical gain, loss, and threshold pump power, and proposed theoretical models behind the operation of continuous wave lasers. In the following section, theory of mode locking by using two widely used techniques, called the Kerr-lens and saturable absorber mode locking, will be outlined. The final section of the theoretical background chapter continues with the introduction of transient absorption spectroscopy method. In Chapter 3, after a brief introduction to the Cr:ZnSe lasers, the demonstration of Kerr lens mode locked and graphene mode locked operation of the laser will be described by providing experimental data. By using this experimental data, the nonlinear refractive index of Cr:ZnSe will be estimated. Chapter 4 begins with a detailed introduction to linear and non-linear optical properties of graphene, and continues with the spectroscopic characterization, including the optical transmission measurements, Raman spectroscopy measurements, pump-probe measurements, saturation measurements of non-gated graphene samples transferred on quartz, YAG, and CaF_2 substrates and a gated supercapacitor based graphene sample.

Optically characterized YAG and quartz samples were successfully utilized as a saturable absorber in mode locking of a Cr:forsterite laser in collaboration with Isinsu Baylam. The graphene samples transferred on quartz and YAG substrate together with the gated supercapacitor graphene were prepared in collaboration with Dr. Coskun Kocabas from Bilkent University, the graphene transferred on CaF_2, which is also used in the mode locking experiments, was prepared in collaboration with Dr. Fabian Rotermund from South Korea. In the last chapter, some of the collaborative works done in collaboration with Dr. Funda Yağcı Acar from Koç University Chemistry Department, and other group members from Laser Research Laboratory (LRL) will be summarized.

Chapter 2: Theoretical Background

2.1 Continuous-wave laser operation

A typical solid state laser system consists of three essential components: gain medium, pumping mechanism, and feedback mechanism. The pumping mechanism excites the atoms to excited states and creates a population inversion in the gain medium. A resonator is then required to provide feedback to initiate oscillation based on stimulated emission. Depending on the output characteristics, lasers show two distinct operation regimes known as continuous wave (cw) and pulsed operation. In the cw regime, the output power of the laser is constant over time. However, in pulsed operation, the output power is a function of time, which has a certain repetition rate, pulsewidth, and pulse energy. Pulsed operation will be discussed in detail in Section 2.2.

In Section 2.1.1, the ideal 4-level system will be introduced and a theoretical model will be developed to show the advantages of having a 4-level laser material as a gain medium. In Section 2.1.2, conditions to achieve laser operation will be discussed and an analytic equation for threshold power estimation will be derived for Gaussian beams.

2.1.1 Modeling of gain mechanism

When we look at the energy level diagrams of typical rare earth or transition metal elements, the lowest energy level is called the ground state. Resonant absorption of photons can lead to transitions to higher lying excited states. In an ideal 4-level system, additional metastable states, which are very short lived, are formed close to both ground and excited states. Figure 2.1.1 represents an ideal 4-level atomic system, where $N_0, N_1, N_2,$ and N_4 are the population densities of the given energy levels. For the ideal case, in order to initiate amplification by stimulated emission, the population density at the excited energy level has to be greater than that of the ground state. The population difference between these states is called population inversion and is denoted as ΔN.

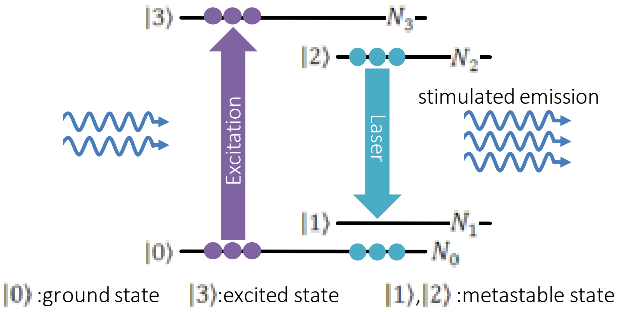

Figure 2.1.1: Energy level diagram of an ideal 4-level laser system.

Under monochromatic pumping, the rate of change for the upper state population (N_2) can be written in the presence of pumping, absorption, spontaneous, and stimulated emission as

$$\frac{dN_2}{dt} = W_P N_0 - \sigma_e \frac{I}{h\nu} N_2 + \sigma_a \frac{I}{h\nu} N_1 - \frac{N_2}{\tau_f}. \qquad 2.1.1$$

Here, W_P is the pumping rate, σ_a is the absorption cross section, σ_e is the emission cross-section, and τ_f is the fluorescence lifetime. Now, assume that absorption and emission cross sections are equal $(\sigma_a = \sigma_e = \sigma)$, and because of short lived metastable states: $N_3 = N_1 \approx 0$. Then, Eqn 2.1.1 simplifies to:

$$\frac{dN_2}{dt} = W_P N_0 - \sigma \frac{I}{h\nu} (N_2 - N_1) - \frac{N_2}{\tau_f}. \qquad 2.1.2$$

When we rewrite Equation 2.1.1 by substituting $N_0 = N_t - N_2$ and $N_2 = \Delta N$, we obtain the following equation:

$$\frac{dN_2}{dt} = \Delta N\left(-\sigma\frac{I}{h\nu} - W_p - \frac{1}{\tau_f}\right) + W_P N_t = 0. \tag{2.1.3}$$

Steady state solution of the rate equation provides us the small signal population inversion and saturation intensity as:

$$\Delta N_0 = \frac{N_t W_P \tau_f}{1 + W_P \tau_f}, \tag{2.1.4}$$

and,

$$I_s = \frac{h\nu}{\sigma\tau_f}\left(1 + W_P\tau_f\right). \tag{2.1.5}$$

Figure 2.1.2 compares 3-level and 4-level laser systems in terms of the small signal population inversion formulas derived in ref [47]. It clearly shows that under similar pumping, 4-level systems always have positive population inversion.

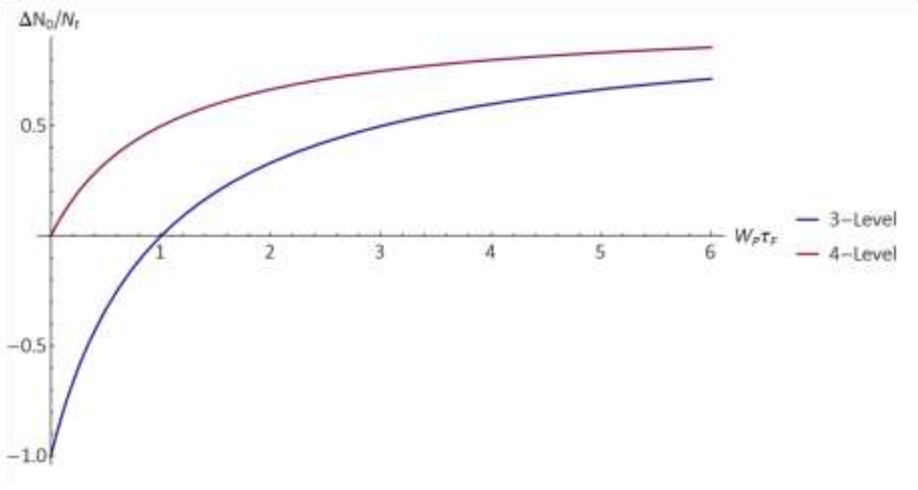

Figure 2.1.2: Change of small signal population inversion for 3- and 4- level laser systems as a function of the pumping rate.

2.1.2 Laser threshold

In the previous section, we concluded that a 4-level laser material always has positive population inversion when it is pumped with an external source. However, having positive population inversion does not guarantee gain. In order to achieve amplification, the gain has to exceed the losses coming from different sources in the cavity, such as scattering losses, reflection losses, and parasitic absorption losses. In Equation 2.1.4, increasing pumping rate (W_P) results in a larger population inversion. The laser threshold is reached when gain resulting from the population inversion is equal to the material and cavity losses. Figure 2.1.3 illustrates a hypothetical gain medium with thickness of dz and area of A.

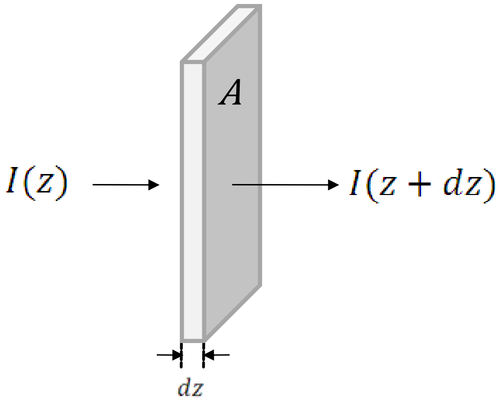

Figure 2.1.3: Hypothetical gain medium with thickness of dz and area of A.

The number of photons that leads to laser emission is

$$\frac{(I_L(z+dz)-I_L(z))A}{h\nu_L} = (N_2)\left(\frac{\sigma_e I_L}{h\nu_L}\right)(Adz). \qquad 2.1.6$$

Since the intensity is defined as the power per unit area, the fractional change in the beam power is given by

$$g = \frac{\Delta P_L}{P_L} = \frac{(I_L(z+dz)-I_L(z))A}{I_L A} = N_2\sigma_e L_C \qquad 2.1.7$$

where L_C is the length of the gain medium and P_L is the laser power.

It can be shown that G and P_L satisfy the following coupled differential equations [47]

$$\frac{dG}{dt} = -\frac{G(t) - G_0}{\tau_f} - \frac{P_L(t)G(t)}{E_{sat}} \tag{2.1.8}$$

and

$$\frac{dP_L}{dt} = \frac{2G(t)}{T_R} P_L(t) - \frac{1}{\tau_P} P_L(t). \tag{2.1.9}$$

Above, the roundtrip time (T_R), cavity photon lifetime (τ_P), small-signal fractional power gain (G_0) and, the saturation energy (E_{sat}) are given by the

$$T_R = \frac{2L_R}{c}, \tag{2.1.10}$$

$$\tau_P = \frac{2L_R/c}{2\alpha_L L_C + \frac{1}{2}\ln\frac{1}{R_1 R_2}}, \tag{2.1.11}$$

$$G_0 \approx \frac{\sigma_a I_P N_t}{h\nu_P} \sigma_e d_g \tau_f \tag{2.1.12}$$

and

$$E_{sat} = \frac{h\nu_L}{\sigma_e} A \tag{2.1.13}$$

respectively. Steady state solution of Eqn. 2.1.9 $\left(\frac{dP_L}{dt} = 0\right)$ at threshold gives the following relation for the threshold value of the fractional gain:

$$G_{th} = \frac{T_R}{2\tau_P}. \tag{2.1.14}$$

When the above definitions of T_R and τ_P are substituted into Eqn. 2.1.14, the threshold gain will be equal to

$$G_{th} = \alpha_L L_C + \frac{1}{2}\ln\frac{1}{R_1 R_2}. \tag{2.1.15}$$

In summary, once the small signal population inversion is equal to the cavity and material losses, laser threshold is reached. Once it is reached, laser oscillation is readily observed.

In ref [48], threshold power required to attain laser oscillation for Gaussian beams was further derived as follows:

$$P_{th} = \frac{\pi h \nu_P (\omega_L^2 + \omega_P^2)(T + L)}{4 \eta_a \tau_2 \sigma_e}. \tag{2.1.16}$$

In the above equation, ω_L and ω_P are the laser and pump beam waists, respectively, η_a is the fractional absorbed pump power by the gain medium, T is the total transmission of mirrors, τ_2 is the spontaneous lifetime, and L is the total passive cavity loss for one round trip. One can use this equation to estimate the required minimum pumping power to achieve laser operation.

2.1.3 Continuous-wave operation

It was shown in earlier section that gain (G) and laser power (P_L) satisfy the coupled differential equations in 2.1.8 and 2.1.9. By using steady state solutions of these equations, one can develop an idea on the continuous wave operation of lasers as well. After finding the relation between output power and small signal gain, analysis of an efficiency curve, and what information can be extracted from this curve will be discussed.

i) When we set $\frac{dG}{dt} = 0$ in Equation 2.1.8, the steady state gain is given by

$$G_s = \frac{G_0}{1 + \frac{P_L}{P_{Sat}}}. \tag{2.1.17}$$

In steady state, saturated gain will be equal to the threshold gain $G_s = G_{th}$. In a standing-wave laser cavity, because of forward and backward travelling waves, total intracavity power is twice the value of P_L in Eqn 2.1.17. When we rearrange it, we obtain the relation between the cw output power and small signal gain as:

$$P_{out} = T\frac{P_{Sat}}{2}\left(\frac{G_0}{G_{th}} - 1\right), \qquad 2.1.18$$

where T is the transmission of the output coupler from which the laser power is delivered out of the cavity. By looking at this equation one can easily see that the output power linearly scales with the small signal gain (G_0) defined in Eqn 2.1.12.

In earlier section, by setting $\frac{dP_L}{dt} = 0$, the threshold gain was obtained as

$$G_{th} = \alpha_L d_g + \frac{1}{2}\ln\left(\frac{1}{R_1 R_2}\right). \qquad 2.1.19$$

For a typical laser cavity, the above equation can be approximated as $G_{th} \approx 1/2(L + T)$, where L accounts for the material losses and T is the transmission of the output coupler. Now, in order to find the explicit relation between output power and pump power, substitute G_{th}, small signal gain (G_0) and saturation power (P_{Sat}) into output power equation derived in 2.1.23. After simplification, the ratio of output power to input power has the form

$$\eta = \frac{\Delta P_{out}}{\Delta P_P} = \frac{T}{T + L}\frac{\lambda_P}{\lambda_L}\eta_a, \qquad 2.1.20$$

where η is called the slope efficiency and $\eta_a = \sigma_a N_g d_g$. This result is a very useful tool in determining the material losses (L) of the laser by simply measuring two slope efficiencies with two different T values. Figure 2.1.4 shows a typical efficiency curve and the best fit line.

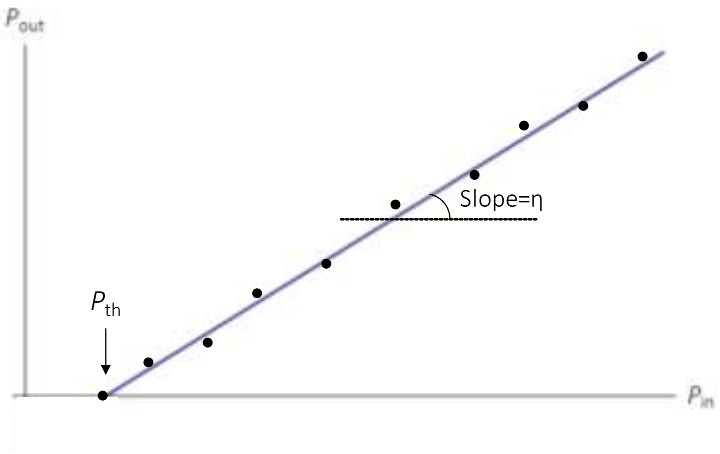

Figure 2.1.4: Input vs output power curve with best fit line.

2.2 Pulsed-laser operation

As the name suggests a pulsed laser produces pulses with a certain repetition rate and pulse duration. Pulsed operation can be categorized under two categories: Q-switched operation and mode-locked operation. Q-switched operation refers to the pulse formation by modulating the gain, which can be achieved with either active switches put inside the cavity (electro-optic modulators) or passive saturable absorbers. For typical Q-switched lasers, the resulting pulse energies are typically in the range of micro to milli joules.

In the case of mode-locked operation, randomly oscillating longitudinal modes inside the laser cavity should have a constant phase relation, in other words longitudinal cavity modes supported by the gain bandwidth should be locked. Similar to q-switching, both active and passive mode-locking methods exist [49, 50]. In comparison with q-switched lasers, modelocked lasers produce lower pulse energies but higher peak powers due to having shorter pulse durations (typically 10^{-15} s).

As we mentioned earlier, in a modelocked laser, the longitudinal modes inside the cavity oscillate with a constant phase relation. The electric field of arbitrary oscillations can be written as a summation in the form of

$$E(t) = \sum_{n=-m}^{m} E_n \exp i \left[\left(\omega_0 + n\frac{2\pi}{T_R}\right) t + \varphi_n\right], \tag{2.2.1}$$

where E_n and φ_n are the electric field amplitude and phase of the *n*th mode, ω_0 is the center frequency of the gain band, T_R is the roundtrip time which equals $2L_R/c$. When we do the summation over all modes supported by the gain medium, we end up with the following intensity profile:

$$I(t) \propto E(t)E^*(t) = E_0^2 \frac{\sin^2\left(\frac{N\pi t}{T_R}\right)}{\sin^2\left(\frac{\pi t}{T_R}\right)}. \tag{2.2.2}$$

Here N is the number of modes that oscillate with constant phase. Figure 2.2.1 shows the calculated intensity profiles by using the Eqn. 2.2.2 with different number of phase locked modes (N). By looking at the figure, we can easily notice three features: 1) As we increase the number of oscillating modes, the duration of the resulting pulses become shorter. 2) Changing N, does not affect the repetition rate of the output. 3) P_{Peak}/P_{av} increases by N.

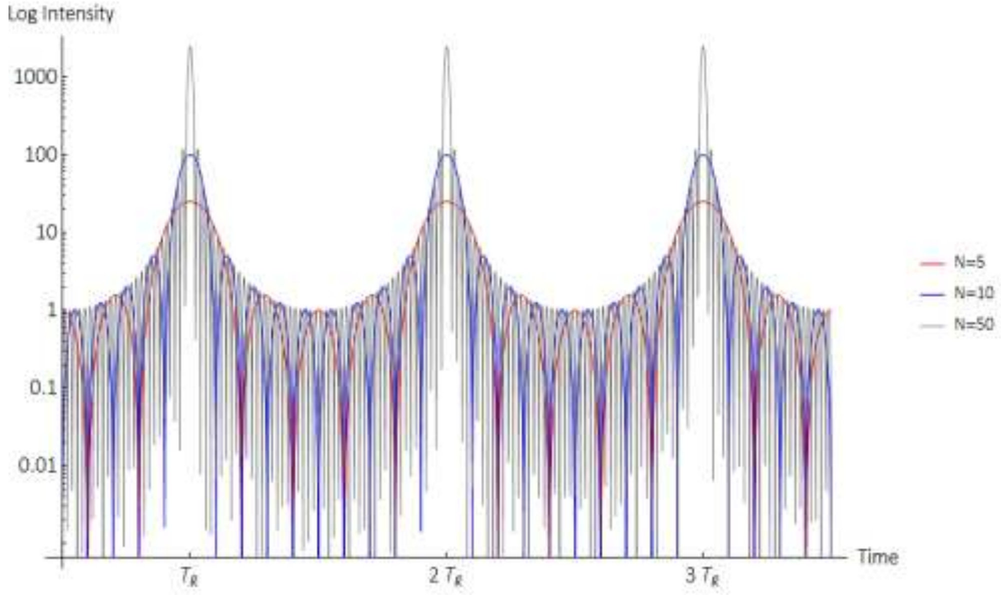

Figure 2.2.1:Logarithmic intensity vs time plot where N=5,10 and 50 in Eqn. 2.2.2.

In section 2.2.1 saturable absorber modelocking will be described in detail. In section 2.2.2 another passive modelocking technique called Kerr lens modelocking will be discussed.

2.2.1 Saturable absorber mode locking

Saturable absorption refers to the fact that the transmission of an absorbing material increases with increasing light intensity. Saturable absorption of different materials, namely quantum well structures, graphene, carbon nanotubes, is widely used in mode locking lasers [51, 52]. These materials can be classified under two classes, depending on their recovery time, as fast or slow saturable absorber (SA). In modeling a slow saturable absorber, one has to take into account the change in the gain after one pass. However in the fast saturable absorber case, recovery of the material is so fast that the gain is assumed to be constant, which is the subject of this thesis work.

The master equation developed by Herman Haus [53], provides a powerful tool in modeling the output of mode-locked lasers. The master equation for a fast saturable absorber is the following

$$\frac{1}{T_R}\frac{\partial}{\partial T}a = (g-l)a + \frac{g}{\Omega_\mathrm{g}^2}\frac{\partial^2}{\partial t^2}a + \gamma|a|^2 a. \qquad 2.2.3$$

Here $|a|^2$ corresponds to the instantaneous power. T_R is the cavity roundtrip time, g and l are the gain and loss, respectively, Ω_g is the gain bandwidth, and γ is the self amplitude modulation (SAM) coefficient. Finally, t represents small time scale of the order of pulsewidth, and T represents large time scales comparable to cavity roundtrip times.

Steady state $(d/dT = 0)$ solution of the differential equation in Eqn. 2.2.3 is [53, 54]

$$a(t) = A_0 \operatorname{sech}\left(\frac{t}{\tau}\right), \qquad 2.2.4$$

which gives the pulse shape of generated pulses from a passively mode locked laser where A_0 is the amplitude and τ is the pulsewidth.

2.2.2 Kerr lens mode locking (KLM)

Kerr-lens mode locking is a passive mode locking technique in which the constant phase relation between longitudinal modes is achieved with a $\chi^{(3)}$nonlinear process known as the Kerr effect. Depending on the value and sign of the nonlinear refractive index (n_2), the refractive index becomes a function of intensity and can be expressed in the form

$$n(I) = n_0 + n_2 I. \qquad 2.2.5$$

Here, n_0 is the linear refractive index of the material and $n(I)$ is the modified refractive index at high intensities. Since laser beams have a Gaussian intensity profile, i.e. center of the beam is more intense compared to the edges, at high intensities a virtual lens is formed inside the material. This phenomenon is called self-focusing. Figure 2.2.2 illustrates how Kerr effect is used to attain constant phase relation which leads to the generation of ultrashort pulses.

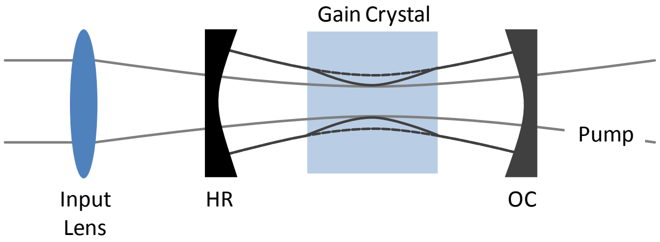

Figure 2.2.2: Schematic of a basic resonator to describe how Kerr lensing is employed to produce ultrashort pulses.

Figure 2.2.2 shows a simplified laser setup which contains an input lens, 2-mirror resonator, the gain crystal together with the beam profiles of both pump and laser beams. In this configuration, an intense spike passing through the gain crystal undergoes self-focusing due to Kerr effect and overlaps better with the pump beam. Hence, the laser sustains mode-locked operation as opposed to continuous wave (cw) operation by taking the advantage of Kerr effect.

Kerr-lens mode locking can be regarded as a fast saturable absorber mode locking and modeled by using the following equation:

$$\frac{1}{T_R}\frac{\partial}{\partial T}a = (g-l)a + \left(\frac{1}{\Omega_f^2} + jD\right)\frac{\partial^2}{\partial t^2}a + (\gamma - j\delta)|a|^2 a. \qquad 2.2.6$$

Eqn. 2.2.7 has a solution in the form of

$$a(t) = A_0 \operatorname{sech}^{1+j\beta}\left(\frac{t}{\tau}\right). \qquad 2.2.7$$

However in the presence of self phase modulation (SPM) due to the Kerr effect, generated pulses will be distorted in the frequency domain. In order to balance SPM, negative dispersion should be introduced into the cavity. Figure 2.2.3 (a) shows the phase shift curves coming from both self phase modulation and dispersion compensation. Figure 2.2.3 (b) shows the combination of both.

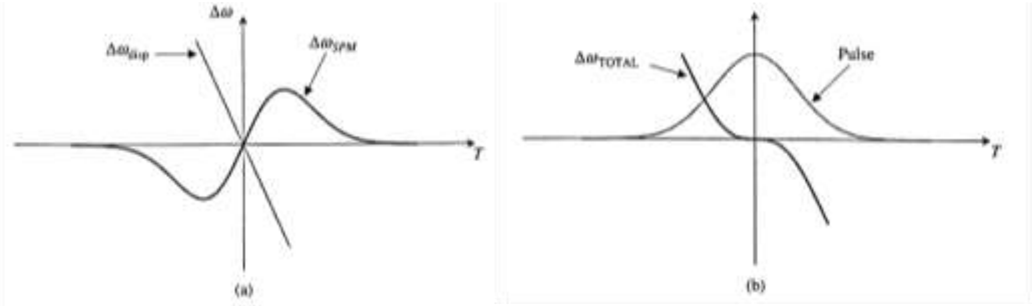

Figure 2.2.3: (a) Phase shift resulting from self phase modulation and dispersion inside the cavity.(b) total phase shift acquired by the pulse [47].

As it can be seen from the figure, combination of negative dispersion and SPM gives zero dispersion at the center of the pulse. In this case, generated pulses are called solitons. A simplified version of the master equation introduced in Eqn. 2.2.6 can be written by assuming 1) weak filtering due to having broad gain bandwidth and 2) small SAM coefficient ($\gamma \approx 0$):

$$\frac{1}{T_R}\frac{\partial}{\partial T}a = jD\frac{\partial^2}{\partial t^2}a - j\delta|a|^2 a. \qquad 2.2.8$$

Eqn. 2.2.8 also has a hyperbolic secant solution of the form

$$a(T,t) = A_0 \operatorname{sech}\left(\frac{t}{\tau}\right) e^{-j\frac{\delta|A_0|^2 T}{2T_R}}. \qquad 2.2.9$$

In addition, from the solution of the master equation (Eqn. 2.2.8), it can be shown that solitons satisfy the area theorem

$$|A_0|\tau = \sqrt{\frac{2|D|}{\delta}} \qquad 2.2.10$$

By squaring both sides and by using $W = 2|A_0|^2\tau$, one obtains the relation between pulse energy (*W*), pulse duration divided by a factor of 1.76 (τ) and the group delay dispersion (*D*) as

$$\tau = \frac{4|D|}{W\delta}. \qquad 2.2.11$$

2.2.3 Dispersion compensation

By definition, dispersion is the wavelength dependent refractive index of materials. The well known example of this phenomenon is the formation of rainbows. When white light, i.e. combination of different colors, passes through a dispersive medium, because of dispersion each color refracts with a different angle (See Figure 2.2.4).

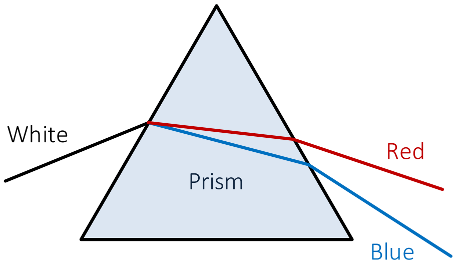

Figure 2.2.4: Schematic of a prism showing dispersion due to refraction.

In literature, empirical formulas are produced to provide the wavelength dependent refractive index of materials. Such equations are called Sellmeier equations which usually have the form

$$n^2(\lambda) = 1 + \sum_i \frac{B_i\lambda^2}{\lambda^2 - C_i}. \tag{2.2.12}$$

As we mentioned in earlier section, femtosecond pulse generation cannot be achieved unless negative group delay dispersion (GDD) is introduced into the cavity to balance the nonlinear phase shift. In literature, many materials and structures are used for dispersion compensation, such as slabs, prism pairs, GTIs and DCMs. Group delay dispersion (GDD) for a slab of material is defined as the second derivative of the phase with respect to frequency as [55]

$$\frac{d^2\varphi}{d\omega^2} = \frac{\lambda^3 L_s}{2\pi c^2}\frac{d^2 n}{d\lambda^2}, \tag{2.2.13}$$

where φ is the phase, ω is the angular frequency, L_s is the length of the slab, c is the speed of light and n is the refractive index. The second derivative of Sellmeier equation determines the sign of GDD. It can be either positive or negative for a material, at different wavelength ranges.

Another way of producing negative GDD is the well known prism pair configuration. Figure 2.2.5 illustrates a schematic of a pair of prisms which leads to negative dispersion.

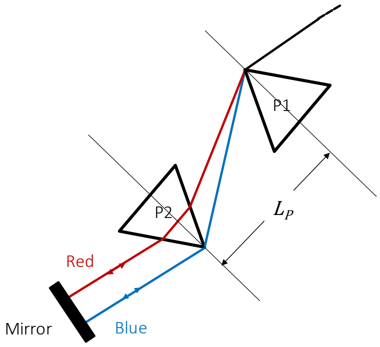

Figure 2.2.5: Schematic of a typical prism pair configuration.

GDD generated from a prism pair [55] is given by

$$\frac{d^2\varphi}{d\omega^2} = \frac{\lambda^3}{2\pi c^2}\frac{d^2 Z}{d\lambda^2}, \qquad 2.2.14$$

where Z is the optical path length and the second derivative of optical path length with respect to wavelength can be derived as [55]:

$$\frac{d^2 Z}{d\lambda^2} = 4\left[\frac{d^2 n}{d\lambda^2} + (2n - n^{-3})\left(\frac{dn}{d\lambda}\right)^2\right] L_P \sin\beta - 8\left(\frac{dn}{d\lambda}\right)^2 L_P \cos\beta. \qquad 2.2.15$$

where L_P is the separation between the tips of the prisms, as shown in Figure 2.2.5 and β is the angular spread of the beam due to dispersion.

2.3 Transient absorption spectroscopy

With the development of robust pulsed laser systems, time resolved spectroscopy techniques have been developed as well. In the case of transient absorption spectroscopy, the absorbance of a material is monitored with respect to the time delay between pump and probe pulses. In Section 2.3.1, details of a transient absorption spectrometer are outlined. In the Sections 2.3.2 and 2.3.3, lifetime and saturation fitting procedures are described.

2.3.1 Measurement

Transient absorption spectroscopy is a widely used characterization method that measures the nonlinear absorption of materials. In this technique, the differential absorption (ΔA) is recorded as a function of the delay between probe and pump excitation. Figure 2.3.1 shows a simplified schematic of a typical transient absorption spectrometer. Here, the pump beam excites the system to an excited state and the spectrometer records the change in absorption at broadband or single wavelength with the help of the probe pulse as a function of the delay provided by the translation stage.

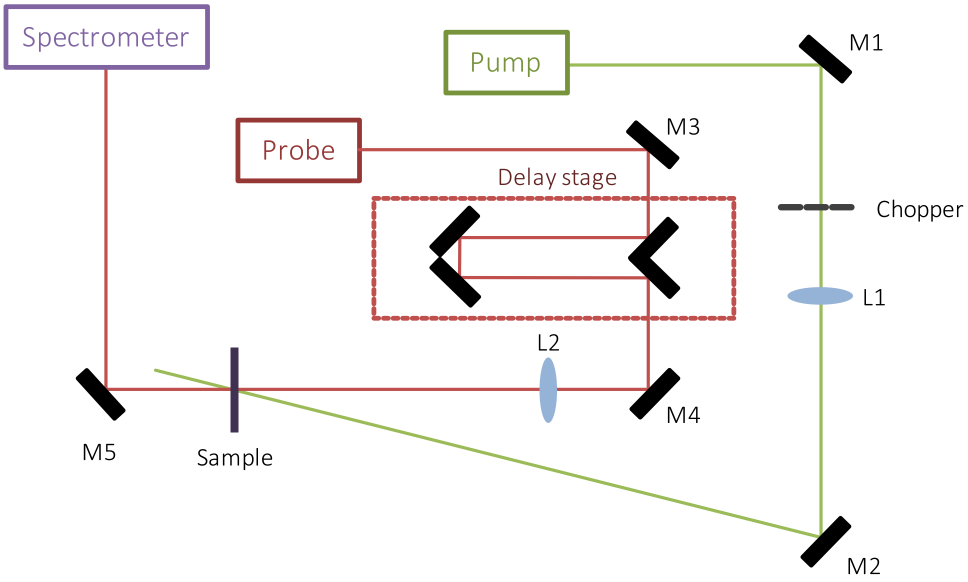

Figure 2.3.1: Simplified schematic illustration of a transient absorption spectrometer.

Differential absorption is defined as

$$\Delta A = A_{pumped} - A_{unpumped}. \quad 2.3.1$$

As a result, positive ΔA indicates that pumped absorbance is greater than unpumped case so that excited state absorption occurs. Negative ΔA means that the pumped absorbance is smaller than unpumped case hence resulting in bleaching.

2.3.2 Lifetime fitting

Figure 2.3.2 shows a typical lifetime decay data of a monolayer graphene measured with a transient absorption spectrometer. In order to extract the time constant from the given curve, the number of exponentials has to be chosen. In the case of graphene, it is known from previous studies that it has bi-exponential decay [56]. Hence the following equation is fitted to the curve:

$$\Delta A(t) = A_1 \exp\left[-\frac{t-t_0}{\tau_1}\right] + A_2 \exp\left[-\frac{t-t_0}{\tau_2}\right], \quad 2.3.2$$

where $A_1$and A_2 are the weighted amplitudes of two exponential decays, $\tau_1$and τ_2 are the time constants of the decays.

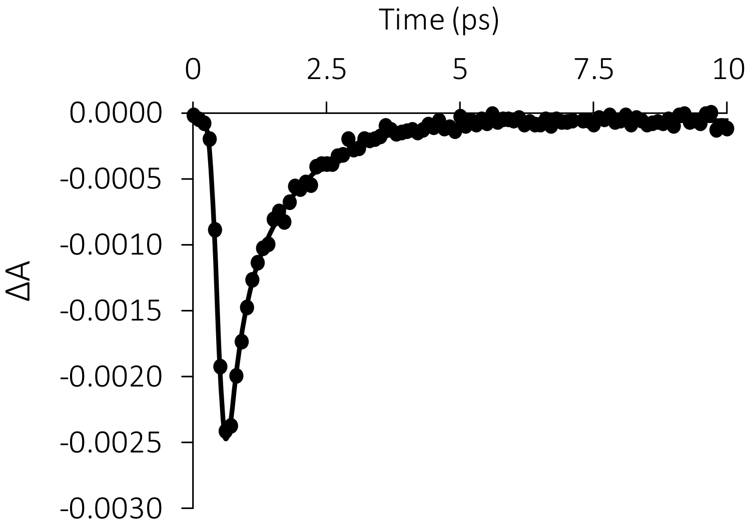

Figure 2.3.2: Transient curve of a monolayer graphene.

Based on the fitting results, fast and slow time constants were determined as 200fs and 1.1ps, respectively.

2.3.3 Saturation fitting

Before using a material as a saturable absorber, four parameters have to be measured: saturation fluence (J_{sat}), modulation depth (ΔT), non saturable losses (T_{ns}) and recovery time (τ_A) at a specific wavelength. By looking at these parameters, one can judge whether or not the material of interest is a suitable saturable absorber for a specific laser system. Figure 2.3.3 shows a typical saturation curve, where modulation depth and non-saturable loss are 1% and 0.2%, respectively. Here, the saturation parameter defined as $S = J/J_{sat}$. Therefore $S = 1$ corresponds to the intensity being equal to the saturation fluence (J_{sat}).

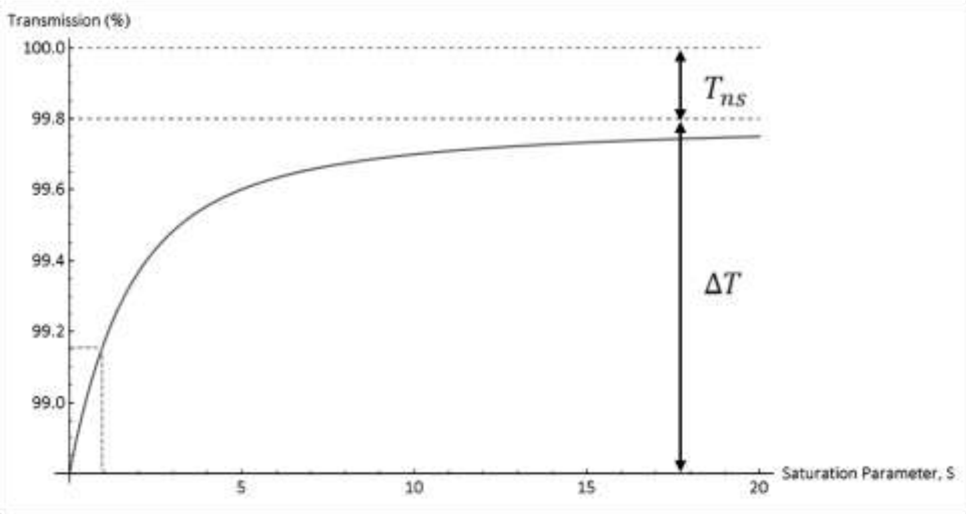

Figure 2.3.3: A typical saturation curve, showing the transmission as a fuction of the saturation parameter.

By comparing the pulse duration (τ_P) of the excitation source and the recovery time (τ_A) of the absorber, two types of fit equations are used (See Table 2.3.1).

Table 2.3.1: Different fitting equations based on the type of the saturable absorber and the excitation source.

Type	Reference	Equation	
Fast SA $\tau_P \ll \tau_A$	[57]	$q(J) = \dfrac{q_S}{\dfrac{J}{J_{Sat}}\sqrt{1+\dfrac{J_{Sat}}{J}}} \tanh^{-1}\left[\sqrt{\dfrac{1}{1+\dfrac{J_{Sat}}{J}}}\right] + q_{ns}$	2.3.3
Slow SA $\tau_P \gg \tau_A$	[58, 59]	$q(J) = q_S \dfrac{J_{Sat}}{J}\left(1 - \exp\left[-\dfrac{J}{J_{Sat}}\right]\right) + q_{ns}$	2.3.4

Here $q(J)$ is the sum of the saturable (q_S) and non-saturable losses (q_{ns}) coming from the saturable absorber. For the fast saturable absorber case ($\tau_P \ll \tau_A$), the recovery time is longer compared to the excitation source and hence, the temporal pulse profile of the excitation should be taken into account. In Refs [57, 58], hyperbolic secant shaped pulse profile is used in the derivation of Eqn. 2.3.2, tabulated in Table 2.3.1. In contrast, for a slow saturable absorber, excitation pulse duration is sufficiently short, compared to the recovery time of the SA. Hence, the pulse shape becomes irrelevant. During our experiments, pulse duration of the laser was around 100 fs, and recovery time of graphene was around 1.5 ps. Therefore, graphene was treated as a slow saturable absorber.

When measuring the saturation curves, we used a transient absorption spectrometer and recorded the differential absorbance as a function of the incident fluence. Hence, by using the loss equation defined for the slow SA case, we derived a new fit equation in terms of differential absorbance (ΔA). Differential absorbance was defined as

$$\Delta A = A(J = J_P) - A(J = 0), \tag{2.3.5}$$

in Section 2.3.1. When we convert the pumped and un-pumped absorbance to transmission we get the following expression:

$$\Delta A = -\frac{1}{T_0 \ln 10}\left(T(J = J_P) - T(J = 0)\right), \tag{2.3.6}$$

where T_0 is the steady state transmission, $T(J = J_P)$ is the pumped transmission, $T(J = 0)$ corresponds to the un-pumped transmission of the sample under investigation. By using the total loss coming from the absorber (Eqn. 2.3.4), pumped and un-pumped total transmission expressions are

$$T(J = J_P) = 100 - q(J_P) = 100 - q_S \frac{J_{Sat}}{J_P}\left(1 - \exp\left[-\frac{J_P}{J_{Sat}}\right]\right) - q_{ns} \tag{2.3.7}$$

$$T(J = 0) = 100 - q(0) = 100 - q_S - q_{ns} \tag{2.3.8}$$

For the J=0 case, we used the following approximation for the exponential term:

$$\exp\left[-\frac{J}{J_{Sat}}\right] \approx 1 - \frac{J}{J_{Sat}} \qquad 2.3.9$$

By substituting Equations 2.3.7 and 2.3.8 into Equation 2.3.6, we obtain

$$\Delta A = -\frac{1}{T_0 \ln 10}\left(\left(100 - q_S \frac{J_{Sat}}{J}\left(1 - \exp\left[-\frac{J}{J_{Sat}}\right]\right) - q_{ns}\right) - (100 - q_S - q_{ns})\right) \qquad 2.3.10$$

After simplification, the final form of the fit equation becomes

$$\Delta A = -\frac{q_s}{T_0 \ln 10}\left(-\frac{J_{Sat}}{J}\left(1 - \exp\left[-\frac{J}{J_{Sat}}\right]\right) + 1\right) \qquad 2.3.11$$

Figure 2.3.4 shows a typical saturation curve for a mono layer graphene transferred onto a quartz substrate.

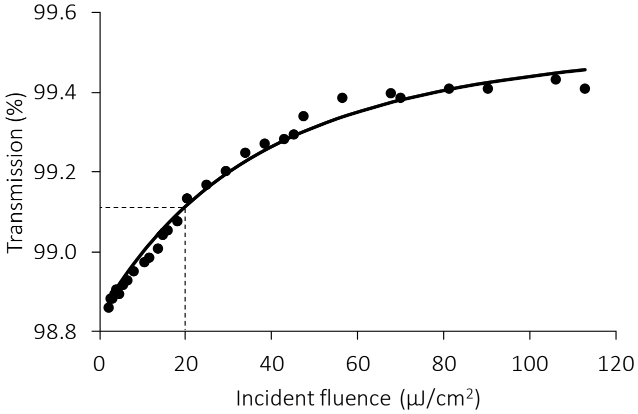

Figure 2.3.4: Saturation curve of monolayer graphene on quartz.

Saturation fluence (J_{sat}) and modulation depth (ΔT) values determined from the fit (Eqn. 2.3.11) are 20 μJ/cm^2 and 0.75%, respectively.

Chapter 3: Development of Femtosecond Cr:ZnSe Laser

3.1 Introduction

Since its first demonstration in 1996 [60], Cr:ZnSe has emerged as a versatile solid-state source of tunable coherent radiation in the mid infrared (mid-IR), covering the wavelength range 1880-3349 nm [34, 61]. Since the room-temperature luminescence quantum efficiency at low doping levels is close to unity [62], efficient continuous-wave (cw) operation [63-71] can be readily obtained. Furthermore, the vibronically broadened emission band can be utilized to produce mode-locked pulses with picosecond [35] or femtosecond duration [36-39, 72-74]. In previous studies, two main methods have been employed to generate femtosecond pulses from Cr:ZnSe lasers: saturable absorber mode locking [36, 39, 72, 73], and Kerr-lens mode locking (KLM) [37, 38, 74]. Development of stable, mid-infrared femtosecond sources is needed in numerous emerging applications which are mentioned in Chapter 1.

In the case of saturable absorber modelocking, the more conventionally used semiconductor saturable absorber mirrors (SESAMs) were utilized to produce femtosecond pulses [52]. SESAMs have the drawback of operating only over a limited wavelength range set by the resonant behavior of the semiconductor quantum well structure and the bandwidth of the high-reflector coating. To overcome the operation bandwidth and tuning range limitations, single-walled carbon nanotube saturable absorbers (SWCNT-SAs) and graphene saturable absorbers (GSAs) have been used [75, 76]. With SWCNT-SAs, mode-locked operation in the wavelength range of 800-2070 nm has been demonstrated [77, 78]. Use of SWCNT-SAs at longer wavelengths is limited due to the infrared absorption of the PMMA host. Furthermore, practical limits in the diameter of currently producible single-walled carbon nanotubes have kept the corresponding transition wavelengths of the SWCNT-SAs near or below 2 μm [78].

In comparison with SESAMs and SWCNT-SAs, GSAs offer the great potential of overcoming the spectral limitations discussed above. This is because even a single atomic layer of graphene, possessing a point-bandgap structure, has been shown to provide sufficient saturable absorption over an ultra-wide range of wavelengths. Furthermore, no additional polymer matrix is required to hold the saturable absorber on the substrate. In this case, the absorption band resulting from graphene extends from the visible to the infrared with a constant value of $\pi\alpha$, where α is the fine structure constant given by 1/137. To date, many fiber [79] and solid-state lasers [80-82] have been mode-locked by utilizing graphene as a saturable absorber in a broad wavelength range. Among them, the longest achieved mode-locked operation wavelength was near 2 μm [82].

Irrespective of the mode locking method used, careful dispersion management of the resonator is very crucial in order to balance the nonlinearities stemming from the Kerr medium and/or the saturable absorber. To manage the group delay dispersion (GDD), various types of optical elements, including prism pairs [37, 39, 74], dispersion compensating mirrors (DCM) [73], Gires–Tournois interferometer (GTI) mirrors, and slabs [36, 38, 72, 74] can be used. The ideal choice of the dispersion compensator depends on several factors including the amount of negative GDD that can be produced, the level of residual third-order dispersion, and the insertion loss of the compensator. Commercial DCMs and GTI mirrors are available for femtosecond lasers in the visible and near infrared. However, at present, such dispersion compensators are not readily available commercially at mid-IR wavelengths. If slabs or prism pairs are used as an alternative, the emission band of the laser should coincide with the transparency window of the materials that will be used as slabs or prisms. These considerations show that, it is important to develop cost effective dispersion management methods for lasers that operate in the mid-IR range. Hence it is important to evaluate the viability of various low-cost dispersion compensation methods.

In the following Sections 3.2 experimental details and results of graphene mode locked Cr:ZnSe laser will be discussed. In addition, evaluation of different dispersion compensation methods applied to a Kerr-lens mode locked Cr:ZnSe laser will be presented in Section 3.3.

3.2 Graphene mode-locked operation

3.2.1 Experimental

The saturable absorber based on high-quality monolayer graphene is usually fabricated on quartz substrates, which is a limiting factor in extending the operation wavelength of graphene mode locked lasers beyond 2 μm [51, 83]. This can be remedied by using an infrared-transparent substrate: calcium fluoride (CaF_2). The saturable absorber based on high-quality monolayer graphene used in our experiments was fabricated by employing a similar method described in ref [81]. The monolayer graphene was synthesized on a Cu film by chemical vapor deposition (CVD) technique. After rapid cooling, poly-methyl methacrylate (PMMA) was deposited on the grown graphene as a supporting material. The graphene/PMMA layer was then separated from the Cu film by wet etching and transferred onto a CaF_2 substrate of 1 inch diameter. Subsequently, the PMMA layer was completely removed by using acetone.

A schematic of the laser setup used in the mode-locking experiments is shown in Figure 3.2.1. A 2.4-mm long Cr:ZnSe crystal was positioned between two highly reflecting concave mirrors (radius of curvature=100mm) at Brewster’s angle and was water-cooled at

21°C. The crystal was pumped with a 5-W Tm:fiber laser (IPG Photonics, TLR-5-1800-LP) operating at 1.8 μm.

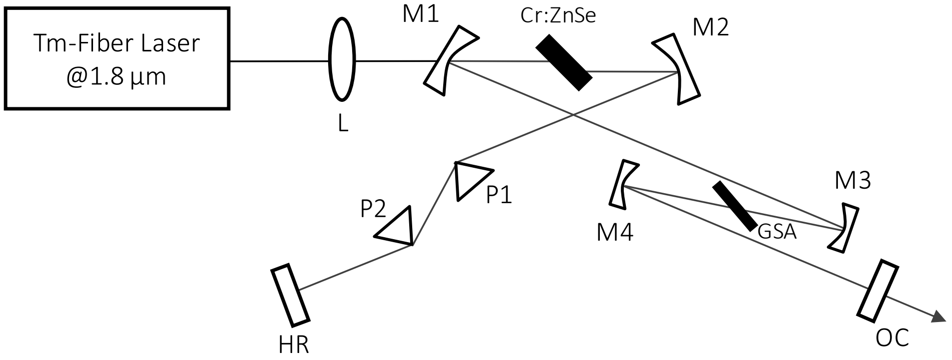

Figure 3.2.1: Experimental setup of the GSA mode-locked Cr:ZnSe laser. M1, M2, M3, and M4 are highly reflecting concave mirrors (ROC=100mm), OC is 3% and 6% output coupler. L is the pump focusing lens (f=7.5cm). P1 and P2 are the CaF_2 dispersion compensation prisms.

The high reflector (HR) and output coupler (OC) arm lengths were 62 cm and 120 cm, respectively, resulting in a total cavity length of around 2 meters. Two Brewster cut CaF_2 prisms (P1 and P2) were placed at minimum deviation in the HR arm for dispersion compensation. The GSA was put at Brewster's incidence between two curved mirrors (M3 and M4, each with ROC=100mm).

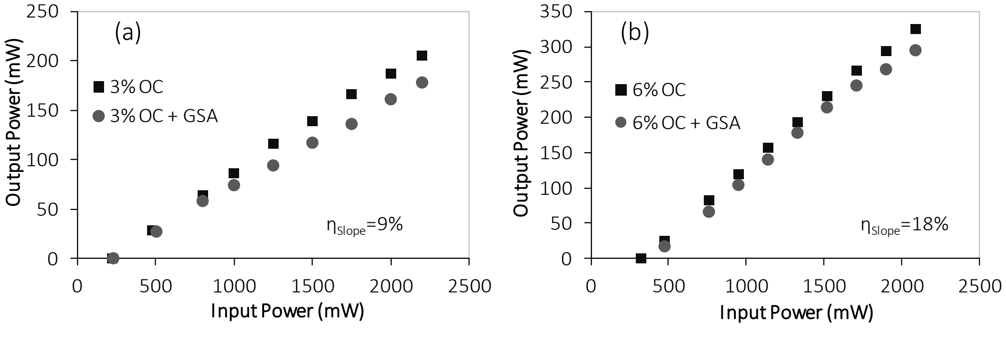

Figure 3.2.2: Continuous-wave efficiency curves of the Cr:ZnSe laser operating with (a) 3% and (b) 6% output couplers (OC).

Figure 3.2.2 shows the efficiency curves taken with the Cr:ZnSe laser with 3% and 6% transmitting output coupler. In the continuous wave (cw) regime, the laser with the 6% OC delivered as high as 300 mW of output power at the input pump power of 2 W. By comparing the slope of the efficiency curves with that of the empty cavity, the insertion loss of the GSA and focusing optics (M3 and M4) was estimated to be 4.2%. Because the single-pass transmission of GSA at 2500nm was measured as ~2.1% (see Figure 3.2.3), the estimated roundtrip passive loss of 4.2% agrees well with the optical transmission data displayed in Figure 3.2.3.

During the mode-locking experiments, we utilized a pair of CaF_2 prisms for dispersion compensation. Taking into account the dispersion of the Cr:ZnSe crystal, prism pair (separation=22cm), substrate of GSA (2mm-CaF_2), and insertion of prisms (13mm-CaF_2), the overall group delay dispersion of the cavity was estimated to be -2609 fs^2. To initiate mode-locking, GSA was translated through the beam waist produced by M3 and M4. Stable mode-locked operation was readily observed and could be sustained for several hours. The minimum output power to initiate mode-locked operation was measured to be 50mW, when the laser was pumped at 1.1W (from Figure 3.2.2). Stable, single-pulse mode-locking was obtained up to 80 mW, beyond which cw peaks appeared in the spectrum. The spectrum was measured with a scanning spectrometer. In the autocorrelation measurements, two-photon absorption in a germanium photo detector was employed.

3.2.2 Results and Discussion

To test the quality of the fabricated sample we measured the optical transmission spectrum and Raman spectrum. As can be seen from the optical transmission curve displayed in Figure 3.2.3, the monolayer graphene shows the zero bandgap behavior with a nearly constant absorption of $\leq 2.3\%$ above 900 nm up to the mid-infrared spectral region. The amount of absorption is in very good agreement with the theoretically expected value of $\pi\alpha$ for graphene.

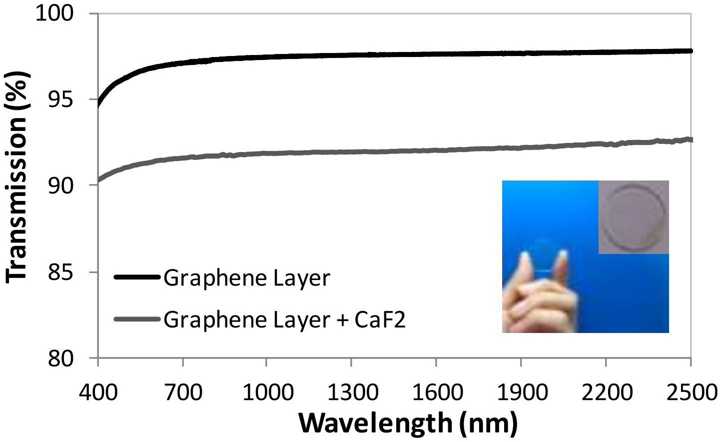

Figure 3.2.3: Optical transmission of the high-quality monolayer graphene transferred onto CaF_2.

Information regarding the quality and number of graphene layers can be inferred from Raman spectrum measurements [84]. Figure 3.2.4 shows the Raman spectrum of our sample measured with a Renishaw Invia Raman microscope at the pump wavelength of 532 nm.

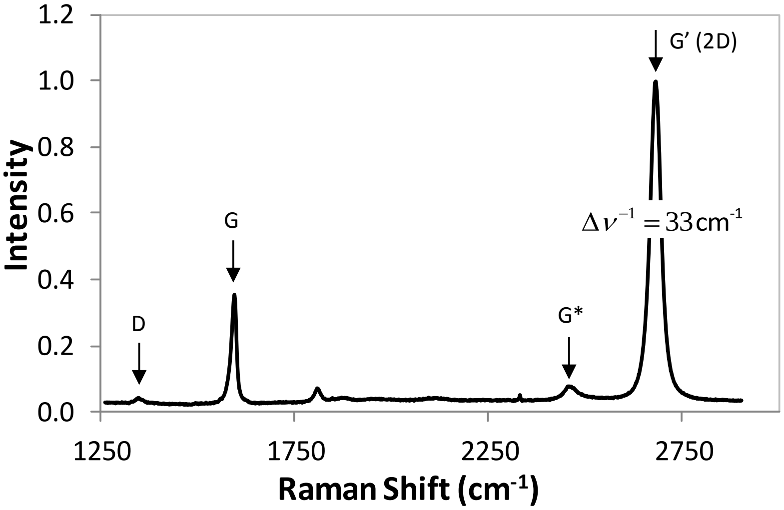

Figure 3.2.4: Measured Raman spectrum of the monolayer graphene on CaF_2.

The well-known D, G, G* and G’ (2D) bands were clearly observed as expected. From the measured spectrum, the estimated value of the $I_G/I_{G'}$ ratio and the linewidth of the G’ band came to 0.36 and 33 cm^{-1}, suggesting that the transferred graphene was nearly a monoatomic layer. Similar values were reported for monolayer graphene on other substrates in previous studies [85]. In addition, the I_D/I_G ratio is well below 0.3, indicating that the layer is nearly defect free.

The estimated spot size on the sample came to 47 μm, which gives a threshold intracavity fluence of 312 $\mu J/cm^2$ for mode-locking at the output power of 50 mW. At the highest mode-locked average output power of 80 mW, the corresponding intracavity fluence on the GSA was determined to be 500 $\mu J/cm^2$. Up to this fluence level, no damage occurred on the surface of the GSA sample. Based on our measurements at other wavelengths above 1000 nm where the linear absorption is nearly constant, we expect a modulation depth of $< 0.4\%$ and a saturation fluence of < 14 $\mu J/cm^2$ for the monolayer GSA near 2500nm [80].

Figure 3.2.5 and Figure 3.2.6 show the spectrum, autocorrelation trace and RF spectrum of the generated pulses shown for the 3% and 6% output couplers, respectively. The spectrum was measured with a home-made scanning spectrometer. The spectral bandwidth (43nm) and center wavelength (2400nm) for both cases showed similar results. In the autocorrelation measurements, the two photon absorption signal was measured in a Ge detector. By assuming a $sech^2$-shaped pulse profile, the pulsewidth was determined to be 176 fs and 202 fs with the 3% and 6% OC, respectively. Moreover, RF spectra of the fundamental tone, measured with a resolution bandwidth of 1 kHz, show that the side band noise level was 65 (55) dB below the carrier for the 3% (6%) output coupler.

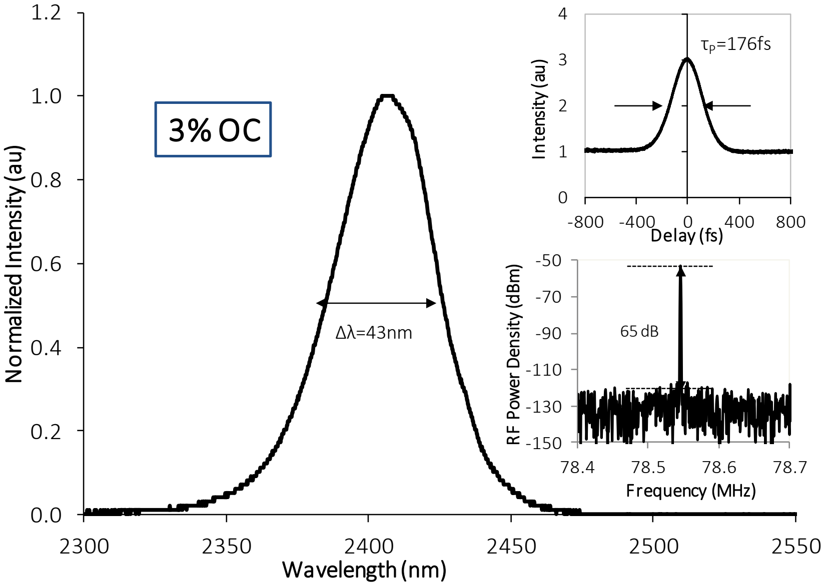

Figure 3.2.5: The optical spectrum, autocorrelation, and RF spectrum of the femtosecond pulses generated with 3% output coupler.

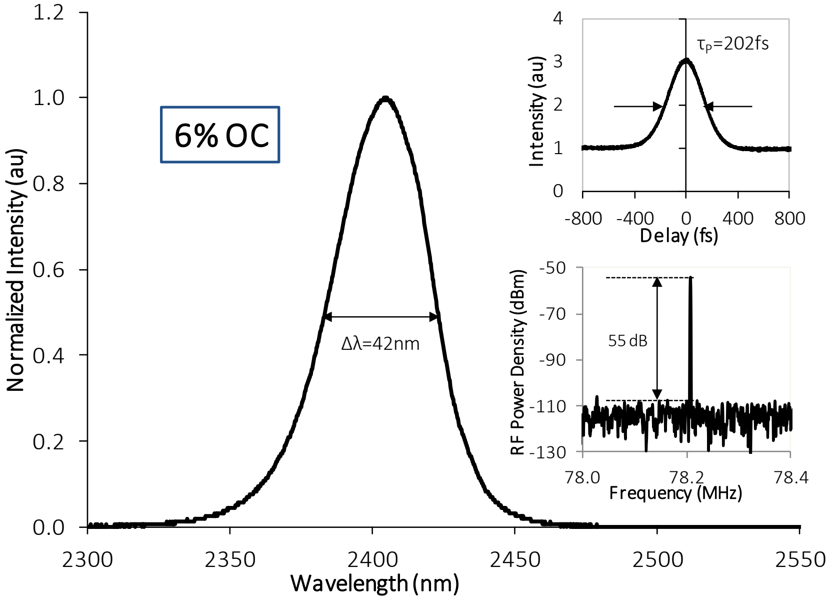

Figure 3.2.6: The optical spectrum, autocorrelation, and RF spectrum of the femtosecond pulses generated with 6% output coupler.

In conclusion, we demonstrated the operation of a stable 2.5-μm femtosecond Cr:ZnSe laser, passively mode-locked with high-quality, monolayer graphene coated on a CaF_2 substrate. The laser produced 176-fs pulses at a repetition rate of 78 MHz with an average power of 80 mW. The measured time-bandwidth product was 0.39 with 3% OC. With a 6% OC, 2.4-nJ, 200-fs pulses were generated near 2400 nm at a pulse repetition frequency of 78 MHz. The average mode-locked output power was 185 mW. To the best of our knowledge, this represents the first demonstration of a femtosecond Cr:ZnSe laser passively mode locked with a graphene saturable absorber.

3.3 Kerr-lens mode-locked operation

3.3.1 Experiment

In this work, prism pairs made of CaF_2 and MgF_2, and slabs of BK7 and YAG were investigated for dispersion compensation. The schematic of the experimental setup is shown in Figure 3.3.1. The Cr:ZnSe laser was configured as a standard, astigmatically compensated x-resonator with two curved high reflectors (M1 and M2, R=10 cm) around the 2.4-mm-long, single-crystal Cr:ZnSe gain medium, a flat end high reflector (HR) and a flat output coupler (OC). Two different output couplers with 1% and 6% transmission at 2400 nm were used in the experiments. The high reflector and the output coupler arm lengths were 65 cm and 84 cm, respectively, giving an estimated beam waist of 35 μm near the center of the cavity stability range.

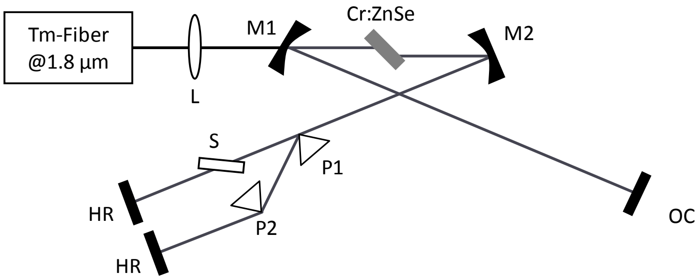

Figure 3.3.1: Experimental setup of the Kerr-lens mode-locked Cr:ZnSe laser containing a slab (S) or a prism pair (P1 and P2) for dispersion compensation.

The total small-signal absorption of the Cr:ZnSe gain medium at 1800 nm was 94%. To remove the unused pump power, the crystal was surrounded with indium foil and held inside a copper holder whose temperature was maintained at 21°C by water cooling. The Cr:ZnSe laser was longitudinally pumped with a continuous-wave (cw) Tm-fiber pump laser operating at 1800 nm. The pump beam was focused inside the gain medium with a converging lens of focal length 10 cm (L in Figure 3.3.1). During KLM operation, either a prism pair (P1 and P2) or a slab (S) was used for dispersion compensation. In the initial phase of the experiments, the cw power performance of the resonator was evaluated in the absence of dispersion compensation elements. As can be seen from Figure 3.3.2, as high as 158 mW of output power was obtained with the 1% output coupler when the input pump power was 2.58 W.

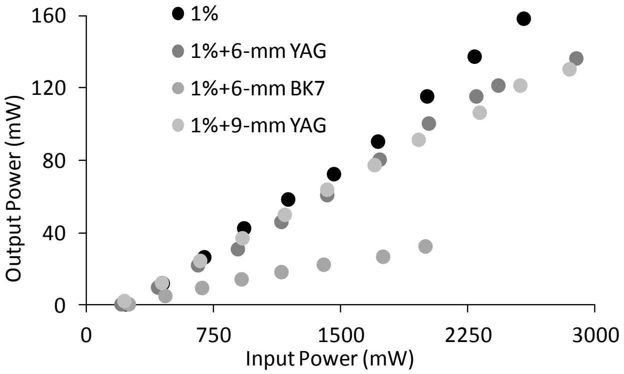

Figure 3.3.2: Continuous-wave power efficiency curves of the Cr:ZnSe laser containing 6 mm-BK7, 6 mm-YAG, and 9mm-YAG slabs. The transmission of the output coupler is 1%.

The corresponding slope efficiency (η_S) was measured to be 6.7%. In the case of the 6% output coupler, the slope efficiency was 14.5% and a maximum output power of 370 mW was obtained with 2.82 W of pump power (See Figure 3.3.3).

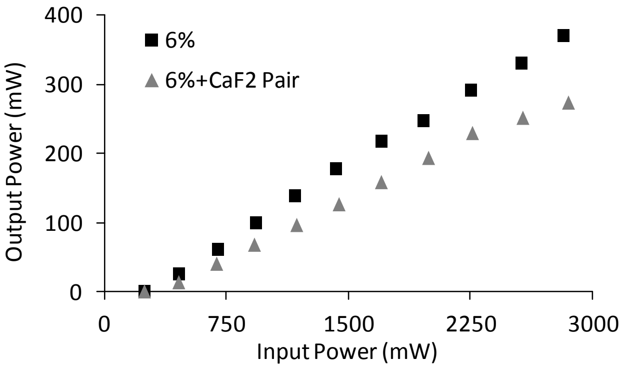

Figure 3.3.3: Continuous-wave power efficiency curves of the Cr:ZnSe laser with a CaF_2 prism pair and 6% output coupler.

In the experiments, soft-aperture Kerr-lens mode locking was employed to initiate the pulse train by optimizing the focusing inside the gain medium and by translating the output coupler. During mode-locked operation, dispersion compensation elements (prism pair or slab) were placed at Brewster incidence in the high reflector arm of the laser. Figures 3.3.2, 3.3.3, and 3.3.4 also show the power performance of the laser with these elements.

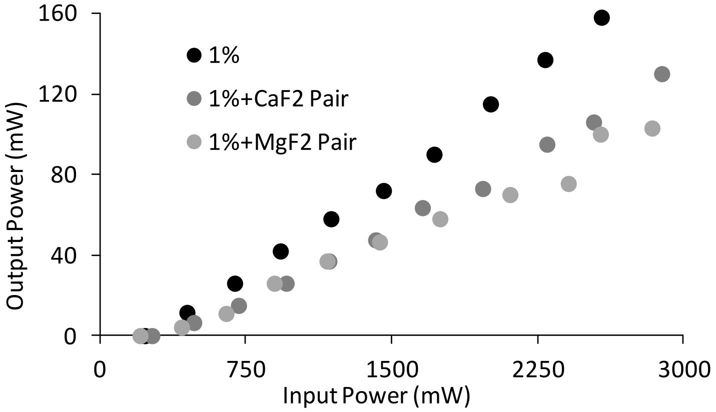

Figure 3.3.4: Continuous-wave efficiency curves of the Cr:ZnSe laser with MgF_2 and CaF_2 prism pairs . The transmission of the output coupler is 1%.

The cavity was further purged with N_2 gas to maintain a relative humidity level around 30% and to minimize instabilities due to water absorption. The spectral and temporal characteristics of the mode-locked pulses were measured with a mid-IR scanning spectrometer and an intensity autocorrelator. Two-photon absorption in a Ge detector was utilized to measure the intensity autocorrelation of the pulses.

3.3.2 Results and Discussion

The power performance of the mode-locked Cr:ZnSe laser was first evaluated with different intracavity dispersion compensation slabs (S in Figure 3.3.1), and prism pairs (P1 and P2 in Figure 3.3.1). Table 3.3.1 lists the estimated insertion loss of the compensation element, net group delay dispersion (GDD) of the resonator containing the compensation element, mode-locked pulsewidth, repetition rate, and time-bandwidth product for each configuration.

Table 3.3.1: Output coupler transmission (T), slope efficiency (η_s), estimated insertion loss (L_{DC}), pulsewidth (τ_P), spectral width ($\Delta\lambda$), central wavelength (λ_P), time-bandwidth product ($\tau_P.\Delta\nu$), calculated group delay dispersion (GDD), third order dispersion (TOD), average output power (P_{av}), repetition rate (f_{rep}), and output pulse energy (W_{out}) of the KLM Cr:ZnSe laser operated with different dispersion compensation schemes. GDD and TOD values were estimated by using the Sellmeier data [86] and dispersion equations [55].

Dispersion Element	**T (%)**	**η_s (%)**	**L_{DC} (%)**	**τ_p (fs)**	**$\Delta\lambda$ (nm)**	**λ_p (nm)**	**$\tau_p.\Delta\nu$**	**GDD (fs^2)**	**TOD (fs^3)**	**Pav (mW)**	**f_{rep} (MHz)**	**W_{out} (nJ)**
6mm-YAG	1	5.4	0.7	116	69	2450	0.404	-1092	14149	31	190	0.16
9mm-YAG	1	5.0	1.0	121	61	2427	0.374	-2164	20068	41	91	0.45
6mm-BK7	1	1.7	8.3	385	27	2361	0.556	-1758	16738	22	91	0.22
MgF2 pair	1	3.7	2.3	95	69	2421	0.335	-1606	18029	40	100	0.40
CaF2 pair	1	5.0	1.0	92	76	2459	0.348	-1767	20550	31	95	0.33
CaF2 pair	6	11.2	2.3	121	63	2451	0.379	-1773	20343	165	95	1.81

The loss introduced by each dispersion compensation element was estimated in two steps (See Chapter 2 for further details on the slope efficiency formula). First, the round-trip loss L_C of the resonator was estimated by comparing the slope efficiencies obtained with two different output couplers in the free-running regime and by using the equation

$$\eta_1 = \frac{\dfrac{T_1}{T_1 + L_C}}{\dfrac{T_2}{T_2 + L_C}}, \tag{3.3.1}$$

here, T_1 and T_2 are the power transmission of the two different output couplers and η_1 is the ratio of the slope efficiencies measured with these two output couplers. In our case, $T_1 = 1\%$ and $T_2 = 6\%$. By using the measured slope efficiencies and Eqn. 3.3.1, L_C was determined to be 1.79%. In the next step, we compared the slope efficiency of the original free-running laser (operated with the output coupler having transmission of T_1) with that of the resonator containing the same output coupler and also the dispersion compensation element. The round-trip loss of the compensator was assumed to be L_{DC}. From the ratio η_2 of the measured slope efficiencies, L_{DC} was estimated by using the equation

$$\eta_2 = \frac{\dfrac{T_1}{T_1 + L_C}}{\dfrac{T_2}{T_2 + L_C + L_{DC}}}. \qquad 3.3.2$$

As can be seen from Table 3.3.1, the worst cw and mode-locked performance was obtained when the 6 mm long BK-7 slab was used for dispersion compensation. In this case, the estimated loss introduced by the slab was 16.3 % and, as can be seen from Figure 3.3.2, only 32 mW of cw output power could be obtained with 2 W of pump power (corresponding slope efficiency=1.72%). Excess loss limited the mode-locked pulse energy to 0.22 nJ and the shortest obtained pulsewidth was 385 fs.

The cw performance of the laser was dramatically improved by going to YAG slabs which have low absorption loss in the operating wavelength range of the Cr:ZnSe laser. For example, the estimated insertion loss of the 6-mm and 9-mm YAG slabs was 1.4 and 1.9%, respectively. In the case of the 6-mm-long YAG substrate, the net GDD of the cavity (-1092 fs^2) was not sufficient to balance the Kerr nonlinearities and double pulsing was routinely observed in the autocorrelation trace. Addition of an extra 3-mm-long YAG plate nearly doubled the net GDD to -2164 fs^2. In this case, double pulsing disappeared and 41 mW of average output power was obtained, corresponding to 0.45 nJ of pulse energy. For the mode-locked resonator containing 9-mm-long YAG slab, the measured spectrum and autocorrelation of the pulses are shown in Figures 3.3.5 (a) and (b), respectively.

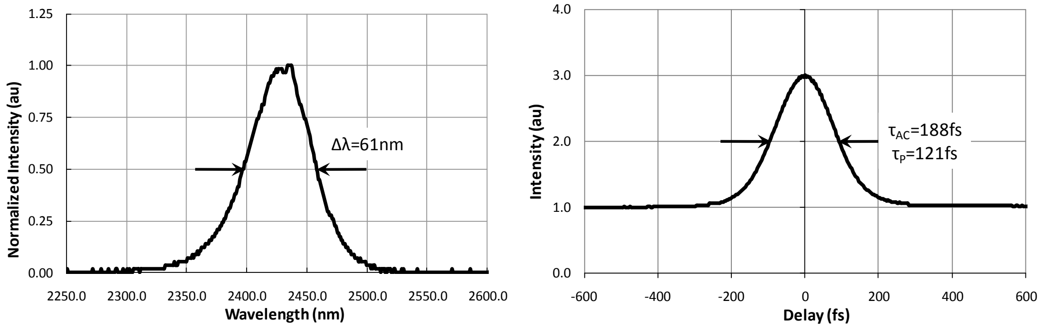

Figure 3.3.5: (a) Measured spectrum and (b) autocorrelation of the pulses generated from the KLM Cr:ZnSe laser containing a 1% output coupler and a 9-mm YAG slab.

By assuming a sech^2 pulse profile, the pulsewidth (FWHM) was determined to be 121 fs. The spectral bandwidth was 61 nm, giving a time-bandwidth product of 0.374.

Although a single-crystal YAG slab can be used with very low insertion loss to compensate for dispersion around 2400 nm, the fixed length of the substrate prevents continuous adjustment of the total GDD. This can be obviated by using prism pairs where GDD can be varied by changing the prism separation and/or prism material insertion. In our experiments, we tested the performance of two types of prism pairs (MgF$_2$ and CaF$_2$) which have high transmission around 2400 nm. In each case, the prisms were inserted at Brewster incidence on the high reflector arm of the cavity. They were further mounted on translation stages to control the material insertion. Figure 3.3.4 shows the cw power performance of each prism pair taken with the 1% transmitting output coupler. As can be seen from Table 3.3.1, the insertion loss of the CaF$_2$ prism pair (2.0%) was lower than that of the MgF$_2$ prism pair (4.6%) due to the better surface quality of the former. In particular, the resonator containing the CaF$_2$ prism pair and 1% output coupler produced 73 mW of output power with 1.97 W of pump power, which was 6 mW higher than that obtained with the MgF$_2$ prism pair. For both cases, the net GDD of the cavity was in the range of –(1600-1800) fs^2, resulting in the generation of sub-100-fs pulses. With the CaF$_2$ prism pair, slightly shorter pulses with a duration of 92 fs were generated. The pulse energy and time-bandwidth product were 0.33 nJ and 0.348, respectively. For the mode-locked resonator containing the CaF_2 prism pair, the measured spectrum and autocorrelation of the pulses are shown in Figures 3.3.6 (a) and (b).

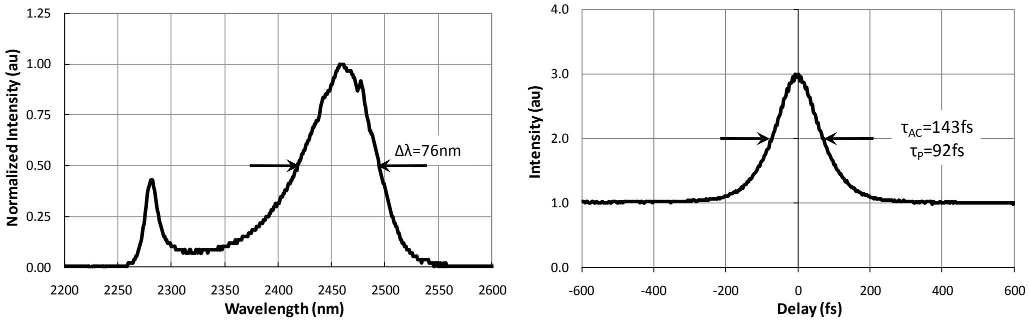

Figure 3.3.6: (a) Measured spectrum and (b) autocorrelation of the pulses generated from the KLM Cr:ZnSe laser containing a 1% output coupler and a CaF_2 prism pair.

Finally, in order to extract higher pulse energies from the laser, the 1% output coupler was replaced with a 6% output coupler while keeping the CaF_2 prism pair in the high reflector arm of the laser. As can be seen from Table 1, this gave as high as 165 mW of average output power during mode-locked operation, corresponding to 1.81 nJ of pulse energy at the pulse repetition frequency of 95 MHz. As can be seen from the autocorrelation and spectrum measurements displayed in Figures 3.3.7(a) and (b), the temporal and spectral width of the pulses were 121 fs and 63 nm, giving a time-bandwidth product of 0.379.

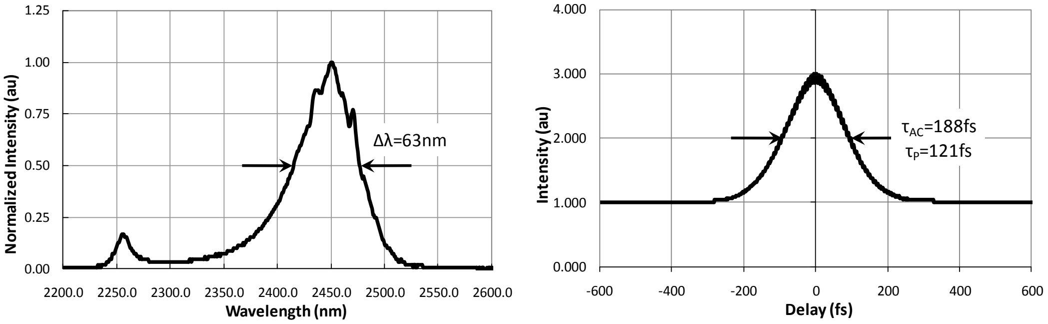

Figure 3.3.7: (a) Measured spectrum and (b) autocorrelation of the pulses generated from the KLM Cr:ZnSe laser containing a 6% output coupler and a CaF_2 prism pair.

In this case, no double pulsing was observed with a fast detector that monitored the pulse train in the nanosecond time scales or with the autocorrelator.

The KLM operating point of each configuration can be analyzed by using the soliton area theorem that relates the output pulsewidth to the pulse energy, GDD, and nonlinear refractive index [53]. In particular, we can determine the nonlinear refractive index n_2 from the experimentally measured parameters of the mode-locked laser by using the well known equation

$$\tau = \frac{4|D|}{W\delta}. \tag{3.3.3}$$

Here, τ is the pulsewidth divided by 1.76, W is the intracavity pulse energy, D is the net GDD of the cavity, and δ is the nonlinear coefficient given by

$$\delta = \frac{2\pi}{\lambda} n_2 \frac{2L_C}{A_{eff}}. \tag{3.3.4}$$

In Eqn. 3.4, λ is the center wavelength of the spectrum, L_C is the single-pass length of the gain medium, and A_{eff} is the effective area of the laser beam inside the gain medium given by

$$A_{eff} = \frac{n_0 \pi \omega_{rms}^2}{2}. \tag{3.3.5}$$

In Eqn. 3.5, n_0 is the linear refractive index and ω_{rms} is the root-mean-squared spotsize of the laser beam. In the calculation of ω_{rms}, we employed the standard ABCD analysis to first determine the beam waist (ω_0) inside the gain medium. Here, it was assumed that the cavity configuration remains near the center of the stability region during KLM operation and ω_{rms} was calculated by using the equation

$$\omega_{rms} = \sqrt{\frac{1}{L_C}\int_0^{L_C} \omega_0^2 \left(1 + \left(\frac{z - z_f}{z_0}\right)^2\right) dz}. \tag{3.3.6}$$

Above, z_f is the location of the laser beam waist within the crystal and z_0 is the Rayleigh range ($z_0 = n_0\pi\omega_0^2/\lambda$). The parameters ω_0, and ω_{rms} were determined to be 34.9 and 35.5 μm, respectively. By using this procedure, the nonlinear refractive index n_2 was determined for each of the six KLM configurations tested in the experiments and the results are tabulated in Table 3.3.2.

Dispersion Element	**OC (%)**	**n_2 (m^2/W)**
6mm-YAG	1	$1.49\text{x}10^{-18}$
9mm-YAG	1	$1.01\text{x}10^{-18}$
6mm-BK7	1	$5.12\text{x}10^{-19}$
MgF2 pair	1	$1.07\text{x}10^{-18}$
CaF2 pair	1	$1.52\text{x}10^{-18}$
CaF2 pair	6	$1.55\text{x}10^{-18}$
	Average:	$1.2\text{x}10^{-18}$

Table 3.3.2: The nonlinear refractive index (n_2) values determined by using the soliton area theorem for the different mode-locking configurations tested in the experiments.

The nonlinear refractive index n_2 came to $(1.2 \pm 0.2) \times 10^{-18}\text{m}^2/\text{W}$ which is close to the previously reported value of $1.7 \times 10^{-18}\text{m}^2/\text{W}$ [73].

In conclusion, we have utilized four different cost-effective and practical dispersion compensation methods for Cr:ZnSe lasers operated in the Kerr-lens mode-locked regime. Our results show that, in the case of BK7, although material dispersion has the correct sign to compensate for Kerr nonlinearities, the excessive material absorption leads to poor power and mode-locked performance. The highest pulse energy was obtained with a 6% output coupler and a CaF_2 prism pair, where as high as 1.81 nJ was obtained with 2 W of pump power. When a 1% output coupler was used with the CaF_2 prism pair, higher intracavity energy led to the generation of the shortest pulses (duration of 92 fs FWHM) in the experiments. Overall, YAG slabs could be used with lower insertion loss in comparison with prism pairs. On the other hand, the prism pair allowed for continuous adjustment of the cavity dispersion. Finally, by using the soliton area theorem, we estimated the nonlinear refractive index (n_2) of ZnSe as $(1.2\pm0.2)\times10^{-18}$ m^2/W, which comes close to the previously reported value of 1.7×10^{-18} m^2/W.

Chapter 4: Nonlinear optical characterization of graphene

4.1 Introduction

Graphene is the name of a carbon allotrope in which carbon atoms form a two dimensional honeycomb lattice structure as illustrated in Figure 4.1.1.

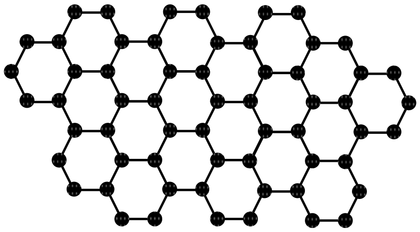

Figure 4.1.1: Illustration of honeycomb atomic structure of graphene.

Until 2004, it was believed that any 2-dimensional structure cannot remain stable in its free form, due to the tendency to evolve into a thermodynamically more stable 3 dimensional form [87]. In 2004, two scientists from Manchester University, Geim and Novoselov, successfully showed that few-layer graphene can be isolated from bulk graphite [88]. In the following years, researchers revealed many remarkable physical properties of graphene, which have found wide variety of applications in many fields [89].

Graphene has unique optical properties owing to the point gap E-k diagram as illustrated in Figure 4.1.2.

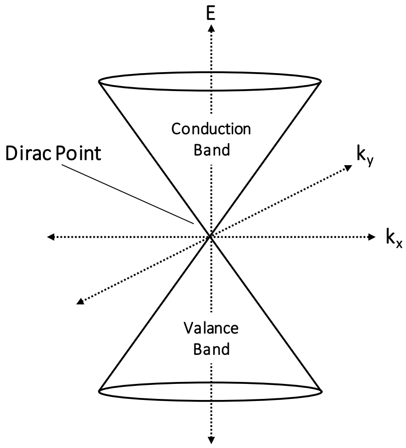

Figure 4.1.2: E-k diagram of graphene near Dirac point.

Electrons and holes in graphene obey the Dirac relativistic equation for ½ spin particles. So, they have the following dispersion relation near the Dirac point [90]:

$$E_{2D}(k_x, k_y) = \hbar \nu_F \sqrt{k_x^2 + k_y^2}, \tag{4.1.1}$$

where ν_F is the Fermi velocity ($\approx 10^6 m/s$) and k_x, k_y are the wave vectors of the electrons. Notice that the dispersion relation of electrons in graphene is similar to $E(k) = \hbar ck$, which is the dispersion relation of a photon, hence electrons and holes in graphene have zero effective mass near Dirac point, and they are called massless Dirac fermions. Due to this unique zero band gap energy as well as the linear dispersion relation, the absorption of a single layer free standing graphene is nearly independent of wavelength and can be expressed as [91]:

$$A = \pi\alpha \approx 2.3\%, \tag{4.1.2}$$

where $\alpha = 1/137$ is the fine structure constant. Therefore, one can roughly estimate the number of transferred graphene layers by simply measuring the optical absorption of a prepared sample. In 2006, Ferrari et al. proposed the use of Raman spectroscopy in the characterization of the quality of produced graphene layers [84]. In Raman spectroscopy, a sample is illuminated with a monochromatic light source and the amount of energy lost due to the excitation of vibrational modes (phonons) is determined by simply measuring the wavelength shift of the scattered light. Before proceeding on the description of the Raman spectrum of graphene, crystal structure and phonon properties of graphene will be summarized. Figure 4.1.3 (a) shows the Brillouin zones of graphene where the zone centers are labeled as the Γ-points, corners as K-points, the middle of corners as M-points, and $\overrightarrow{a_1}$, $\overrightarrow{a_2}$ are the unit vectors [92, 93]. Dirac cones shown in Figure 4.1.2 are formed at the corners of each unit cell (See Figure 4.1.3 (b)).

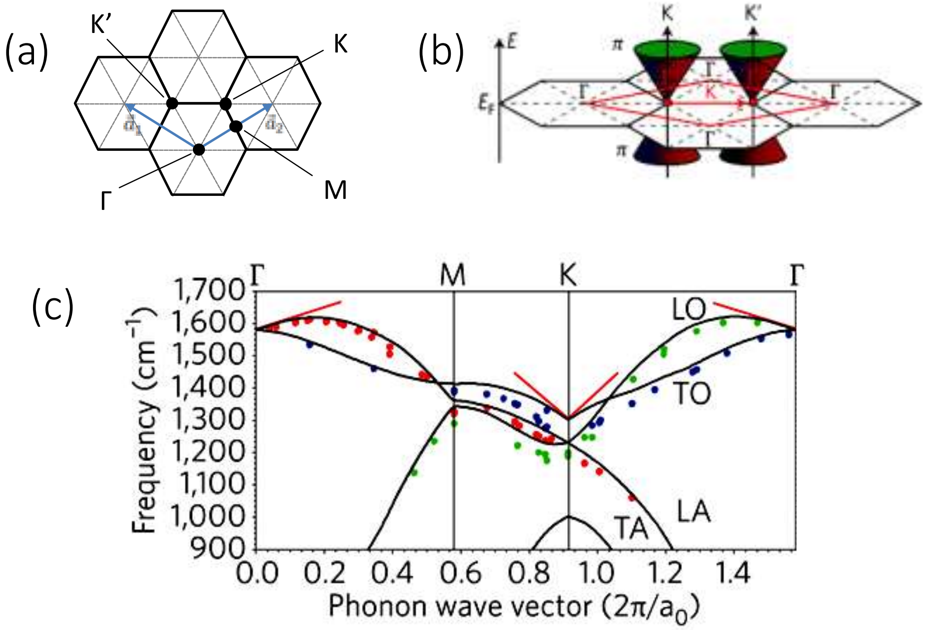

Figure 4.1.3: (a) Schematic illustration of the Brillouin zones of graphene, (b) together with the Dirac cones at K- and K'-points. (c) Calculated and measured phonon dispersion curves for monolayer graphene [92, 93].

In all ordered crystalline structures, atoms oscillate around an equilibrium position, which gives rise to mechanical waves that propagate through the lattice with a definite energy and momentum. The number of normal modes resulting from lattice vibrations is governed by the number of atoms (N) contained in the unit cell of the crystal. In the case of single-layer graphene, it contains two carbon atoms in the unit cell $(N = 2)$, hence it has four in plane and two out of plane modes at Γ ($3N = 6$), two of which is doubly degenerate (E_{2g} and B_{2g} symmetry) [93]. Calculated and measured phonon dispersion curves at K-, M- and zone center Γ-points are plotted in Figure 4.1.3 (c), which is a useful tool in interpreting the Raman spectrum of graphene. LO and TO stands for longitudinal and transverse optical phonons, LA and TA stands for the longitudinal and transverse acoustic phonons in the figure [92].

A typical Raman spectrum of a monolayer graphene sheet is plotted in Figure 4.1.4 [39]. It contains four distinct peaks which are commonly labeled as the G, G'(2D), G* and D bands.

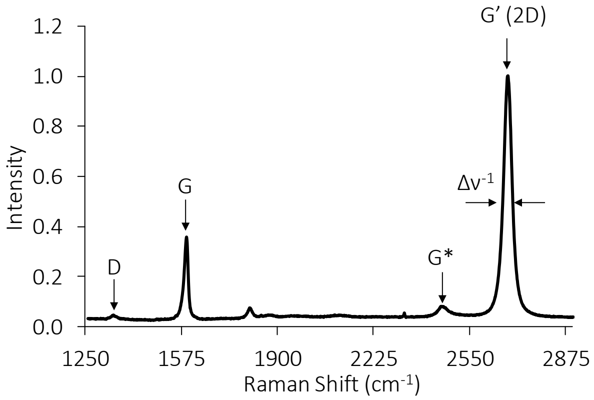

Figure 4.1.4: A typical Raman spectrum of a monolayer high quality graphene transferred on CaF_2.

The only first order Raman scattering peak matches with the doubly degenerate zone center (Γ-point) phonon in Figure 4.1.3 (c) which is the G peak at 1580 cm^{-1}. D and G' (2D) peaks originate from second order processes. Ideally, in a sample with no defects, the TO phonon near the K point is forbidden (1350 cm^{-1}), i.e. Raman inactive. However, for defected edges of the sample, a defect assists the transition and it becomes visible in the Raman spectrum. Hence, a small D peak in the Raman spectrum indicates that the sample under investigation has good crystal quality. G' peak results from the two TO phonons near the K point (2700 cm^{-1}). For monolayer graphene, the G' peak can be fitted with a single Lorentzian distribution function. As the number of layers increases, the full width half maximum (FWHM) increases and the intensity of the peak decreases due to having an increasing number of Lorentzians. By inspecting the FWHM of G’ (2D) peak and the intensity ratios of the G and G’ (2D), one can precisely determine the number of layers. In summary, simply by looking at the Raman spectrum of a graphene sample, one can determine the 1) number of layers and 2) the crystal quality. The ratio of the intensities of G/G’ together with the linewidth of G’ peak provide the number of transferred layers, where the intensity ratio of D/G provides information about the crystal quality.

In earlier discussions, we introduced the lattice structure as well as the E-k diagram of graphene, and noted that its conduction and valance bands form bandgapless Dirac cones at K and K’ points (See Figure 4.1.3 (b)), which provides a constant linear absorption from the visible to the infrared with a little deviation from 2.3% [91]. It is important to evaluate the non-equilibrium dynamics of electrons and holes in understanding the optical properties of graphene [94]. Ultrafast transient spectroscopy is a suitable tool for probing the carrier dynamics. In this technique femtosecond pulses excite the electrons from valance to conduction band through dipole allowed π-π^* transition, while probe pulses at a certain photon energy monitor the changes in the transmission of the sample as a function of the delay between pump and probe pulses.

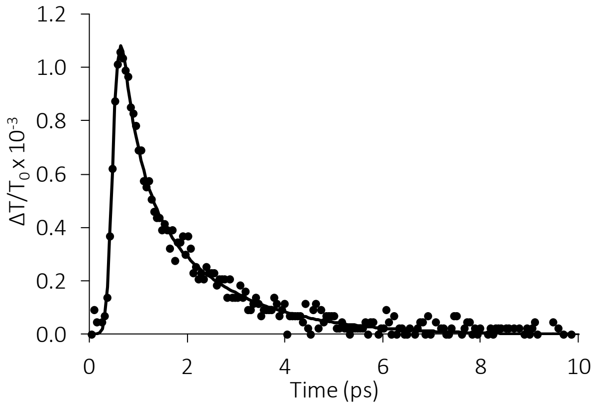

Figure 4.1.5: Typical pump-probe trace of a monolayer graphene.

In Figure 4.1.5, a typical measured transient absorption trace as a function of time is plotted together with the bi-exponential fit. Here $\Delta T/T_0 = (T - T_0)/T_0$, where T and T_0 are the transmission values of the sample with and without the excitation pulse, respectively. Photo-excited carriers relax to equilibrium in two distinct time scales, given by the fast (τ_1) and slow (τ_2) time constants. Typical fast and slow time constants for monolayer graphene are measured in the range of 100-200 fs, 0.4-1.7ps, respectively [56]. The following model is proposed in describing the pump-probe curve plotted in Figure 4.1.5. After photo-excitation takes place, excited carriers block the further absorption of pump photons due to Pauli blocking and hence, the transmission of the sample at the probe photon energies increases rapidly and reaches the peak of the transient curve, which corresponds to stage (b) in Figure 4.1.6. Following excitation, because of high carrier density in the conduction band, electrons collide with each other and lose most of their energy through intraband carrier-carrier scattering, which is represented as (c) in Figure 4.1.6. Later, in step (d) carriers lose their remaining energy to lattice vibrations through carrier-phonon scattering and equilibrate at their initial state [56].

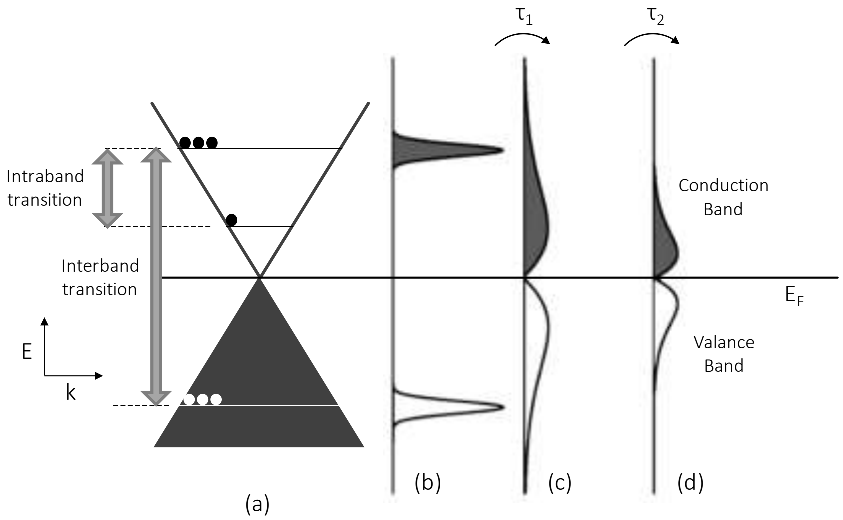

Figure 4.1.6: (a) An illustration of the interband and intraband transitions in graphene, and (b)(c)(d) temporal evolution of photo-excited carriers [56].

Until now, we have assumed that the Fermi level is located at the center of the conduction and valance bands (Dirac point). However in reality because of unintentional doping, which could be due to the interaction between the graphene layer and the substrate or the excess carriers coming from the production stage, the Fermi level can be shifted into the valance or conduction band, depending on the type of dopant (n or p) [95-97]. Figure 4.1.7 can be used in describing the effect of carrier doping on the optical properties of graphene, where (a) and (b) show the undoped and doped E-k diagram of monolayer graphene, respectively. In state (a), photons with photon energy of $2E_F$ are readily absorbed. However, in the case of state (b), because of electron doping, Fermi level is shifted into the conduction band and further absorption of photons with photon energy of $2E_F$ is blocked due to the Pauli blocking ($E_F < E_{F'}$).

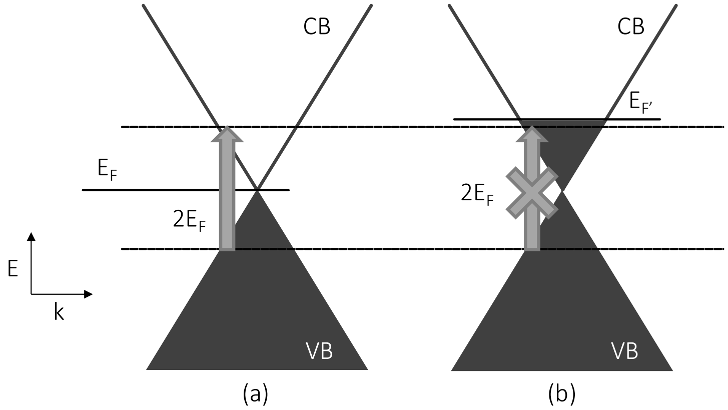

Figure 4.1.7: (a) Undoped and (b) doped E-k diagram of monolayer graphene.

Such a mechanism can be effectively used in altering the optical properties of graphene. To date, Fermi level was shifted up to 0.45eV by means of a gated graphene based optical modulators [98]. Because of the limitations resulting from the dielectric breakdown of materials, further shift in the Fermi level corresponding to the transitions in the visible and near infrared range cannot be controlled by using dielectric capacitors [99].

Electrolyte gating of graphene by using supercapacitors was proposed to overcome the limitations mentioned above [100, 101]. In this scheme, an ionic liquid is sandwiched in between monolayer graphene-coated quartz plates as shown in Figure 4.1.8 (a), where graphene plates act as electrodes. Applied gate voltage polarizes the ionic liquid, hence few nanometer thick electrical double layers (EDLs) are formed near the graphene surfaces as shown in Figure 4.1.8 (b).

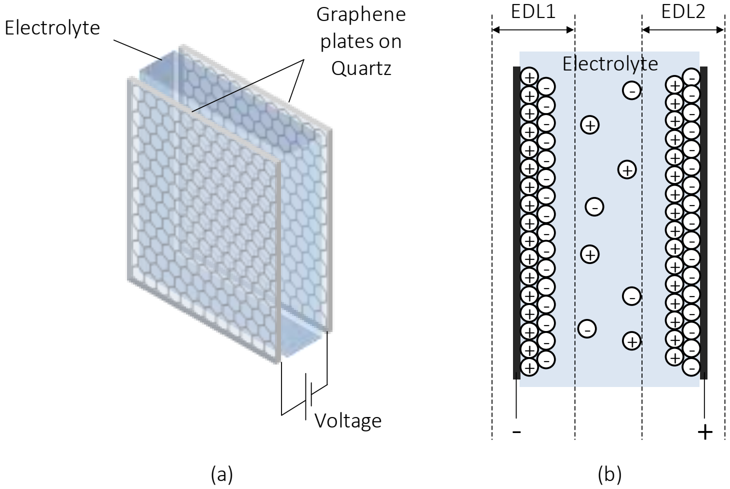

Figure 4.1.8: (a) Schematic illustration of electrolyte gating of graphene (b) electrical double layer (EDL) formation near graphene plates.

Notice that the top and bottom EDLs act as capacitors connected in series, both have few nanometer separation and large surface area which generate very large electric fields. As a result, the graphene plates are electrostatically doped with either electrons or holes depending on the polarity of the applied voltage. Therefore, the magnitude of the Fermi level shift into the conduction or valance band can be controlled by changing the applied bias voltage. The amount of the shift is given by

$$E_F' - E_F = \Delta E_F = \hbar v_F \sqrt{\pi n}\,, \qquad 4.1.3$$

where $v_F$is the Fermi velocity (1.1×10^8 cm/s), n is the carrier density, and $\hbar$ is the Planck's constant [99]. Due to Pauli blocking, this shift in the Fermi level completely suppresses the absorption of the device for wavelengths (λ) with photon energy below $2|E_F|$, in other words for $\lambda < hc/2|E_F|$. The resulting voltage dependent change in the optical transmission occurs at relatively low bias voltages of a few volts, due to the use of an electrolyte with a high dielectric constant. The reversible doping scheme alters the linear/nonlinear absorption, and saturation characteristics of the graphene [57].

In the following Section, the experimental setup that we used during the nonlinear optical characterization experiments will be described. Later, in Sections 4.3.1 and 4.3.2, we evaluated the nonlinear absorption and transient characteristics of monolayer graphene on different substrates, and graphene-based supercapacitor device, respectively.

4.2 Nonlinear optical characterization experiments with graphene and graphene-based supercapacitors

4.2.1 Graphene on different substrates

Three samples, investigated in the experiments, were synthesized with a similar method described in [102]. Prepared samples were transferred onto yttrium aluminum garnet (YAG) and quartz substrates in collaboration with Dr. Coskun Kocabas at Bilkent University and transferred on calcium fluoride (CaF_2) substrate in South Korea, in collaboration with Prof. Fabian Rotermund. The optical characterization of three samples was performed at Koç University Surface Science and Technology Center (KUYTAM).

In order to characterize the linear and non-linear optical properties of monolayer graphene samples coated on quartz, YAG and CaF_2 substrates, steady-state optical transmission, Raman, and ultrafast transient absorption spectroscopy methods were used. The linear optical transmission data were measured with a typical spectrophotometer (Shimadzu 3101-PC) in the 700–2500 nm range. In order to check the quality of the samples, we further measured the Raman spectrum of each sample by using Renishaw inVia Raman microscope at the pump wavelength of 532 nm. And finally, in order to measure the transient absorption and saturation of the samples, we used a commercial transient absorption spectrometer (Ultrafast Systems, HELIOS). Figure 4.2.1 shows a schematic of the setup where pump pulses were generated from an OPA system, and for the probe pulses, a near-infrared continuum spanning from 900nm to 1400nm was used. In order to generate the infrared continuum, 800 nm light coming from a Ti:Sapphire laser was focused on a CaF_2 substrate (by using a lens labeled as L2 in Figure 4.2.1).

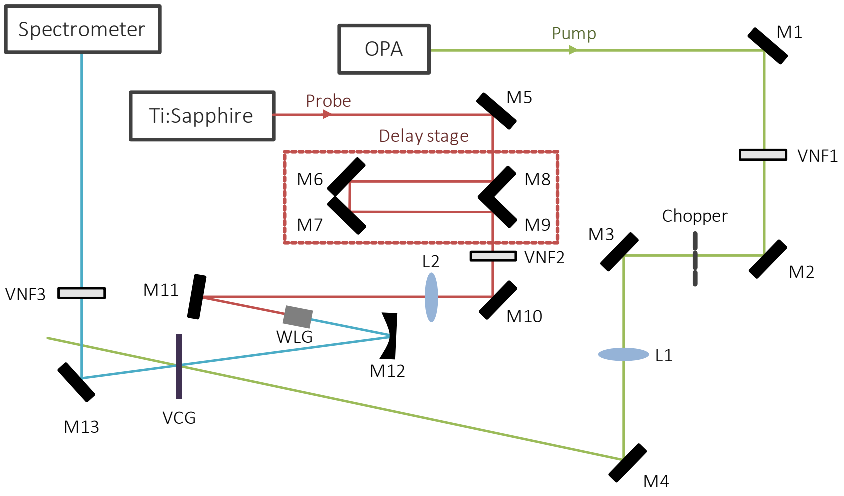

Figure 4.2.1: Schematic illustration of transient absorption spectrometer setup.

4.2.2 Voltage controlled graphene

The voltage controlled graphene based supercapacitor structure was prepared at Bilkent University in collaboration with Dr. Coskun Kocabas. The graphene supercapacitor was fabricated by using two monolayer large-area graphene electrodes, each synthesized via chemical vapor deposition and transfer-printed onto a 1-mm-thick, 1-inch-diameter quartz substrate. The 100-µm spacing between the two graphene electrodes was filled with an electrolyte, (Diethymethyl (2-methoxyethyl) ammonium bis (trifluromethylsulfony) imide [DEME][TFSI]), which has a relative dielectric constant of $\epsilon_r = 14$ [103]. A sketch of the graphene supercapacitor is shown in Figure 4.1.8. We measured the voltage dependent optical transmission, pump-probe response, and absorption saturation of the sample.

4.3 Results and Discussions

In this section, the results we obtained will be discussed in two sub sections titled as: graphene on different substrates and voltage controlled graphene.

4.3.1 Graphene on different substrates

First, we measured the optical transmission of each sample to roughly determine the number of layers transferred on the samples. By looking at Figure 4.3.1, it turns out that all three samples have almost constant transmission from visible to infrared. When we subtract the average background coming from the substrate (Fresnel reflections), the remaining transmission resulting from the graphene samples are 2.1%, 1.3% and 1.8% for quartz, YAG, and CaF_2 substrates, respectively.

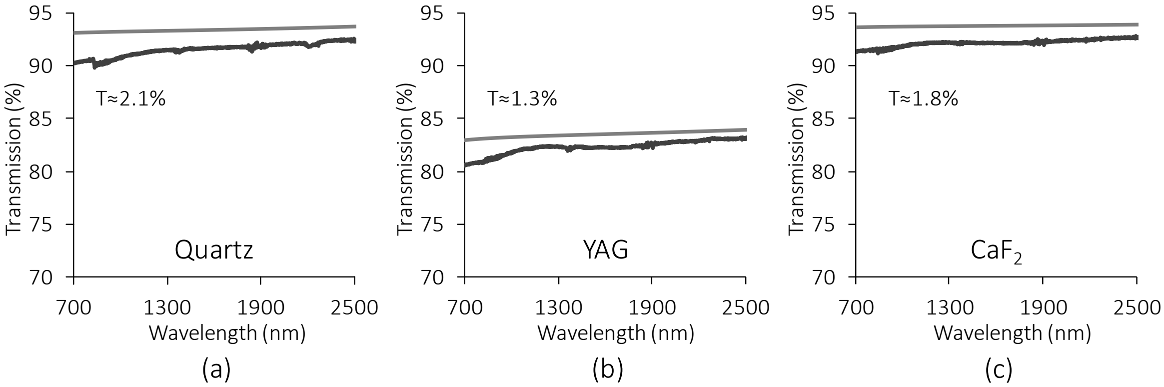

Figure 4.3.1: Optical transmission data of different samples coated on (a) quartz, (b) YAG and, (c) CaF_2.

From the literature, we know that the steady state transmission of the free standing graphene was ideally 2.3%. However, studies showed that the total transmission can slightly deviate from the theoretical value due to the interactions between the substrate and the graphene [95, 104].

As we mentioned in the Introduction section, Raman spectroscopy is a widely used tool in further characterizing the quality of graphene samples [84]. Measured Raman spectra of the samples on quartz, YAG and CaF_2 substrate were plotted in Figure 4.3.2 (a), (b) and (c), respectively.

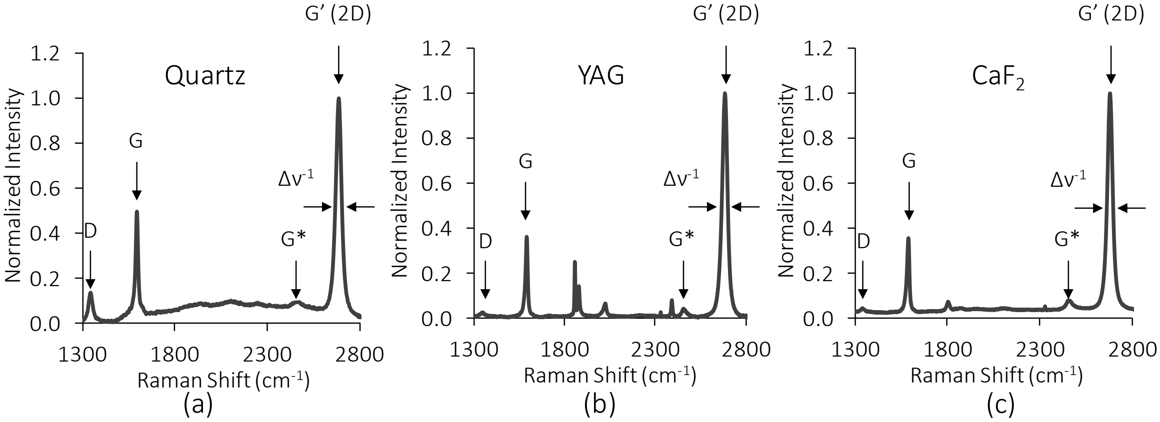

Figure 4.3.2: Measured Raman spectra of different graphene samples transferred on (a) quartz, (b) YAG, and (c) CaF_2.

Typical graphene peaks around 1350 cm^{-1}, 1580cm^{-1} and 2700cm^{-1} are observed as expected. These peaks are labeled as the D, G, and G' (2D) peaks, respectively. The quality of the graphene sample can be deduced from the D/G and, G/G' peak ratios together with the linewidth of G' (2D) peak. Calculated values of the ratios and the linewidth of G'(2D) and G peaks are tabulated in Table 4.3.1.

Table 4.3.1: Tabulated peak ratios and linewidth of 2D and G peaks for graphene transferred on quartz, YAG and CaF_2 substrates.

Substrate	D/G	G/G'	Δν of 2D (cm^{-1})	Δν of G (cm^{-1})
Quartz	0.26	0.5	37	15
YAG	0.07	0.36	35	14
CaF_2	0.12	0.36	33	15

By looking at the values of G/G' ratio and the linewidth of G' (2D) peak, transferred graphene layers are nearly monolayer in all three cases. Also D/G ratios suggest that the graphene transferred on quartz substrate has poor crystal quality compared to the others. Furthermore by inspecting the peak positions of G, and 2D peaks, we can easily monitor the level of unintentional doping [95, 96]. Unintentional doping blocks the absorption of incoming photons at infrared wavelengths due to Pauli blocking. Hence, it is an undesirable effect during the production. Table 4.3.2 summarizes the measured Raman peak positions of graphene on each sample together with the free standing values reported in ref [60].

Table 4.3.2: Tabulated peak positions for graphene transferred on quartz, YAG and CaF_2 substrates.

Substrate	D (cm^{-1})	G (cm^{-1})	G’ (2D) (cm^{-1})
Free-standing[95]	1350	1580	2700
Quartz	1344	1595	2686
YAG	1345	1590	2684
CaF_2	1344	1592	2680

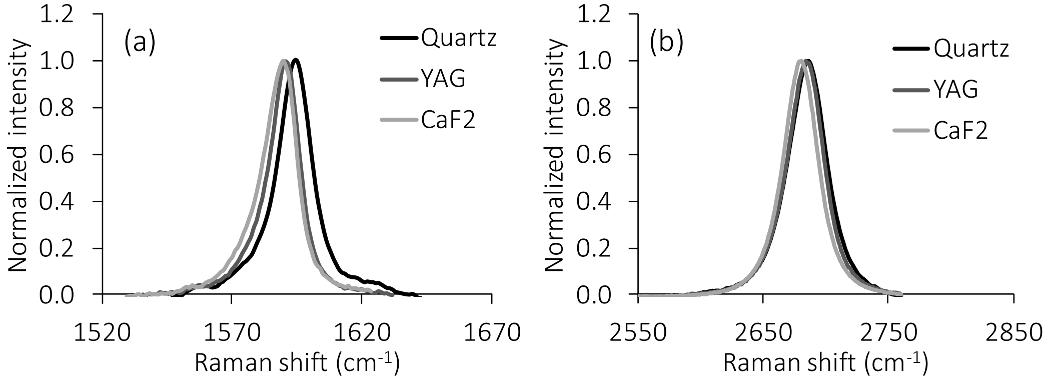

Figure 4.3.3: (a) G and (b) G’ (2D) peak positions for monolayer graphene on quartz, YAG, and CaF_2 substrates.

According to the literature, the peak position of the G band red-shifts for increasing doping concentration independent of the type of dopant (n or p) [95, 96]. Hence from Table 4.3.2, graphene transferred on quartz substrate is the most unintentionally doped sample compared to the others. Such doping can result from both interactions between the substrate and the graphene layer, as well as during the production stage. Similarly, the intensity of G peaks doesn't change with the doping, where the intensity of G’ (2D) peak decreases. As a result, the peak intensity ratio of G/G’ increases with increasing doping concentration. Table 4.3.1 lists the calculated intensity ratios of G/G', as expected from the earlier results. The highest value was obtained for the graphene transferred on quartz substrate. In summary, Raman analysis showed that the graphene layer transferred on the quartz substrate had the poorest crystal quality.

The measured transient absorption curves at 1250 nm for monolayer graphene on quartz, YAG and CaF_2 substrates are shown in Figure 4.3.4 (a), (b) and (c), respectively.

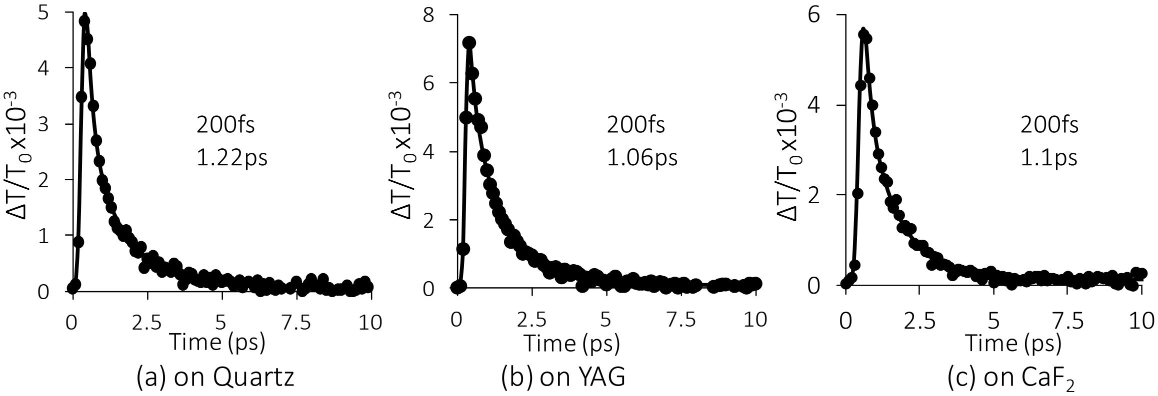

(a) on Quartz (b) on YAG (c) on CaF_2

Figure 4.3.4: Transient absorption curves measured at 1.25μm for graphene on (a) quartz, (b) YAG, and (c) CaF_2 substrates.

As we introduced in the introduction section, graphene exhibits a bi-exponential lifetime decay. The fast time constant is related to the fast cooling of the excited carriers through carrier-carrier scattering, and the slow time constant is associated with carrier-phonon scattering and the recombination of electrons and holes. From literature, the fast time constant for monolayer graphene was measured as 200fs [56, 94]. Since the excitation pulse duration (≈100 fs) is comparable with the fast time constant of graphene (≈200 fs), it cannot be resolved. Hence, we kept the fast time constant as 200fs and obtained slow time constants around 1ps for all three decay curves as a result of the bi-exponential fit to the data.

Finally, in order to determine the saturable absorber properties of the samples, such as the modulation depth (ΔT), saturation fluence (J_{sat}), insertion loss (L), and non-saturable loss

(T_{ns}), we measured the saturation curves of the samples which are plotted in Figure 4.3.5 together with the theoretical fits (See Section 2.3.3 for further details on the fitting procedure).

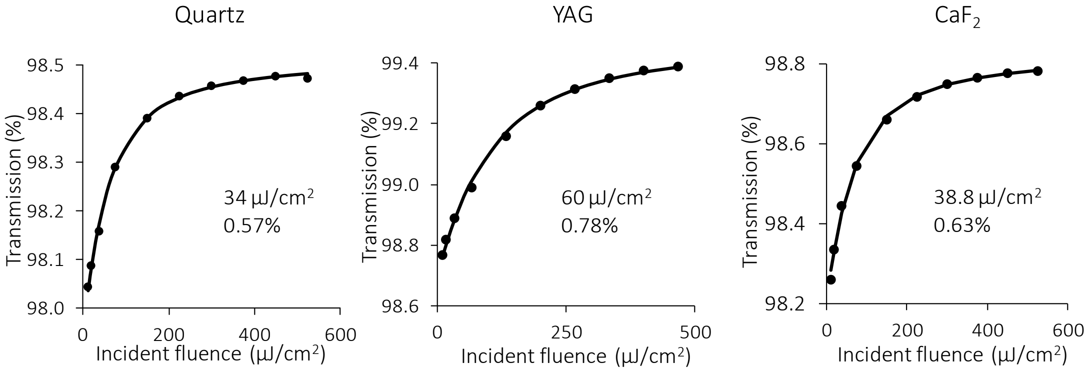

Figure 4.3.5: Measured saturation curves of the samples on quartz, YAG and CaF_2 substrates.

Note that the modulation depth is basically the difference in the transmission under low and high incident fluence, which is also called as the saturable loss. The non-saturable loss is the remaining loss coming from the absorber that cannot be saturated. Finally, the insertion loss (L) is the sum of modulation depth and the non-saturable loss. The results that we have obtained from the theoretical fits are summarized in Table 4.3.3.

Table 4.3.3: Summary of the saturation fluence, modulation depth, non-saturable loss and insertion loss results extracted from the theoretical fit to the saturation data.

Substrate	Saturation fluence (J_{sat})	Modulation depth (ΔT)	Non-saturable loss (T_{ns})	Insertion loss (L)
Quartz	34 μJ/cm^2	0.6%	1.5%	2.1%
YAG	60 μJ/cm^2	0.8%	0.5%	1.3%
CaF_2	39 μJ/cm^2	0.6%	1.2%	1.8%

By looking at these results, graphene transferred on quartz and CaF_2 substrate has comparable saturation fluence and modulation depth with the literature [13]. However in the case of the YAG substrate, the saturation fluence increased by a factor of two in comparison with the quartz and CaF_2 results. We further used the samples on quartz and YAG in the mode locking of an extended cavity Cr:forsterite laser [105, 106]. Since the intracavity power of the laser was well above the saturation fluence determined for both samples, we did not see any difference in the mode locking results.

4.3.2 Voltage controlled graphene

The change in the optical transmission of the voltage controlled saturable absorber (VCG-SA) as a function of applied voltage is shown in Figure 4.3.6 (a). In this figure, $\Delta T/T_0$ is the normalized change in the transmission with respect to the transmission T_0 at zero bias.

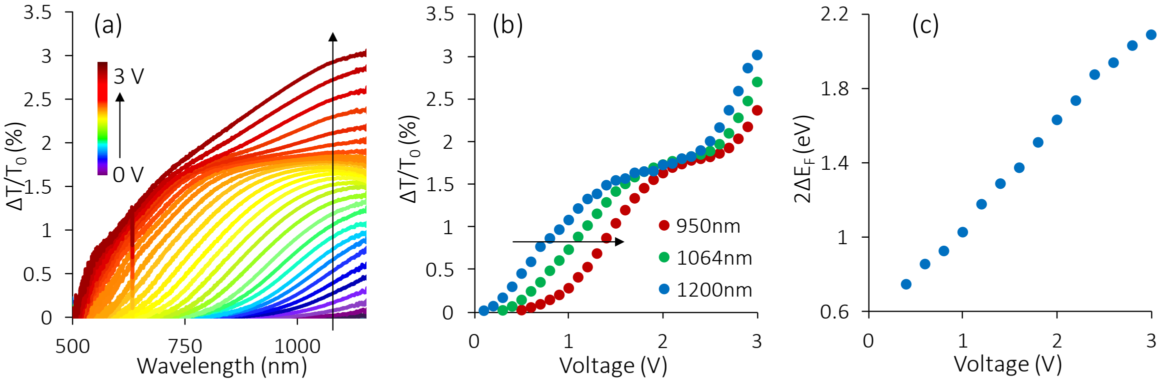

Figure 4.3.6: (a) The variation of the normalized change of the optical transmission of the graphene electrodes as a function of wavelength at different bias voltages in the 0-3V range. (b) Measured variation of the fractional change in the optical transmission as a function of the bias voltage at the wavelengths of 950, 1064 and 1200 nm. (c) The estimated Fermi level shift of the device as a function of the bias voltage.

From Figure 4.3.6 (a), the maximum change in the fractional transmission of two graphene layers was determined to be 3% at 1200nm. Figure 4.3.6 (b) further shows the variation of the normalized transmission at 950, 1064 and 1200 nm as a function of the bias voltage. In the actual supercapacitor, a more complicated two-step response of the transmission was observed as a function of the applied bias voltage, which could be probably attributed to the asymmetric ionic strengths and different ionic radii of the cations and anions of the electrolyte [99, 107]. Figure 4.3.6 (c) shows the variation of the effective Fermi energy shift (ΔE_F) of the device as a function of the bias voltage, which was deduced from the fractional optical transmission data. The effective Fermi energy shift linearly scales with the applied voltage, meaning that higher applied bias voltages are required to modulate the transmission at shorter wavelengths. With this specific electrolyte, the effective Fermi level of the device could be shifted by up to 1.2 eV at a voltage bias of only 3V, enabling the use of this supercapacitor as a modulator down to the wavelength of 500 nm in the visible range.

The ultrafast and nonlinear optical responses of the VCG-SA were investigated by using a time-resolved pump probe spectrometer (HELIOS, Ultrafast Systems). Pump (λ_{pump}=700nm) and probe (λ_{probe}=1250nm) pulses were obtained from a tunable optical parametric amplifier (TOPAS, Spectra Physics), both were pumped with 2 mJ, 100 fs pulses at a pulse repetition rate of 1 kHz from a commercial Ti:sapphire chirped-pulse amplifier (Spitfire ACE, Newport-Spectra Physics).

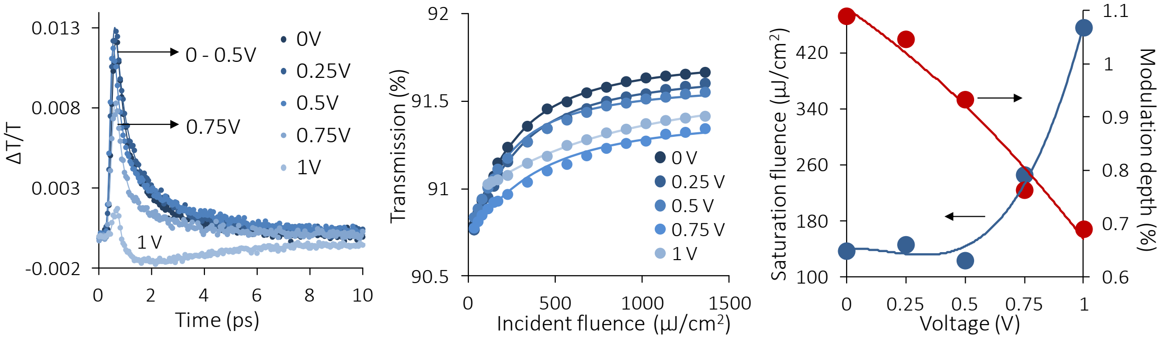

(a) (b) (c)

Figure 4.3.7: (a) Ultrafast response of the graphene-based supercapacitor at the probe wavelength of 1250 nm for different bias voltages. (b) Measured change of the optical transmission as a function of the incident light fluence at 700 nm. (c) Measured variation of the saturation fluence and modulation depth at 1250 nm as a function of the bias voltage.

Pump-probe measurements are shown in Figure 4.3.7 (a) for applied bias voltages from 0.5 to 1V. Up to an applied voltage of 1V, the ultrafast response of the graphene has similar dynamics with an average fast and slow time constants of 283 fs and 1.9 ps. For voltages beyond 1V, however, the device had more complicated dynamics, possibly because of the mixed role of intra-band and inter-band transitions at 1250 nm [108]. Figure 4.3.7 (b) also shows the measured saturation curves at bias voltages of 0, 0.25, 0.5, 0.75 and 1V. Since the relaxation of graphene, 1.9ps, is slower than the excitation pulses of 100fs, we used the slow SA equation [59] in theoretical fitting to the data. According to the results obtained from the theoretical fits, which are plotted in Figure 4.3.7 (c), the saturation fluence at 1250 nm monotonically increases with the applied bias, becoming 456 μJ/cm^2 at 1V and the modulation depth decreases from 1.09% at 0V to 0.69% at 1V. Hence, we were able to adjust the modulation depth of the device in the range of 1.1-0.7%.

Moreover, we also measured the change in the optical transmission under the presence of a pump of 700nm as a function of bias voltage in Figures 4.3.8 (a) and (b). Figure 4.3.8 (a) clearly shows that by applying a bias voltage, the transitions beginning from 1450nm to 850nm become forbidden due to Pauli blocking. Similar to Figure 4.3.6 (b), in Figure 4.3.8 (b), we observed the two step-like behavior due to the asymmetric doping of two graphene electrodes.

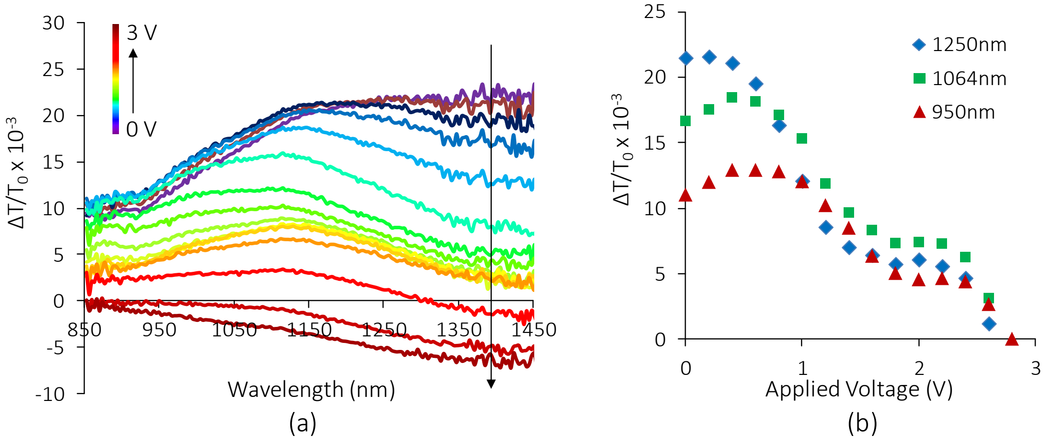

Figure 4.3.8: (a) Transmission change of VCG-SA as a function of wavelength and applied voltage. (b) Measured variation of the transmission change as a function of the bias voltage at the wavelengths of 950, 1064 and 1250 nm.

In conclusion, we have characterized the optical properties of graphene samples on quartz, YAG and CaF_2. Graphene on CaF_2 was used in mode locking of Cr:ZnSe laser (2.5μm). Graphene on quartz and YAG substrate were used in mode locking of Cr:Forsterite laser (1.25μm) in collaboration with Isinsu Baylam. Since quartz has parasitic absorptions above 2 μm and the graphene on YAG sample showed unintentional doping, we could not initiate pulsed operation in Cr:ZnSe laser. We determined the saturation fluence and modulation depth of samples as 34 μJ/cm^2 and 0.6%, 60 μJ/cm^2 and 0.8%, 39 μJ/cm^2 and 0.6% for graphene on quartz, YAG and CaF_2, respectively. We did not observe any significant dependence on the type of the substrate, the only effect of the substrate is that it has to be transparent in the operation range of the laser.

Furthermore, we have characterized the linear and non-linear optical properties of a voltage controlled saturable absorber based on graphene super capacitors. One of the most favorable characteristics of the graphene supercapacitor, in comparison with its solid-state counter parts, is the possibility of shifting the Fermi level by several eV (in our case $|2\Delta E_F|$ by as much as 2.4 eV) with relatively low bias voltages of the order of several volts. Pump-probe measurements revealed that the ultrafast response of the graphene has similar dynamics with an average fast and slow time constants of 283 fs and 1.9 ps up to 1V of applied voltage. The saturation fluence at 1250 nm monotonically increases with the applied bias, becoming 456 μJ/cm^2 at 1V and the modulation depth decreases from 1.09% at 0V to 0.69% at 1V. Hence, we were able to adjust the modulation depth of the device in the range of 1.1-0.7%. In comparison with other conventional nano-structured carbon-based saturable absorbers, the most important advantage of the current scheme is that the proposed graphene supercapacitor architecture enables the flexibility of adjusting the overall device loss with reasonably low bias voltages while still enabling mode-locked operation. We believe that this superior characteristic makes the voltage controlled graphene saturable absorber device (VCG-SA) a potentially important candidate for the mode-locking of a wide range of low-gain lasers in the visible and near-infrared. In our experiments conducted with a multi-pass cavity Cr^{4+}:forsterite laser, we could successfully generate sub-100-fs, nearly transform-limited pulses near 1255 nm [109].

Chapter 5: Other Collaborative Works

5.1 Linear and non-linear optical spectroscopy of Ag_2S quantum dots

5.1.1 Introduction

Quantum dots, a type of semiconductor nanocrystals, have unique optical properties due to the quantum confinement resulting from the nanometer size of the particles. Quantum dots exhibit wavelength tunable emission under ultraviolet excitation which makes it a promising material in many fields ranging from quantum computation to linear and nonlinear *in vivo* imaging [110-113].

As the number of atoms increases in a crystalline structure, resulting energy levels evolve into continuous bands from discrete levels due to the interactions between neighboring atoms (Figure 5.1.1).

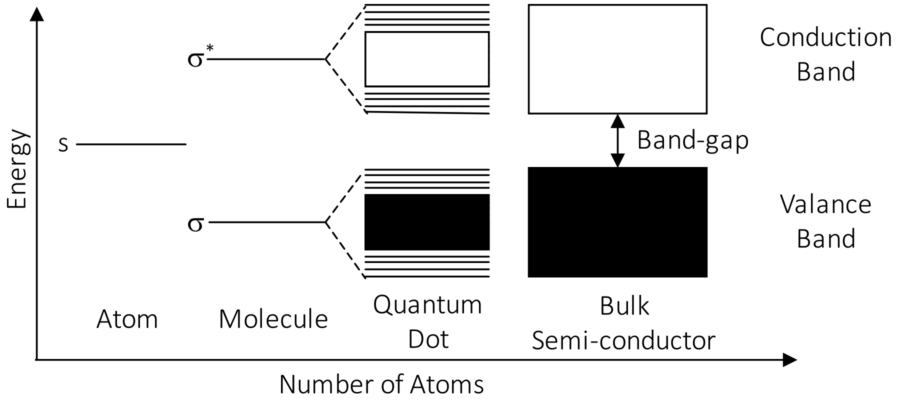

Figure 5.1.1: Energy level illustration of an atom, a molecule, a quantum dot and a bulk semiconductor material.

Due to the quantum confinement resulting from the size of the particles, it can be modeled by using the particle in a box model where the energy levels are dependent on the size of the box. As the size of the box increases, the resulting emission peak red-shifts. Combination of group II–VI semiconductor compounds, such as CdS, CdTe and CdSe, are usually used in the synthesis of colloidal quantum dots which emit in the visible region of the electromagnetic spectrum. As the size of the quantum dots is increased, the peak of the emission signal shifts to longer wavelengths (See Figure 5.1.2, the image was taken from PlasmaChem websit).

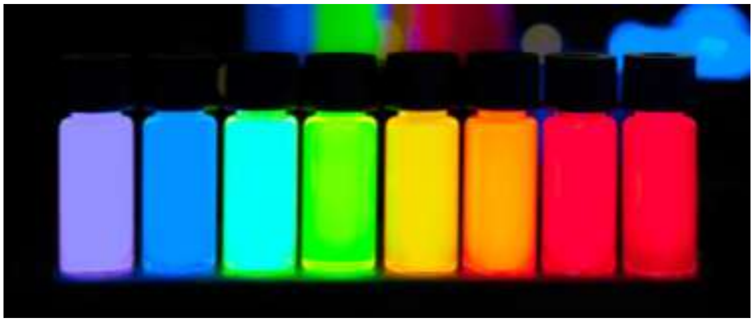

Figure 5.1.2: Band-gap tunable emission from colloidal quantum dots under ultra-violet excitation.

To date, many groups reported size-tunable photoluminescence from different types of quantum dots in the visible region [114-116]. Lately, there is a tremendous demand for near infrared (NIR) emitting quantum dots (NIR QDs), especially in biological applications and in efficient solar energy conversion [117]. This can be fulfilled with the development of quantum dots which emit at the near-infrared portion of electromagnetic spectrum [118, 119]. In literature CdSeTe [120], CdSeTe/Cd, CdHgTe/CdS [121], CdTe/CdSe/ZnSe [122] and PbS [123] based QDs exhibit near-infrared emission. Among these alternatives, Ag_2Se and Ag_2S based QDs show very low toxicity [124] which enables the *in vivo* imaging in the near infrared region.

In this section, we measured the photoluminescence and nonlinear absorption properties of Ag_2S based near-infrared emitting quantum dots. The samples were prepared in collaboration with Dr. Funda Yağcı Acar from Chemistry Department of Koç University [125].

5.1.2 Experimental Setup

Quantum dots were synthesized in water with the following reaction:

$$\mathrm{Ag_2NO_{3(aq)}} + \mathrm{Na_2S_{(aq)}} \rightarrow \mathrm{Ag_2S_{(s)}} + \mathrm{NaNO_{3(aq)}}$$

During the reaction, the capping agent, 2-mercaptopropionic acid (2-MPA), is added in order to prevent aggregation of the produced nanoparticles and provides an aqueous solution.

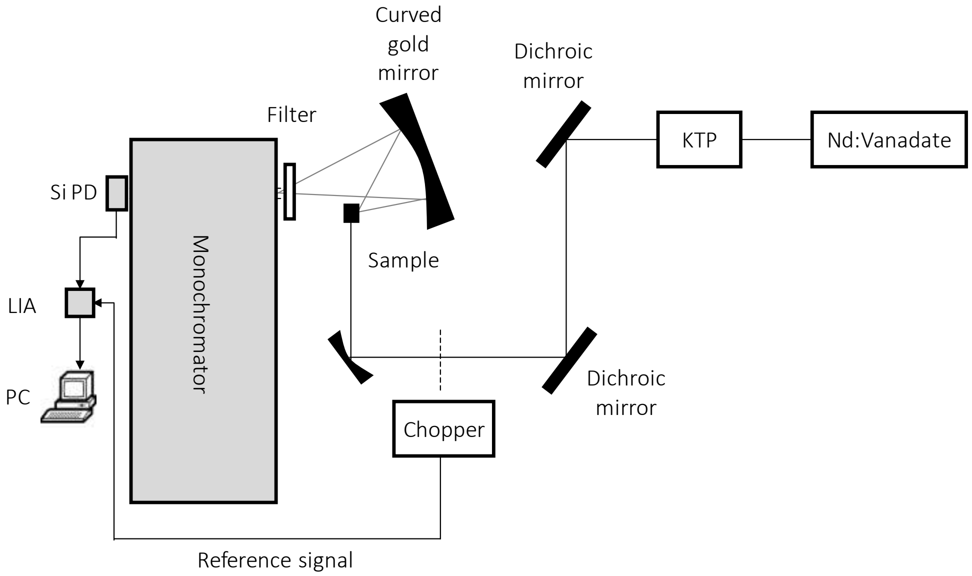

Figure 5.1.3: Photoluminescence setup, where PD, LIA, PC, and KTP stands for photodiode, lock-in amplifier, personal computer and potassium titanyl phosphate, respectively.

Experimental setup that was used in characterization of photoluminescence of the produced particles at different reaction temperatures and at different stages of the reaction is shown in Figure 5.1.3 which is a typical photoluminescence setup which includes an excitation source, a monochromator and a detection part. In our experiments we used a frequency doubled continuous wave Nd:Vanadate laser operates at 532 nm. The excitation beam was chopped at 24Hz to provide a reference signal to the lock-in amplifier. The emitted luminescence was then collected with a concave gold reflector and imaged into a 0.5 m Czerny-Turner monochromator.

An amplified silicon detector sensitive over the wavelength range of 400–1100 nm was used together with a lock-in amplifier. The excess pump light was blocked by using a long-pass filter that had a transmission of 90% from 550 to 1100 nm.

For the detection although photomultiplier tubes (PMT) are more sensitive compared to the photodetectors, we used a silicon photodetector due to the wavelength limited detection of PMT. Figure 5.1.4 shows the photoluminescence signals which were recorded with both PMT and silicon photodetector, above 850 nm the response of PMT vanishes due to the limited work function of the metal (photocathode) inside the tube.

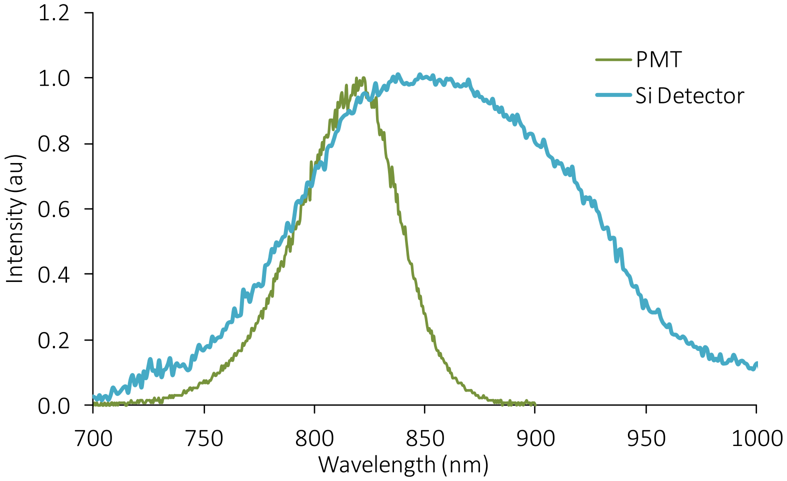

Figure 5.1.4: Comparison between the photomultiplier tube (PMT) and silicon photodetector detection.

5.1.3 Results and Discussions

In this section I will briefly summarize our photoluminescence measurements that have been done in collaboration with Ibrahim Hocaoglu, further details of this work on biomedical applications can be found in the following reference: [125].

Reaction temperature dependent absorption and emission spectrum of Ag_2S coated with 2-MPA are shown in Figure 5.1.5 where the molar ratios of Ag/S and 2-MPA/Ag is 4 and 5, respectively. These ratios were chosen as it provides the least amount of non-radiative decay and therefore high quantum yield. All three samples were collected at the 3rd hour of the reaction. Increasing the reaction temperature caused a red shift in the absorption spectra of the particles in Figure 5.1.5 which indicates that the produced particles have larger crystal sizes. Also the photoluminescence measurements plotted in Figure 5.1.5 shows that the intensity of the emission peak was improved as the reaction temperature was increased.

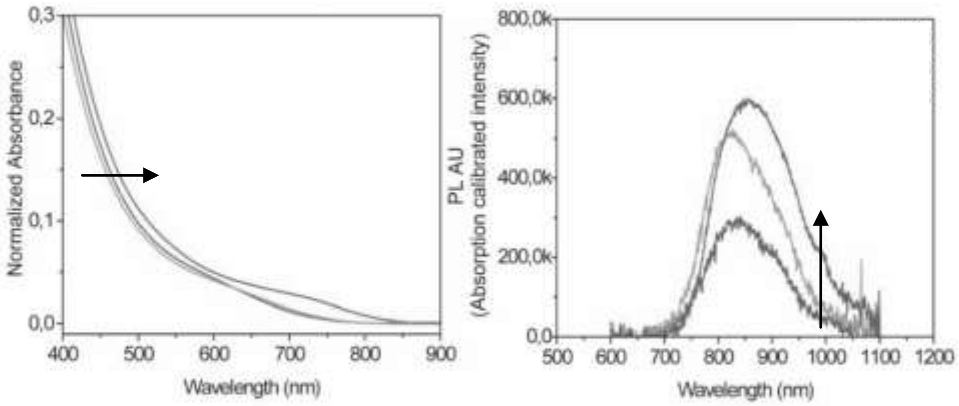

Figure 5.1.5: Prepared nanoparticles at different reaction temperatures. Arrows indicate the increasing reaction temperature which are 30, 50 and 90° C (Ag/S=4, 2MPA/Ag=5) [125].

Notice that above 50° C the peak of the emission signal red shifts which can be attributed to the decomposition of the 2-MPA at elevated temperatures. Having higher peak intensity in photoluminescence measurements suggests that the produced nanoparticles have better crystal quality, which prevents non-radiative transitions.

In the second case, samples at different reaction times are collected and absorption and photoluminescence spectra of these samples were plotted in Figure 5.1.6 in order to evaluate the optimum reaction time at 50 °C of reaction temperature. Similar to the earlier findings, longer reaction durations lead to larger crystals, hence the absorption of the particles is red shifted (See Figure 5.1.7, arrow indicates the increasing reaction time). In the case of the photoluminescence measurements, the optimum reaction time was determined as 7 hours where the photoluminescence quantum yield was calculated as 27%.

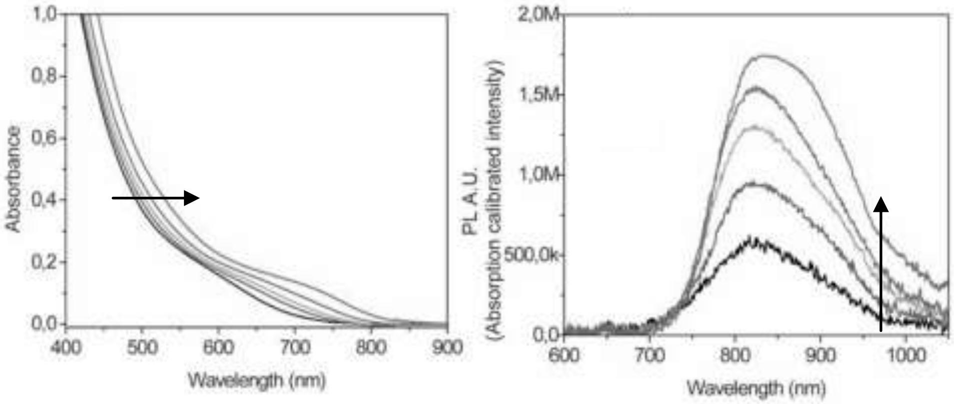

Figure 5.1.6: Photoluminescence signal of samples which are collected at different reaction times when the reaction temperature was 50°C. Arrows indicate the increasing reaction duration in the range of 1 to 22 hours (Ag/S=4, 2MPA/Ag=5) [125].

In summary, the best reaction parameters to obtain a high quality Ag_2S based quantum dot were determined as the molar ratios of Ag/2-MPA and Ag/S should be 4 and 5, respectively, and the reaction temperature and duration should be 50°C and 7 hours, respectively.

5.2 Temperature sensitive CdS/DMAEMA quantum dots

5.2.1 Introduction

Quantum dots are a type of semiconductor nano-crystals, in which a few number of atoms forms a sphere shaped structure. Colloidal quantum dots, meaning suspended in a solution, are composed of a semiconductor core and an organic coating. Use of an organic coating provides stability, biocompatibility, and depending on the type of the coating response to an external stimulus. Stimuli responsive materials are interesting materials because it changes its properties under certain conditions [126]. In this work, we have demonstrated a temperature dependent photoluminescence from poly(2-(N,N-dimethylamino)ethyl methacrylate) (PDMAEMA) coated CdS quantum dots. The samples were synthesized by Hande Özturk from Funda Yağcı Acar’s group at Chemistry department of Koç University.

5.2.2 Experimental Setup

For temperature dependent photoluminescence measurements, we used a home-made source of 355-nm coherent radiation. The output of a 1064-nm Q-switched Nd:YAG laser was first frequency doubled in a potassium titanyl phosphate ($KTiOPO_4$, KTP) crystal to convert a portion of the fundamental beam to its second harmonic at 532 nm. The beams at 1064 nm and 532 nm were then focused inside a 20-mm-long lithium triborate (LiB_3O_5, LBO) crystal to produce 355-nm radiation via sum frequency generation. Prepared quantum dot samples were placed in a temperature controlled cuvette and the temperature sensor of the controller (Newport Corp. MODEL 325) was dipped into the sample cuvette in order to collect more accurate data between 25 to 80 °C. As the temperature of the samples was varied, the emitted luminescence was collected with a concave gold mirror and focused into a 0.5-m Czerny–Turner type monochromator. The emission spectra were recorded between 400 and 750 nm with a photomultiplier tube (PMT).

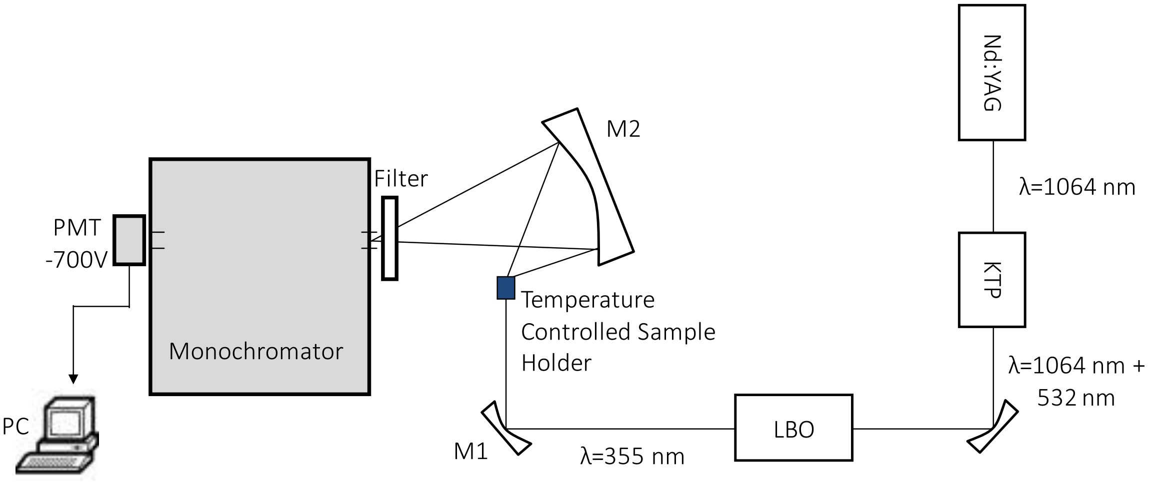

Figure 5.2.1: Experimental setup to measure the temperature dependent photoluminescence signal.

5.2.3 Results and Discussions

The samples were heated up to 65°C from room temperature. Measured photoluminescence signals at different temperatures are shown in Figure 5.2.2.

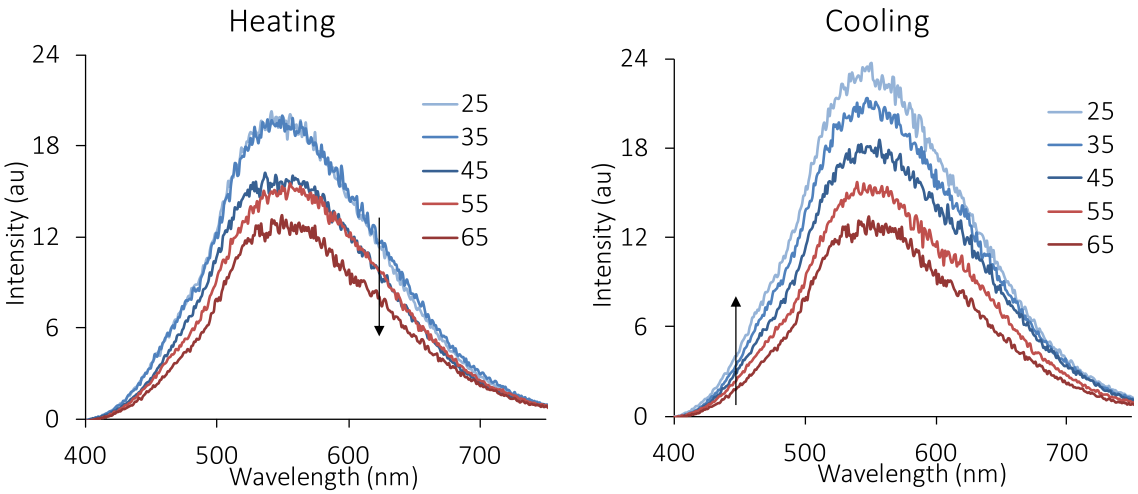

Figure 5.2.2: Measured temperature dependent photoluminescence signal from room temperature up to 65° C.

The photoluminescence intensity of the sample decreased about 52% as the temperature increased from room temperature to 65°C. In order to test the reversibility of this behavior we slowly cooled the samples back to room temperature, where the initial emission strength is fully recovered even after 3rd cycle shown in Figure 5.2.3. The hysteresis in the heating and cooling curves can be attributed to the time required for the disentanglement of collapsed polymer coating.

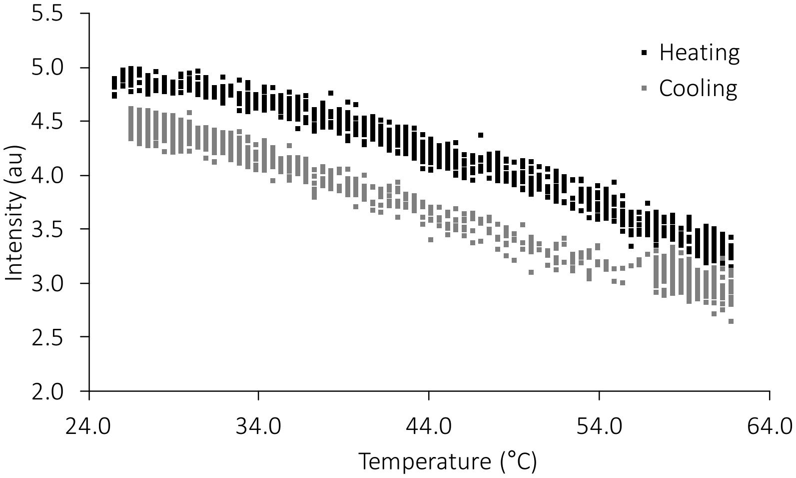

Figure 5.2.3: Third heating and cooling cycle of the sample.

Finally we have measured the stability of the emission at constant temperature for 200 mins, which corresponds to almost 3.5 hours. The measurement shown in Figure 5.2.4 proves that the produced particles are stable under continuous excitation at 355nm. In summary, all the measurements indicate that the produced temperature sensitive CdS based quantum dots exhibit excellent response to temperature in a reversible manner.

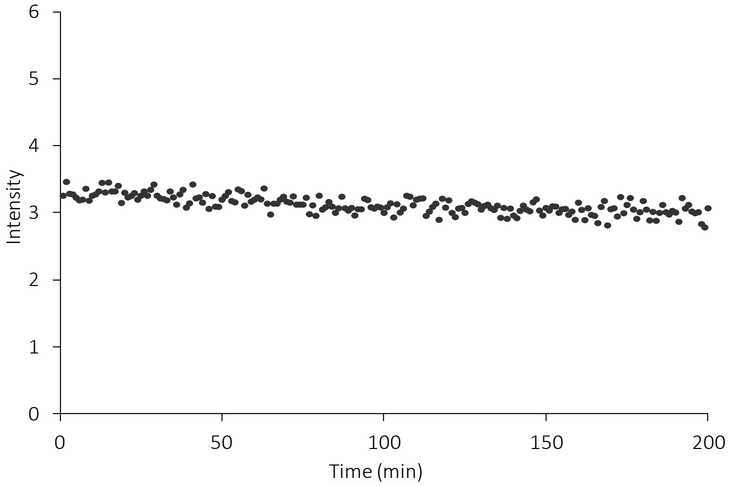

Figure 5.2.4: Peak intensity of photoluminescence signal at constant temperature as a function of time.

5.3 Injection seeding of Cr:ZnSe laser

5.3.1 Introduction

Cr:ZnSe lasers with broad tunability in the 2–3 μm find a multitude of applications in the pumping of parametric oscillators in the mid-IR [127], in the generation of frequency combs for vibrational spectroscopy of molecules [5], and in remote sensing [128]. All of these applications require a coherent light source that has a defined spectral output and that is tunable. Because the high stimulated emission cross section, four-level energy structure, and absence of excited-state absorption in Cr:ZnSe, it is quite straightforward to obtain efficient lasing with a low threshold pump power [31, 60, 61, 129, 130]. However, especially during gain-switched operation where the gain far exceeds the losses, this also leads to simultaneous lasing over a very broad spectral bandwidth (of the order tens of nanometers, often exceeding 100 nm) and limits the effective use of the laser in the applications mentioned above. An alternative approach employs injection seeding, whereby the spectral characteristics of the gain-switched laser are controlled by the seed laser having a narrower spectrum. Since the seed laser is coupled into the oscillator via an end mirror, no intracavity wavelength-selective elements are needed and no additional losses are introduced.

5.3.2 Experimental Setup

Figure 5.3.1 shows the experimental setup of the injection seeded, gain-switched Cr:ZnSe laser. As the seed laser, we used a continuous wave (cw) tunable Cr:ZnSe laser pumped by a Tm:fiber laser. The resonator of the cw seed laser consisted of two curved mirrors, each with a radius of curvature of 10 cm (M1 and M2), a flat high reflector (M3), and a flat 3% transmitting output coupler (OC1).

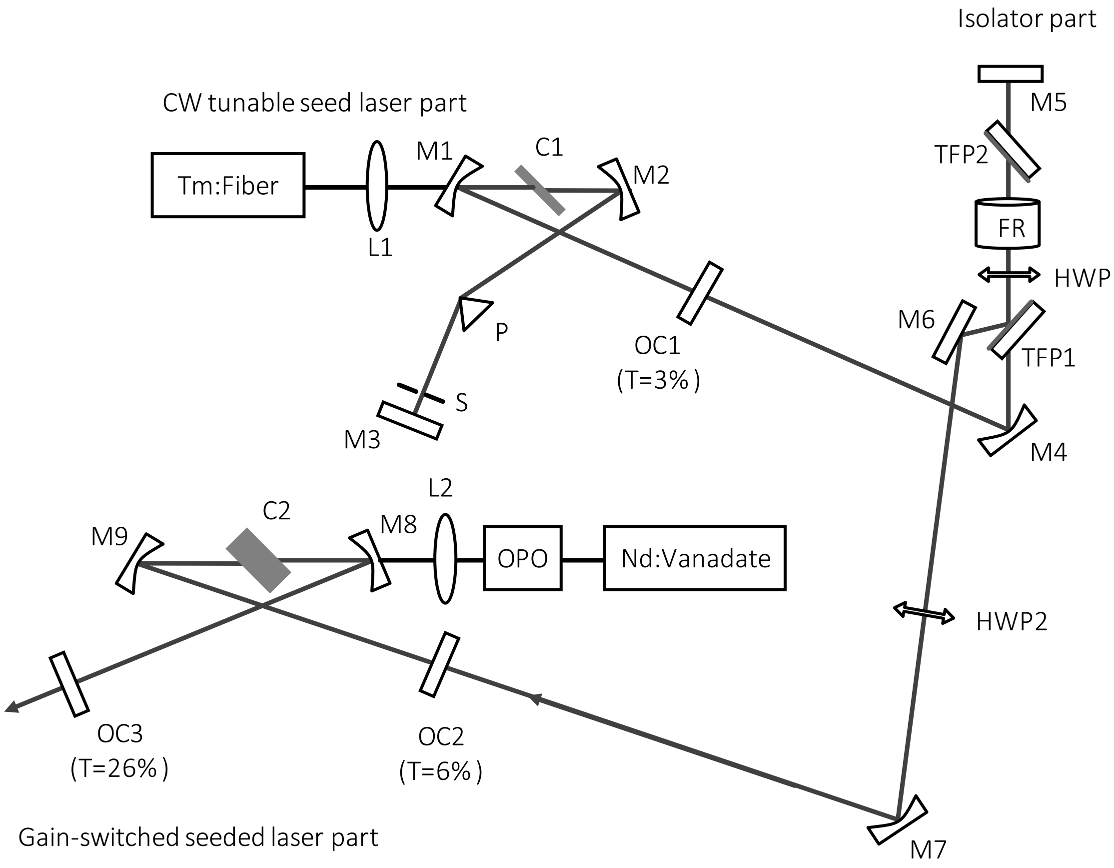

Figure 5.3.1: Schematic of the injection-seeded, gain-switched Cr:ZnSe laser.

A 2.5 mm long Cr:ZnSe crystal (C1) was positioned between M1 and M2 at Brewster incidence. The crystal had a small-signal absorption of 94% at pump wavelength of 1800 nm. The crystal was surrounded with indium foil and clamped between two copper holders which was kept at 21 °C by water cooling. The pump beam was focused to an estimated beam waist of 23μm inside the crystal with a convex lens (L1, f=7.5cm). A Brewster-cut CaF2 prism (P) was placed in the high reflector arm of the resonator to tune the output. An adjustable slit (S) was positioned between the prism and the end high reflector to reduce the spectral width of the seed laser. The high reflector and output coupler arm lengths were 65.5 and 83 cm, giving an estimated laser waist of 35 μm near the center of the stability region. The total cavity length of the seed laser was 160 cm, corresponding to a free spectral range of 93.8 MHz. The output of the cw seed laser was collimated with a curved mirror (M4, R=2m) and passed through a Faraday isolator to protect the CW Cr:ZnSe laser from back reflection as well as from pulses originating from the gain-switched laser. The Faraday isolator part includes two thin-film polarizers (TFP1 and TFP2), a half-wave plate (HWP1), a Faraday rotator (FR), and a flat aluminum retro reflecting mirror (M5).

The output of the isolator was then directed with a flat aluminum mirror (M6) to the gain-switched oscillator. The x-type resonator of the gain-switched laser consisted of two curved mirrors (M8 and M9, R=20cm) and two flat output couplers having transmission values of 6% and 26% (OC2 and OC3 in Figure 5.3.1, respectively). The output coupler OC2 was used to couple the cw seed beam into the gain-switched resonator while the injection-seeded output was taken from OC3. Inside the gain-switched resonator, a 6.6 mm long polycrystalline Cr:ZnSe (C2) sample was used at Brewster incidence. The crystal had a small-signal absorption of 92% at a pump wavelength of 1570 nm. The gain-switched Cr:ZnSe oscillator was pumped by a 1570 nm optical parametric oscillator (OPO), which, in turn, was pumped by a 1kHz-Q-switched Nd:YAG laser at1064 nm. The OPO pump beam was focused inside the crystal with an input lens (L2) which has a focal length of 20 cm. During the experiments, the spectrum of the gain-switched pulses was measured with a 0.5 m Czerny–Turner-type monochromator that had a resolution of 0.05 nm.

5.3.3 Results and Discussions

Figure 5.3.2 shows the spectra of the unseeded and seeded gain-switched Cr:ZnSe laser for three different seed wavelengths. In the absence of the cw seed laser, the gain-switched oscillator had an output spectral width (FWHM) of 125 nm centered around 2360 nm. When the cw laser beam with a bandwith (FWHM) of 0.3 nm was injected into the gain-switched laser cavity, the spectral width of the gain-switched laser was narrowed down to about 0.3 nm. In other words, the spectral brightness of the laser was improved by a factor of 417. When the gain-switched laser was pumped with 600μJ of input pulse energy, the seeded laser was producing output pulse energies in the range of 100-130μJs, depending on the operation wavelength of the seed laser. Below 1 mW of seed power, the residual spectrum of gain-switched laser was reappeared in the output spectrum (See Figure 5.3.2).

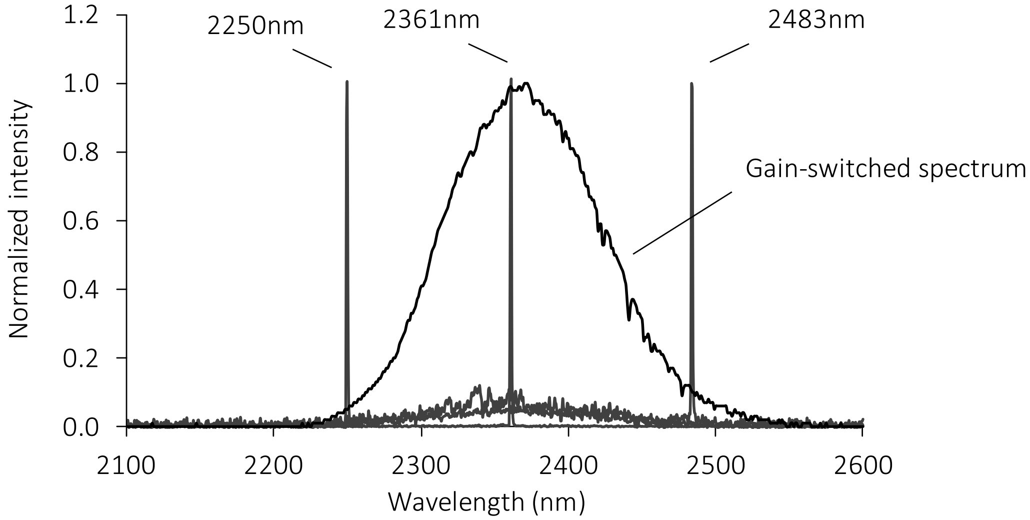

Figure 5.3.2: Spectra of the unseeded and injection-seeded gain-switched Cr:ZnSe laser.

The wavelength of the injection-seeded laser could be successfully tuned in the range of 2250–2483 nm by tuning the operation wavelength of cw seed laser. Figure 5.3.3 (a) further shows the tuning curve of the injection-seeded Cr:ZnSe laser between 2255 and 2455 nm when the input pump pulse energy was 600μJ. In this spectral range, the residual unseeded gain-switched laser spectrum was not present. The highest pulse energy was obtained at 2360 nm, which was also the wavelength of peak emission from the unseeded gain-switched Cr:ZnSe laser.

Figure 5.3.3 (b) shows the efficiency curves of the unseeded and injection-seeded Cr:ZnSe laser. The output pulse energy was measured after the 26% output coupler (OC3). The slope efficiency of the unseeded gain-switched laser was determined to be 22.5% with respect to the incident pump pulse energy. Above 480μJ of incident pump energy, saturation was observed in the output energy of the unseeded oscillator. This is due to the depletion of the ground-state population, resulting in a reduction of the pump absorption.

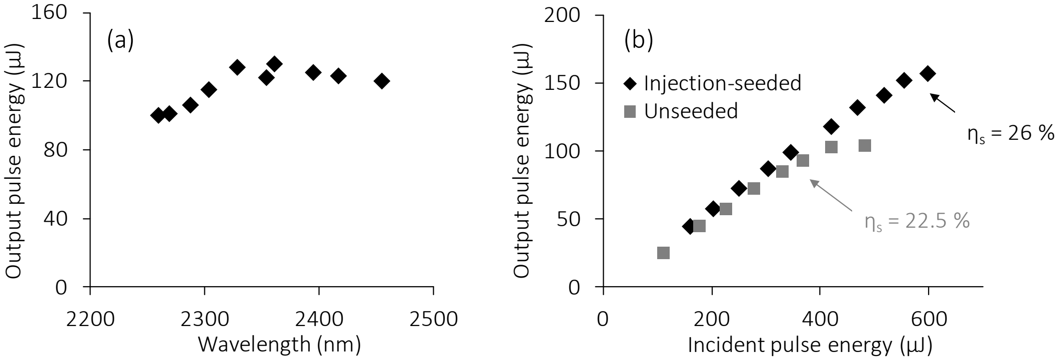

Figure 5.3.3: (a) Tuning curve of the injection-seeded, gain-switched Cr:ZnSe laser. (b) Efficiency curve of the injection-seeded and unseeded Cr:ZnSe laser as a function of the incident pump pulse energy.

However, in the case of the injection seeded laser, saturation of pump was observed at higher incident pump energies (around 600µJ). This can be best explained by the fact that due to injection seeding, gain-switched laser pulses evolve from the seed laser light rather than noise. As a result, a higher rate of stimulated emission, initiated by the evolving laser pulse, replenishes the ground-state population more effectively and reduces the saturation of pump absorption.

5.4 Chirped-pulsed amplification of Cr:ZnSe pulses

5.4.1 Introduction

Chirped pulse amplification (CPA) is a widely used technique to increase the pulse energy as well as the peak power of typical femtosecond laser sources [131]. It has been applied to well known tunable solid state lasers, such as the Nd:Glass [131], Alexandrite [132], Cr:LiSAF [133, 134] Ti:Sapphire [135, 136], Cr:forsterite [137-140], where the nano joule pulses produced from femtosecond sources amplified up to millijoules of pulse energies. A typical CPA has four main stages which are depicted in Figure 5.4.1.

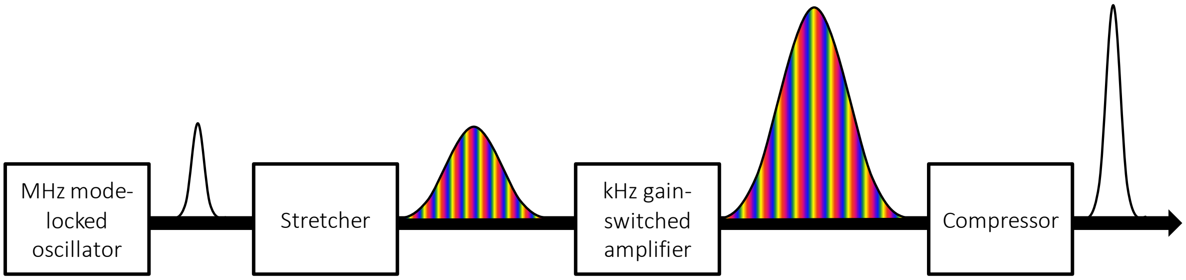

Figure 5.4.1: Evolution of generated pulses through four stages of a chirped pulsed amplifier.

The seed laser is a MHz repetition rate femtosecond laser which provides the nano joule seed pulses. In order to prevent any damage during amplification, and overlap better with the nano second pulses circulating inside the amplifier, femtosecond pulses are stretched to picoseconds by travelling through a dispersive delay line such as a pair of grating. After amplification stage, by applying oppositely signed delay to the pulses, the amplified picosecond pulses are compressed to the initial state. Compressed pulses usually have millijoules of pulse energy together with femtosecond pulse durations which provides gigawatts of peak power. Such high peak power values cannot be produced from a single laser cavity due to the possibility of damaging gain crystal and cavity components as well.

Cr:ZnSe laser is a suitable candidate to construct a chirped pulsed amplifier to extend the operation wavelength of CPAs to mid-infrared region of the spectrum. It has a broad operation bandwidth [34] which enables femtosecond pulsed operation [36-39, 72, 74].

5.4.2 Experimental Setup

In order to produce the nano joule, femtosecond seed pulses we used a Kerr-lens mode-locked Cr:ZnSe laser, which was described in Section 3.3, in detail. As shown in Figure 5.4.2, continuous-wave (cw) thulium fiber laser operates at 1.8 μm was focused inside the Cr:ZnSe crystal by using the input lens (L) which has a focal length of 7.5 cm. 2.4mm long crystal was positioned between two curved dichroic mirrors, M1 and M2 (R=10cm), at Brewster angle to minimize the reflection losses. The laser cavity is a typical astigmatically compensated four mirror x-cavity which has a 3% output coupler.

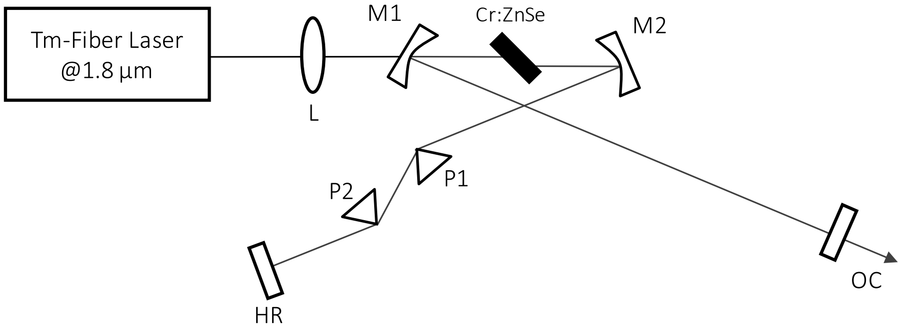

Figure 5.4.2: Schematic illustration of the femtosecond Cr:ZnSe laser as the seed laser.

High reflector (HR) and output coupler (OC) arm lengths were 62 cm and 85 cm respectively, giving a repetition rate of 95 MHz. To evaluate the power performance of the laser, the slope efficiency curve was measured as plotted in Figure 5.4.3. It produces 300mW of cw output power at an input power of 2.5W, and has a slope efficiency of 15%. In order to balance the nonlinearities inside the cavity and obtain soliton mode locking, a prism pair made of CaF_2 is added to the HR arm of the cavity (P1 and P2 in Figure 5.4.2). Overall group delay dispersion (GDD) of the cavity was calculated as -1770 fs^2.

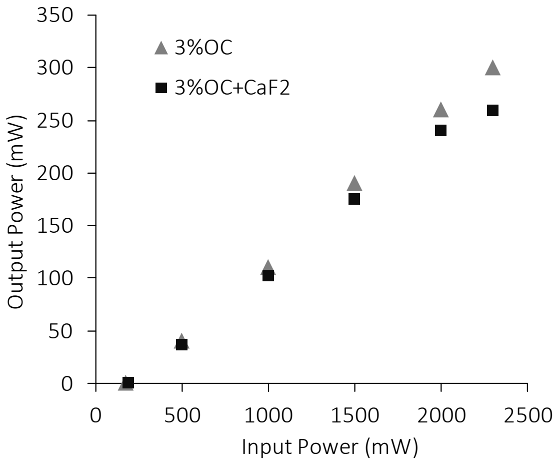

Figure 5.4.3: Continuous wave efficiency curve of the Cr:ZnSe laser.

By translating the OC, femtosecond pulses are readily obtained. Typical output spectrum and autocorrelation trace of the pulses are plotted in Figure 5.4.4 (a) and (b), respectively. Pulses as short as 83 fs were produced with an average output power of 130mW that corresponds to a pulse energy of 1.3 nJs. The time bandwidth product is calculated as 0.35 by assuming a sech^2 shaped pulses, which is in a good agreement with the theoretical value of 0.315.

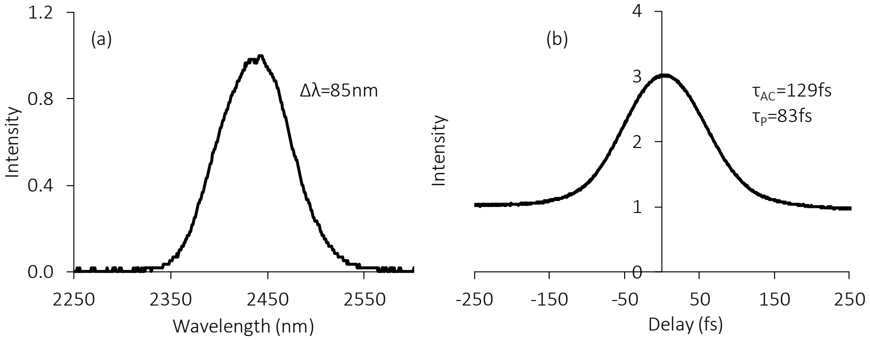

Figure 5.4.4: (a) Output spectrum and (b) auto correlation trace of the generated pulses from the femtosecond seed laser.

Femtosecond pulse spectrum and autocorrelation measurements were done by using a homemade scanning spectrometer, and a homemade autocorrelator. Produced femtosecond pulses are stretched in time domain by using a grating based stretcher and then aligned into the regenerative amplifier by using the apertures shown in Figure 5.4.5. Vertically polarized picosecond seed pulses reflected from the TFP started to circulate inside the amplifier.

We used an optical parametric oscillator (OPO) pumped gain-switched Cr:ZnSe laser which operates at 1 kHz as the amplifier.

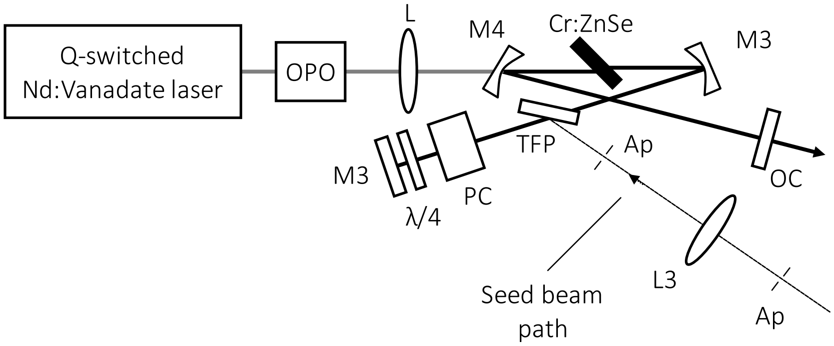

Figure 5.4.5: Schematic illustration of the gain-switched Cr:ZnSe laser as the regenerative amplifier.

Output of the OPO, which operates at 1.56um wavelength, was focused into the Cr:ZnSe crystal with an input lens of L (f=12.5cm) as seen in Figure 5.4.5. 6.6 mm-long crystal was placed between two curved dichroic mirrors, M3 and M4, (R=20cm) at Brewster angle. Measured efficiency curve of the laser with a 26% output coupler is shown in Figure 5.4.6. The laser was producing 1 kHz pulses with a maximum average output power of 149mW when the input pump power was 560mW. The slope efficiency of the gain-switched laser was determined to be 28%.

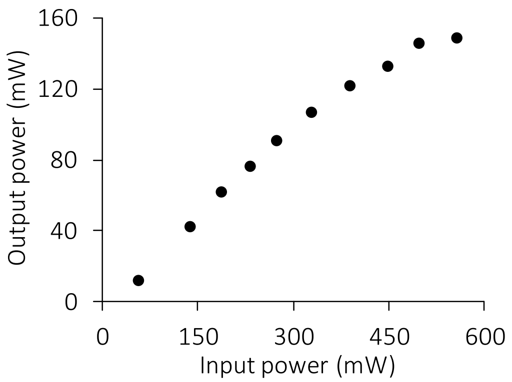

Figure 5.4.6: Efficiency curve of the empty gain-switched Cr:ZnSe laser with 26% output coupler.

The most crucial part of the amplifier setup is the correct operation of the Pockels cell. Pockels cell is an optoelectronic device which basically rotates the polarization of the light by applying a high voltage to a nonlinear crystal, in our case lithium niobate ($LiNbO_3$). When it is used together with a quarter wave plate and a thin film polarizer (TFP) as shown in the Figure 5.4.5, depending on the on/off state of the Pockels cell, pulses circulating inside the cavity are trapped or cavity dumped, respectively. By using a delay generator, on and off time durations are easily adjusted with respect to the trigger coming from the pump source (Figure 5.4.7).

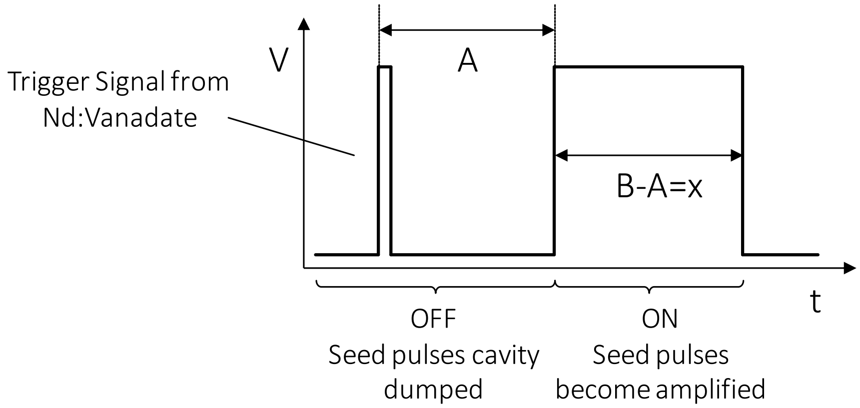

Figure 5.4.7: Graphical illustration of Pockels cell timings.

Amplified output power was optimized both with the alignment of the amplifier mirrors and the delay timings of the delay generator.

5.4.3 Results and Discussions

While the stretched seed pulses circulate inside the amplifier, by using the correct timings of the Pockels cell, they become amplified. Time required to extract maximum gain from the gain-switched laser was around 200-300ns, which corresponds to 20-30 roundtrips. Figure 5.4.8 (a) shows the amplified output power of the pulses with respect to the input power of gain-switched laser. The laser was producing maximum 45 mWs of average output power, which corresponds to 45 uJ of pulse energy with picoseconds pulse duration. Figure 5.4.8 (b) shows the spectrum of the amplified pulses, which has a spectral FWHM of only 14 nm where the seed pulses were having 80nm bandwidth. Such spectral narrowing can be due to spectral narrowing inside the amplifier, or the atmospheric absorption which exists at the operation range, or narrow line reflectivity of the thin film polarizers (TFPs).

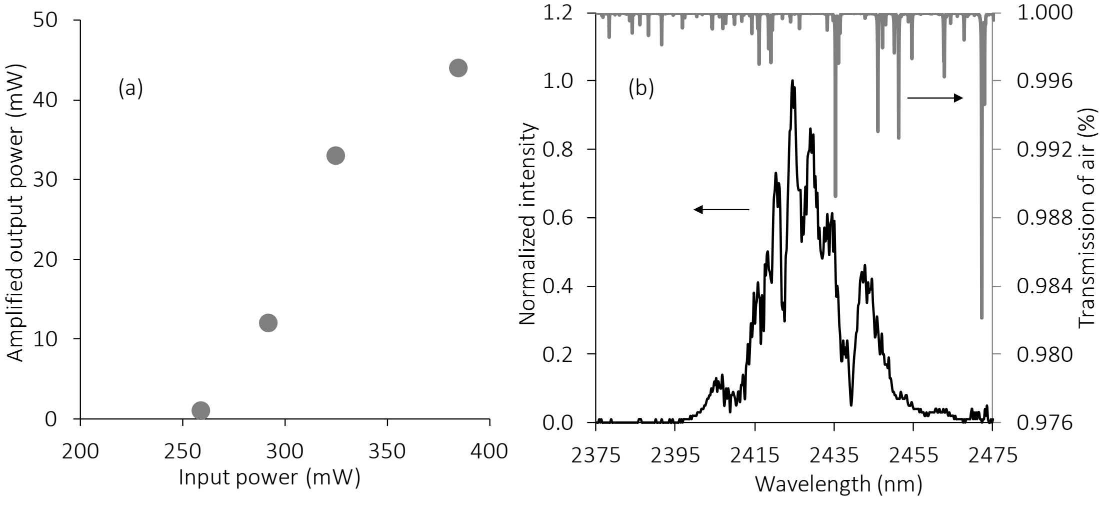

Figure 5.4.8: (a) Amplified output power as a function of the input power provided from the OPO setup. (b) Amplified spectrum of the pulses together with the spectrum of atmosphere.

Chapter 6: Conclusions

In this thesis work, we focused on the development of an efficient and robust femtosecond pulse producing mid infrared laser by utilizing different mode locking techniques. In particular, we successfully applied Kerr lens mode locking and graphene saturable absorber mode locking techniques to the Cr:ZnSe laser which operates around 2.45 μm. In the second part of the thesis, we discussed linear and non-linear optical characterization of a gated graphene based supercapacitor.

First, we demonstrated the Kerr lens mode locking of Cr:ZnSe laser and evaluated the performance of four different cost-effective and practical dispersion compensation methods. Our results show that, in the case of BK7, although the material dispersion has the correct sign to compensate for Kerr nonlinearities, the excessive material absorption leads to poor power and mode-locked performance. The highest pulse energy was obtained with a 6% output coupler and a CaF_2 prism pair, where as high as 1.81 nJ was obtained with 2 W of pump power. When a 1% output coupler was used with the CaF_2 prism pair, higher intracavity energy led to the generation of the shortest pulses (duration of 92 fs FWHM) in the experiments. Overall, YAG slabs could be used with lower insertion loss in comparison with prism pairs. On the other hand, the prism pair allowed for continuous adjustment of the cavity dispersion. Finally, by using the soliton area theorem, we estimated the nonlinear refractive index (n_2) of ZnSe as $(1.2\pm0.2)\times10^{-18}$ m^2/W, which comes close to the previously reported value of 1.7×10^{-18} m^2/W.

Later, we demonstrated the graphene saturable absorber mode-locked operation of a stable femtosecond Cr:ZnSe laser. The laser produced 176-fs pulses at a repetition rate of 78 MHz with an average power of 80 mW. The measured time-bandwidth product was 0.39 with 3% OC. With a 6% OC, 2.4-nJ, 200-fs pulses were generated near 2400 nm at a pulse repetition frequency of 78 MHz. The average mode-locked output power was 185 mW. To the best of our knowledge, this represents the first demonstration of a femtosecond Cr:ZnSe laser, passively mode locked with a graphene saturable absorber. We have characterized the optical properties of graphene samples on quartz, YAG and CaF_2. Graphene on CaF_2 was used in the mode locking of Cr:ZnSe laser (2.5μm). Graphene on quartz and YAG substrate were used in the mode locking of Cr:Forsterite laser (1.25μm) in collaboration with Isinsu Baylam. Since quartz has parasitic absorption above 2 μm and the graphene on YAG sample showed possible unintentional doping, we could not initiate pulsed operation in Cr:ZnSe laser. We determined the saturation fluence and modulation depth of samples as 34 $\mu J/cm^2$ and 0.6%, 60 $\mu J/cm^2$ and 0.8%, 39 $\mu J/cm^2$ and 0.6% for graphene on quartz, YAG and CaF_2, respectively. We did not observe any significant dependence on the type of the substrate, the only effect of the substrate is that it has to be transparent in the operation range of the laser.

Finally, we have characterized the linear and non-linear optical properties of a voltage controlled saturable absorber based on graphene super capacitor. One of the most favorable characteristics of the graphene supercapacitor is the possibility of shifting the Fermi level by several eV (in our case $|2\Delta E_F|$ by as much as 2.4 eV) with relatively low bias voltages of the order of several volts. Pump-probe measurements revealed that the ultrafast response of the device has similar dynamics with an average fast and slow time constants of 283 fs and 1.9 ps up to 1V of applied voltage. The saturation fluence at 1250 nm monotonically increases with the applied bias, becoming 456 μJ/cm^2 at 1V and the modulation depth decreases from 1.09% at 0V to 0.69% at 1V. Hence, we were able to adjust the modulation depth of the device in the range of 1.1-0.7%. In comparison with other conventional nano-structured carbon-based saturable absorbers, the most important advantage of the current scheme is that the proposed graphene supercapacitor architecture enables the flexibility of adjusting the overall device loss with reasonably low bias voltages while still enabling mode-locked operation. We believe that this superior characteristic makes the voltage controlled graphene saturable absorber device (VCG-SA) a potentially important candidate for the mode-locking of a wide range of low-gain lasers in the visible and near-infrared. In our experiments conducted with a multi-pass cavity Cr^{4+}:forsterite laser, we could successfully generate sub-100-fs, nearly transform-limited pulses near 1255 nm.

BIBLIOGRAPHY

1. T. Udem, J. Reichert, R. Holzwarth, and T. W. Hänsch, "Absolute Optical Frequency Measurement of the Cesium D1 Line with a Mode-Locked Laser," Physical Review Letters **82**, 3568 (1999).
2. J. Mandon, E. Sorokin, I. T. Sorokina, G. Guelachvili, and N. Picque, "Supercontinua for high-resolution absorption multiplex infrared spectroscopy," Optics Letters **33**, 285 (2008).
3. E. Sorokin, I. T. Sorokina, J. Mandon, G. Guelachvili, and N. Picque, "Sensitive multiplex spectroscopy in the molecular fingerprint 2.4 um region with a Cr^{2+}: ZnSe femtosecond laser," Optics Express **15**, 16540 (2007).
4. M. J. Thorpe and J. Ye, "Cavity-enhanced direct frequency comb spectroscopy," Applied Physics B: Lasers and Optics **91**, 397 (2008).
5. B. Bernhardt, E. Sorokin, P. Jacquet, R. Thon, T. Becker, I. T. Sorokina, N. Picque, and T. W. Hansch, "Mid-infrared dual-comb spectroscopy with 2.4 μm Cr^{2+}:ZnSe femtosecond lasers," Applied Physics B: Lasers and Optics **100**, 3 (2010).
6. I. T. McKinnie, G. J. Wagner, and C. B. Rawle, "Dual-band Mid-Wave/Long-wave ZGP OPO Pump-tuned by a Cr:ZnSe Laser," in *Conference on Lasers and Electro-Optics*, (Optical Society of America, 2002), paper CTuH1.
7. N. Leindecker, A. Marandi, R. L. Byer, K. L. Vodopyanov, J. Jiang, I. Hartl, M. Fermann, and P. G. Schunemann, "Octave-spanning ultrafast OPO with 2.6-6.1 μm instantaneous bandwidth pumped by femtosecond Tm-fiber laser," Optics Express **20**, 7046 (2012).

8. W. S. Pelouch, G. J. Wagner, and T. J. Carrig, "Mid-Wave ZGP OPOs Pumped by a Cr:ZnSe Laser," in *Advanced Solid-State Photonics*, (Optical Society of America, 2001), paper PD1.
9. K. Vodopyanov, E. Sorokin, P. Schunemann, and I. Sorokina, "4.4-5.4 µm frequency comb from a subharmonic OP-GaAs OPO pumped by a femtosecond Cr:ZnSe laser," in *Advanced Solid-State Photonics*, (Optical Society of America, 2011), paper AME2.
10. L. Nick, M. Alireza, L. B. Robert, and L. V. Konstantin, "Broadband degenerate OPO for mid-infrared frequency comb generation," Optics Express **19**, 6296 (2011).
11. H. Xiong, H. Xu, Y. Fu, J. Yao, B. Zeng, W. Chu, Y. Cheng, Z. Xu, E. J. Takahashi, K. Midorikawa, X. Liu, and J. Chen, "Generation of a coherent x ray in the water window region at 1 kHz repetition rate using a mid-infrared pump source," Optics Letters **34**, 1747 (2009).
12. A. Gordon and F. X. Kartner, "Scaling of keV HHG photon yield with drive wavelength," Optics Express **13**, 2941 (2005).
13. A. Cingoz, D. C. Yost, T. K. Allison, A. Ruehl, M. E. Fermann, I. Hartl, and J. Ye, "Direct frequency comb spectroscopy in the extreme ultraviolet," Nature **482**, 68 (2012).
14. T. Popmintchev, M.-C. Chen, D. Popmintchev, P. Arpin, S. Brown, S. Ališauskas, G. Andriukaitis, T. Balčiunas, O. D. Mücke, A. Pugzlys, A. Baltuška, B. Shim, S. E. Schrauth, A. Gaeta, C. Hernández-García, L. Plaja, A. Becker, A. Jaron-Becker, M. M. Murnane, and H. C. Kapteyn, "Bright Coherent Ultrahigh Harmonics in the keV X-ray Regime from Mid-Infrared Femtosecond Lasers," Science **336**, 1287 (2012).
15. F. K. Tittel, D. Richter, and A. Fried, "Mid-Infrared Laser Applications in Spectroscopy," in *Solid-State Mid-Infrared Laser Sources*. vol. 89, I. T. Sorokina and K. L. Vodopyanov, Eds., ed Berlin Heidelberg: Springer, 2003, pp. 445.
16. V. Ebert, H. Teichert, P. Strauch, T. Kolb, H. Seifert, and J. Wolfrum, "Sensitive in situ detection of CO and O2 in a rotary kiln-based hazardous waste incinerator using 760nm and new 2.3µm diode lasers," Proceedings of the Combustion Institute **30**, 1611 (2005).
17. S. Kim, D. Lee, X. Liu, C. Van Neste, S. Jeon, and T. Thundat, "Molecular recognition using receptor-free nanomechanical infrared spectroscopy based on a quantum cascade laser," Scientific Reports **3**, 1 (2013).
18. M. W. Todd, R. A. Provencal, T. G. Owano, B. A. Paldus, A. Kachanov, K. L. Vodopyanov, M. Hunter, S. L. Coy, J. I. Steinfeld, and J. T. Arnold, "Application of mid-infrared cavity-ringdown spectroscopy to trace explosives vapor detection

using a broadly tunable (6–8 µm) optical parametric oscillator," Applied Physics B: Lasers and Optics **75**, 367 (2002).

19. F. Adler, K. C. Cossel, M. J. Thorpe, I. Hartl, M. E. Fermann, and J. Ye, "Phase-stabilized, 1.5 W frequency comb at 2.8-4.8 µm," Optics Letters **34**, 1330 (2009).
20. A. Schliesser, N. Picque, and T. W. Hansch, "Mid-infrared frequency combs," Nature photonics **6**, 440 (2012).
21. A. Ruehl, A. Gambetta, I. Hartl, M. E. Fermann, K. S. E. Eikema, and M. Marangoni, "Widely-tunable mid-infrared frequency comb source based on difference frequency generation," Optics Letters **37**, 2232 (2012).
22. P. Del'Haye, A. Schliesser, O. Arcizet, T. Wilken, R. Holzwarth, and T. J. Kippenberg, "Optical frequency comb generation from a monolithic microresonator," Nature **450**, 1214 (2007).
23. M. J. Thorpe and J. Ye, "Cavity-enhanced direct frequency comb spectroscopy," Applied Physics B: Lasers and Optics **91**, 397 (2008).
24. C. Gohle, T. Udem, M. Herrmann, J. Rauschenberger, R. Holzwarth, H. A. Schuessler, F. Krausz, and T. W. Hänsch, "A frequency comb in the extreme ultraviolet," Nature **436**, 234 (2005).
25. R. Axel, G. Alessio, H. Ingmar, E. F. Martin, S. E. E. Kjeld, and M. Marco, "Widely-tunable mid-infrared frequency comb source based on difference frequency generation," Optics Letters **37**, 2232 (2012).
26. S. D. Jackson, "Towards high-power mid-infrared emission from a fibre laser," Nature photonics **6**, 423 (2012).
27. P. P. Sorokin and M. J. Stevenson, "Stimulated Infrared Emission from Trivalent Uranium," Physical Review Letters **5**, 557 (1960).
28. P. F. Moulton and A. Mooradian, "Broadly tunable cw operation of Ni: MgF2 and Co: MgF2 lasers," Applied Physics Letters **35**, 838 (1979).
29. P. F. Moulton, A. Mooradian, and T. B. Reed, "Efficient cw optically pumped Ni:MgF2 laser," Optics Letters **3**, 164 (1978).
30. L. D. DeLoach, R. H. Page, G. D. Wilke, S. A. Payne, and W. F. Krupke, "Transition metal-doped zinc chalcogenides: spectroscopy and laser demonstration of a new class of gain media," IEEE Journal of Quantum Electronics **32**, 885 (1996).
31. R. H. Page, K. I. Schaffers, L. D. DeLoach, G. D. Wilke, F. D. Patel, J. B. TassanoJr., S. A. Payne, W. F. Krupke, K.-T. Chen, and A. Burger, "Cr^{2+} Doped Zinc Chalcogenides as Efficient, Widely Tunable Mid-Infrared Lasers," IEEE Journal of Quantum Electronics **33**, 609 (1997).
32. I. T. Sorokina, "Crystalline Mid-Infrared Lasers," in *Solid-State Mid-Infrared Laser Sources*. vol. 89, I. T. Sorokina and K. L. Vodopyanov, Eds., ed Berlin, Heidelberg: Springer, 2003, pp. 255.

33. A. V. Podlipensky, V. G. Shcherbitsky, N. V. Kuleshov, V. I. Levchenko, V. N. Yakimovich, M. Mond, E. Heumann, G. Huber, H. Kretschmann, and S. Kuck, "Efficient laser operation and continuous-wave diode pumping of Cr2+ :ZnSe single crystals," Applied Physics B: Lasers & Optics **72**, 253 (2001).
34. E. Sorokin, I. T. Sorokina, M. S. Mirov, V. V. Fedorov, I. S. Moskalev, and S. B. Mirov, "Ultrabroad Continuous-wave tuning of ceramic Cr:ZnSe and Cr:ZnS lasers," in *Advanced Solid-State Photonics*, (Optical Society of America, 2010), paper AMC2.
35. T. J. Carrig, G. J. Wagner, A. Sennaroglu, J. Y. Jeong, and C. R. Pollock, "Mode-locked Cr2+:ZnSe laser," Optics Letters **25**, 168 (2000).
36. I. T. Sorokina, E. Sorokin, and T. Carrig, "Femtosecond Pulse Generation from a SESAM Mode-Locked Cr:ZnSe Laser," in *Conference on Lasers and Electro-Optics*, (OSA, 2006), paper CMQ2.
37. M. N. Cizmeciyan, H. Cankaya, A. Kurt, and A. Sennaroglu, "Kerr-lens mode-locked femtosecond Cr^{2+}:ZnSe laser at 2420 nm," Optics Letters **34**, 3056 (2009).
38. E. Sorokin and I. T. Sorokina, "Ultrashort-pulsed Kerr-lens modelocked Cr:ZnSe laser," in *CLEO Europe*, (Optical Society of America, 2009), paper CF1.3 Wed.
39. M. N. Cizmeciyan, J. W. Kim, S. Bae, B. H. Hong, F. Rotermund, and A. Sennaroglu, "Graphene mode-locked femtosecond Cr:ZnSe laser at 2500nm," Optics Letters **38**, 341 (2013).
40. I. T. Sorokina, E. Sorokin, S. Mirov, V. Fedorov, V. Badikov, V. Panyutin, A. D. Lieto, and M. Tonelli, "Continuous-wave tunable Cr^{2+} :ZnS laser," Applied Physics B **74**, 607 (2002).
41. N. Tolstik, E. Sorokin, and I. T. Sorokina, "Kerr-lens mode-locked Cr:ZnS laser," Optics Letters **38**, 299 (2013).
42. E. Sorokin, N. Tolstik, K. I. Schaffers, and I. T. Sorokina, "Femtosecond SESAM-modelocked Cr:ZnS laser," Optics Express **20**, 28947 (2012).
43. N. Tolstik, E. Sorokin, and I. T. Sorokina, "Graphene mode-locked Cr:ZnS laser with 41 fs pulse duration," Optics Express **22**, 5564 (2014).
44. J. J. Adams, C. Bibeau, R. H. Page, D. M. Krol, L. H. Furu, and S. A. Payne, "4.0-4.5 mm lasing of Fe:ZnSe below 180 K, a new mid-infrared laser material," Optics Letters **24**, 1720 (1999).
45. J. Kernal, V. V. Fedorov, A. Gallian, S. B. Mirov, and V. V. Badikov, "Room temperature 3.9-4.5 μm gain-switched lasing of Fe:ZnSe," in *Advanced Solid State Photonics*, (OSA, 2006), paper MD6.
46. A. A. Voronov, Kozlovsky, V. I., Korostelin, Yu. V., Landman, A. I., Podmar'kov, Yu.P., Skasyrsky, Ya.K., Frolov M. P., "A continuous-wave Fe2+:ZnSe laser," Quantum Electronics **38**, 1113 (2008).

47. A. Sennaroglu, *Photonics and laser engineering : principles, devices, and applications*. New York: McGraw-Hill, 2010.

48. P. F. Moulton, "An Investigation of the Co:MgF_2 Laser System," IEEE Journal of Quantum Electronics **21**, 1582 (1985).

49. G. Steinmeyer, D. H. Sutter, L. Gallmann, N. Matuschek, and U. Keller, "Frontiers in ultrashort pulse generation: Pushing the limits in linear and nonlinear optics," Science **286**, 1507 (1999).

50. U. Keller, "Recent developments in compact ultrafast lasers," Nature **424**, 831 (2003).

51. Z. Sun, T. Hasan, and A. C. Ferrari, "Ultrafast lasers mode-locked by nanotubes and graphene," Physica E: Low-dimensional Systems and Nanostructures **44**, 1082 (2012).

52. U. Keller, K. J. Weingarten, F. X. Kartner, D. Kopf, B. Braun, I. D. Jung, R. Fluck, C. Hönninger, N. Matuschek, and J. A. d. Au, "Semiconductor saturable absorber mirrors (SESAM's) for femtosecond to nanosecond pulse generation in solid-state lasers," IEEE Journal of Selected Topics in Quantum Electronics **2**, 435 (1996).

53. H. A. Haus, "Mode-locking of lasers," IEEE Journal of Selected Topics in Quantum Electronics **6**, 1173 (2000).

54. O. E. Martinez, R. L. Fork, and J. P. Gordon, "Theory of passively mode-locked lasers including self-phase modulation and group-velocity dispersion," Optics Letters **9**, 156 (1984).

55. R. L. Fork, C. H. B. Cruz, P. C. Becker, and C. V. Shank, "Compression of optical pulses to six femtoseconds by using cubic phase compensation," Optics Letters **12**, 483 (1987).

56. J. M. Dawlaty, S. Shivaraman, M. Chandrashekhar, F. Rana, and M. G. Spencer, "Measurement of ultrafast carrier dynamics in epitaxial graphene," Applied Physics Letters **92**, 042116 (2008).

57. C. C. Lee, J. M. Miller, and T. R. Schibli, "Doping-induced changes in the saturable absorption of monolayer graphene," Applied Physics B: Lasers and Optics **108**, 129 (2012).

58. T. R. Schibli, E. R. Thoen, F. X. Kärtner, and E. P. Ippen, "Suppression of Q-switched mode locking and break-up into multiple pulses by inverse saturable absorption," Applied Physics B: Lasers and Optics **70**, S41 (2000).

59. A. Sennaroglu, U. Demirbas, S. Ozharar, and F. Yaman, "Accurate determination of saturation parameters for Cr^{4+}-doped solid-state saturable absorbers," Journal of the Optical Society of America B-Optical Physics **23**, 241 (2006).

60. L. D. DeLoach, R. H. Page, G. D. Wilke, S. A. Payne, and W. F. Krupke, "Transition Metal-Doped Zinc Chalcogenides Spectroscopy and Laser

Demonstration of a New Class of Gain Media," IEEE Journal of Quantum Electronics **32**, 885 (1996).

61. U. Demirbas and A. Sennaroglu, "Intracavity-pumped Cr^{2+}: ZnSe laser with ultrabroad tuning range between 1880 and 3100 nm," Optics Letters **31**, 2293 (2006).
62. A. Sennaroglu, U. Demirbas, A. Kurt, and M. Somer, "Direct experimental determination of the optimum chromium concentration in continuous-wave Cr2+: ZnSe lasers," IEEE Journal of Selected Topics in Quantum Electronics **13**, 823 (2007).
63. G. J. Wagner, T. J. Carrig, R. H. Page, K. I. Schaffers, J. Ndap, X. Ma, and A. Burger, "Continuous-wave broadly tunable Cr^{2+}:ZnSe laser," Optics Letters **24**, 19 (1999).
64. A. Sennaroglu, A. O. Konca, and C. R. Pollock, "Continuous-Wave Power Performance of a 2.47 μm Cr^{2+}: ZnSe Laser: Experiment and Modeling," IEEE Journal of Quantum Electronics **36**, 1199 (2000).
65. I. T. Sorokina, E. Sorokin, A. Di Lieto, M. Tonelli, R. H. Page, and K. I. Schaffers, "0.5 W efficient broadly tunable continuous-wave Cr2+: ZnSe laser," Advanced Solid State Lasers **34**, 188 (2000).
66. A. D. Lieto and M.Tonelli, "Development of a cw polycrystalline Cr^{2+}:ZnSe laser," Optics and Lasers in Engineering **39**, 305 (2001).
67. E. Sorokin, I. T. Sorokina, A. Di Lieto, M. Tonelli, and R. H. Page, "Tunable diode-pumped continuous-wave single crystal and ceramic Cr2+: ZnSe lasers," Cleo(R)/Pacific Rim 2001, Postdeadline Paper 26 (2001).
68. E. Sorokin, I. T. Sorokina, and R. H. Page, "Room-temperature CW diode-pumped Cr^{2+}:ZnSe laser," in *Advanced Solid State Photonics*, (OSA, 2001), paper 101.
69. I. T. Sorokina, E. Sorokin, A. D. Lieto, M. Tonelli, R. H. Page, and K. I. Schaffers, "Efficient broadly tunable continuous-wave Cr^{2+}:ZnSe laser," Journal of the Optical Society of America B **18**, 926 (2001).
70. E. Sorokin and I. T. Sorokina, "Tunable diode-pumped continuous-wave Cr2+: ZnSe laser," Applied Physics Letters **80**, 3289 (2002).
71. U. Demirbas, A. Sennaroglu, N. Vermeulen, H. Ottevaere, and H. Thienpont, "Continuous-Wave Fiber-Pumped Cr:ZnSe Laser," in *Conference on Solid-State Lasers and Amplifiers II, Photonics Europe*, (2006), paper 6190-10.
72. I. T. Sorokina, E. Sorokin, T. J. Carrig, and K. I. Scaffers, "A SESAM passively mode-locked Cr:ZnSe laser," in *Advanced Solid-State Photonics*, (Optical Society of America, 2006), paper TuA4.
73. I. T. Sorokina, "Broadband Mid-Infrared Solid-State Lasers," in *Mid-Infrared Coherent Sources and Applications*, M. Ebrahim-Zadeh and I. T. Sorokina, Eds., ed: Springer, 2007, pp. 225.

74. M. N. Cizmeciyan, H. Cankaya, A. Kurt, and A. Sennaroglu, "Operation of femtosecond Kerr-lens mode-locked Cr:ZnSe lasers with different dispersion compensation methods," Applied Physics B: Lasers and Optics **106**, 887 (2012).
75. T. Hasan, Z. Sun, F. Wang, F. Bonaccorso, P. H. Tan, A. G. Rozhin, and A. C. Ferrari, "Nanotube–Polymer Composites for Ultrafast Photonics," Advanced Materials **21**, 3874 (2009).
76. S. Y. Set, H. Yaguchi, Y. Tanaka, and M. Jablonski, "Ultrafast fiber pulsed lasers incorporating carbon nanotubes," IEEE Journal of Selected Topics in Quantum Electronics **10**, 137 (2004).
77. I. H. Baek, S. Y. Choi, H. W. Lee, W. B. Cho, V. Petrov, A. Agnesi, V. Pasiskevicius, D. I. Yeom, K. Kim, and F. Rotermund, "Single-walled carbon nanotube saturable absorber assisted high-power mode-locking of a Ti:sapphire laser," Optics Express **19**, 7833 (2011).
78. A. Schmidt, P. Koopmann, G. Huber, P. Fuhrberg, S. Y. Choi, D.-I. Yeom, F. Rotermund, V. Petrov, and U. Griebner, "175 fs Tm:Lu2O3 laser at 2.07 µm mode-locked using single-walled carbon nanotubes," Optics Express **20**, 5313 (2012).
79. B. V. Cunning, C. L. Brown, and D. Kielpinski, "Low-loss flake-graphene saturable absorber mirror for laser mode-locking at sub-200-fs pulse duration," Applied Physics Letters **99**, 261109 (2011).
80. I. H. Baek, H. W. Lee, S. Bae, B. H. Hong, Y. H. Ahn, D.-I. Yeom, and F. Rotermund, "Efficient Mode-Locking of Sub-70-fs Ti:Sapphire Laser by Graphene Saturable Absorber," Applied Physics Express **5**, 032701 (2012).
81. W. B. Cho, J. W. Kim, H. W. Lee, S. Bae, B. H. Hong, S. Y. Choi, I. H. Baek, K. Kim, D.-I. Yeom, and F. Rotermund, "High-quality, large-area monolayer graphene for efficient bulk laser mode-locking near 1.25 um," Optics Letters **36**, 4089 (2011).
82. J. Ma, G. Q. Xie, P. Lv, W. L. Gao, P. Yuan, L. J. Qian, H. H. Yu, H. J. Zhang, J. Y. Wang, and D. Y. Tang, "Graphene mode-locked femtosecond laser at 2 um wavelength," Optics Letters **37**, 2085 (2012).
83. F. Bonaccorso, Z. Sun, T. Hasan, and A. C. Ferrari, "Graphene photonics and optoelectronics," Nature photonics **4**, 611 (2010).
84. A. C. Ferrari, J. C. Meyer, V. Scardaci, C. Casiraghi, M. Lazzeri, F. Mauri, S. Piscanec, D. Jiang, K. S. Novoselov, S. Roth, and A. K. Geim, "Raman Spectrum of Graphene and Graphene Layers," Physical Review Letters **97**, 187401 (2006).
85. A. Reina, X. Jia, J. Ho, D. Nezich, H. Son, V. Bulovic, M. S. Dresselhaus, and J. Kong, "Large Area, Few-Layer Graphene Films on Arbitrary Substrates by Chemical Vapor Deposition," Nano Letters **9**, 30 (2008).
86. M. Bass, *Handbook of Optics*, 2nd Edition ed. vol. 2: McGraw-Hill, 1994.

87. K. S. Novoselov, A. K. Geim, S. V. Morozov, D. Jiang, Y. Zhang, S. V. Dubonos, I. V. Grigorieva, and A. A. Firsov, "Electric field effect in atomically thin carbon films," Science **306**, 666 (2004).
88. K. Novoselov, A. Geim, S. Morozov, D. Jiang, Y. Zhang, S. Dubonos, I. Grigorieva, and A. Firsov, "Electric field effect in atomically thin carbon films," Science **306**, 666 (2004).
89. A. Geim, "Graphene: status and prospects," Science **324**, 1530 (2009).
90. P. Avouris, Z. Chen, and V. Perebeinos, "Carbon-based electronics," Nature Nanotechnology **2**, 605 (2007).
91. K. F. Mak, M. Y. Sfeir, Y. Wu, C. H. Lui, J. A. Misewich, and T. F. Heinz, "Measurement of the Optical Conductivity of Graphene," Physical Review Letters **101**, 196405 (2008).
92. A. C. Ferrari and D. M. Basko, "Raman spectroscopy as a versatile tool for studying the properties of graphene," Nature Nanotechnology **8**, 235 (2013).
93. L. M. Malard, M. A. Pimenta, G. Dresselhaus, and M. S. Dresselhaus, "Raman spectroscopy in graphene," Physics Reports **473**, 51 (2009).
94. M. Breusing, S. Kuehn, T. Winzer, E. Malić, F. Milde, N. Severin, J. P. Rabe, C. Ropers, A. Knorr, and T. Elsaesser, "Ultrafast nonequilibrium carrier dynamics in a single graphene layer," Physical Review B **83**, 153410 (2011).
95. S. Berciaud, S. Ryu, L. E. Brus, and T. F. Heinz, "Probing the Intrinsic Properties of Exfoliated Graphene: Raman Spectroscopy of Free-Standing Monolayers," Nano Letters **9**, 346 (2008).
96. C. Casiraghi, "Doping dependence of the Raman peaks intensity of graphene close to the Dirac point," Physical Review B **80**, 233407 (2009).
97. A. Das, S. Pisana, B. Chakraborty, S. Piscanec, S. K. Saha, U. V. Waghmare, K. S. Novoselov, H. R. Krishnamurthy, A. K. Geim, A. C. Ferrari, and A. K. Sood, "Monitoring dopants by Raman scattering in an electrochemically top-gated graphene transistor," Nature Nanotechnology **3**, 210 (2008).
98. M. Liu, X. Yin, E. Ulin-Avila, B. Geng, T. Zentgraf, L. Ju, F. Wang, and X. Zhang, "A graphene-based broadband optical modulator," Nature **474**, 64 (2011).
99. E. O. Polat and C. Kocabas, "Broadband Optical Modulators Based on Graphene Supercapacitors," Nano Letters **13**, 5851 (2013).
100. J. Yoo, K. Balakrishnan, J. Huang, V. Meunier, B. Sumpter, A. Srivastava, M. Conway, A. Reddy, J. Yu, R. Vajtai, and P. Ajayan, "Ultrathin planar graphene supercapacitors," Nano Letters **11**, 1423 (2011).
101. Y. Zhu, S. Murali, M. Stoller, K. Ganesh, W. Cai, P. Ferreira, A. Pirkle, R. Wallace, K. Cychosz, M. Thommes, D. Su, E. Stach, and R. Ruoff, "Carbon-based supercapacitors produced by activation of graphene," Science **332**, 1537 (2011).

102. K. S. Kim, Y. Zhao, H. Jang, S. Y. Lee, J. M. Kim, K. S. Kim, J.-H. Ahn, P. Kim, J.-Y. Choi, and B. H. Hong, "Large-scale pattern growth of graphene films for stretchable transparent electrodes," Nature **457**, 706 (2009).

103. M.-M. Huang, Y. Jiang, P. Sasisanker, G. W. Driver, and H. Weingärtner, "Static Relative Dielectric Permittivities of Ionic Liquids at 25 °C," Journal of Chemical & Engineering Data **56**, 1494 (2011).

104. S. Yumeng, D. Xiaochen, C. Peng, W. Junling, and L. Lain-Jong, "Effective doping of single-layer graphene from underlying SiO2 substrates," Physical Review B **79**, 115402 (2009).

105. S. Ozharar, I. Baylam, M. N. Cizmeciyan, O. Balci, E. Pince, C. Kocabas, and A. Sennaroglu, "Graphene mode-locked multipass-cavity femtosecond Cr4+: forsterite laser," Journal of Optical Society of America B **30**, 1270 (2013).

106. I. Baylam, S. Ozharar, M. N. Cizmeciyan, O. Balci, E. Pince, C. Kocabas, and A. Sennaroglu, "Femtosecond Pulse Generation from an Extended Cavity Cr4+:forsterite Laser using Graphene on YAG," in *Advanced Solid-State Lasers*, (2013), paper ATh3A.8.

107. R. M. Lynden-Bell, A. I. Frolov, and M. V. Fedorov, "Electrode screening by ionic liquids," Physical Chemistry Chemical Physics **14**, 2693 (2012).

108. L. M. Malard, K. F. Mak, A. H. C. Neto, N. M. R. Peres, and T. F. Heinz, "Observation of intra- and inter-band transitions in the transient optical response of graphene," New Journal of Physics **15**, (2013).

109. I. Baylam, M. N. Cizmeciyan, S. Ozharar, E. O. Polat, C. Kocabas, and A. Sennaroglu, "Graphene Supercapacitor as a Voltage Controlled Saturable Absorber for Femtosecond Pulse Generation," in *CLEO: 2014*, (Optical Society of America, 2014), paper STu1E.2.

110. D. R. Larson, W. R. Zipfel, R. M. Williams, S. W. Clark, M. P. Bruchez, F. W. Wise, and W. W. Webb, "Water-Soluble Quantum Dots for Multiphoton Fluorescence Imaging in Vivo," Science **300**, 1434 (2003).

111. X. Michalet, F. F. Pinaud, L. A. Bentolila, J. M. Tsay, S. Doose, J. J. Li, G. Sundaresan, A. M. Wu, S. S. Gambhir, and S. Weiss, "Quantum Dots for Live Cells, in Vivo Imaging, and Diagnostics," Science **307**, 538 (2005).

112. D. Loss and D. P. DiVincenzo, "Quantum computation with quantum dots," Physical Review A **57**, 120 (1998).

113. V. I. Klimov, A. A. Mikhailovsky, S. Xu, A. Malko, J. A. Hollingsworth, C. A. Leatherdale, H. J. Eisler, and M. G. Bawendi, "Optical Gain and Stimulated Emission in Nanocrystal Quantum Dots," Science **290**, 314 (2000).

114. H. Azzazy, M. Mansour, and S. Kazmierczak, "From diagnostics to therapy: prospects of quantum dots," Clinical biochemistry **40**, 917 (2007).

115. Y. He, Y. Zhong, Y. Su, Y. Lu, Z. Jiang, F. Peng, T. Xu, S. Su, Q. Huang, C. Fan, and S.-T. Lee, "Water-dispersed near-infrared-emitting quantum dots of ultrasmall sizes for in vitro and in vivo imaging," Angewandte Chemie (International ed. in English) **50**, 5695 (2011).
116. H. Mansur, "Quantum dots and nanocomposites," Wiley interdisciplinary reviews. Nanomedicine and nanobiotechnology **2**, 113 (2010).
117. W. Jiang, A. Singhal, J. Zheng, C. Wang, and W. C. W. Chan, "Optimizing the Synthesis of Red- to Near-IR-Emitting CdS-Capped CdTexSe1-x Alloyed Quantum Dots for Biomedical Imaging," Chemistry of Materials **18**, 4845 (2006).
118. G. Asim, K. R. Arup, and J. P. Amlan, "To make polymer: Quantum dot hybrid solar cells NIR-active by increasing diameter of PbS nanoparticles," Solar Energy Materials and Solar Cells **95**, 651 (2011).
119. W. Jiang, A. Singhal, B. Y. S. Kim, J. Zheng, J. T. Rutka, C. Wang, and W. C. W. Chan, "Assessing Near-Infrared Quantum Dots for Deep Tissue, Organ, and Animal Imaging Applications," Journal of the Association for Laboratory Automation **13**, 6 (2008).
120. L. Guo-Xi, G. Miao-Miao, Z. Jian-Rong, and Z. Jun-Jie, "Preparation and bioapplication of high-quality, water-soluble, biocompatible, and near-infrared-emitting CdSeTe alloyed quantum dots," Nanotechnology **20**, 415103 (2009).
121. H. Chen, S. Cui, Z. Tu, J. Ji, J. Zhang, and Y. Gu, "Characterization of CdHgTe/CdS QDs for Near Infrared Fluorescence Imaging of Spinal Column in a Mouse Model," Photochemistry and Photobiology **87**, 72 (2011).
122. B. Blackman, D. Battaglia, and X. Peng, "Bright and Water-Soluble Near IR-Emitting CdSe/CdTe/ZnSe Type-II/Type-I Nanocrystals, Tuning the Efficiency and Stability by Growth," Chemistry of Materials **20**, 4847 (2008).
123. R. Aswathy, Y. Yoshida, T. Maekawa, and D. S. Kumar, "Near-infrared quantum dots for deep tissue imaging," Analytical and Bioanalytical Chemistry **397**, 1417 (2010).
124. Y.-P. Gu, R. Cui, Z.-L. Zhang, Z.-X. Xie, and D.-W. Pang, "Ultrasmall Near-Infrared Ag2Se Quantum Dots with Tunable Fluorescence for in Vivo Imaging," Journal of the American Chemical Society **134**, 79 (2011).
125. I. Hocaoglu, M. N. Cizmeciyan, R. Erdem, C. Ozen, A. Kurt, A. Sennaroglu, and H. Y. Acar, "Development of highly luminescent and cytocompatible near-IR-emitting aqueous Ag2S quantum dots," Journal of Materials Chemistry **22**, 14674 (2012).
126. A. F. E. Hezinger, J. Teßmar, and A. Göpferich, "Polymer coating of quantum dots – A powerful tool toward diagnostics and sensorics," European Journal of Pharmaceutics and Biopharmaceutics **68**, 138 (2008).

127. W. S. Pelouch, G. J. Wagner, T. J. Carrig, and W. J. Scharpf, "Mid-Wave ZGP OPOs pumped by a Cr:ZnSe laser," in *Advanced Solid State Photonics*, (OSA, 2001), paper 670.

128. C. Fischer, E. Sorokin, I. T. Sorokina, and M. W. Sigrist, "Photoacoustic monitoring of gases using a novel laser source tunable around 2.5 μm," Optics and Lasers in Engineering **43**, 573 (2005).

129. H. Cankaya, U. Demirbas, A. K. Erdamar, and A. Sennaroglu, "Absorption saturation analysis of Cr2+: ZnSe and Fe2+: ZnSe," Journal of the Optical Society of America B-Optical Physics **25**, 794 (2008).

130. I. S. Moskalev, V. V. Fedorov, and S. B. Mirov, "Tunable, single-frequency, and multi-watt continuous-wave Cr2+: ZnSe lasers," Optics Express **16**, 4145 (2008).

131. P. Maine, D. Strickland, P. Bado, M. Pessot, and G. Mourou, "Generation of ultrahigh peak power pulses by chirped pulse amplification," IEEE Journal of Quantum Electronics **24**, 398 (1988).

132. M. Pessot, J. Squier, P. Bado, G. Mourou, and D. J. Harter, "Chirped pulse amplification of 300 fs pulses in an alexandrite regenerative amplifier," IEEE Journal of Quantum Electronics **25**, 61 (1989).

133. P. J. Delfyett, A. Yusim, S. Grantham, S. Gee, K. Gabel, M. Richardson, G. Alphonse, and J. Connolly, "Ultrafast semiconductor laser-diode-seeded Cr:LiSAF regenerative amplifier system," Applied Optics **36**, 3375 (1997).

134. M. D. Perry, D. Strickland, T. Ditmire, and F. G. Patterson, "Cr:LiSrAlF6 regenerative amplifier," Optics Letters **17**, 604 (1992).

135. C. P. J. Barty, T. Guo, C. Le Blanc, F. Raksi, C. Rose-Petruck, J. Squier, K. R. Wilson, V. V. Yakovlev, and K. Yamakawa, "Generation of 18-fs, multiterawatt pulses by regenerative pulse shaping and chirped-pulse amplification," Optics Letters **21**, 668 (1996).

136. M. Aoyama, K. Yamakawa, Y. Akahane, J. Ma, N. Inoue, H. Ueda, and H. Kiriyama, "0.85-PW, 33-fs Ti:sapphire laser," Optics Letters **28**, 1594 (2003).

137. G. Jonusauskas, J. Oberlé, and C. Rullière, "54-fs, 1-GW, 1-kHz pulse amplification in Cr:forsterite," Optics Letters **23**, 1918 (1998).

138. J. M. Evans, V. Petricevic, R. R. Alfano, and Q. Fu, "Kilohertz Cr:forsterite regenerative amplifier," Optics Letters **23**, 1692 (1998).

139. J. M. Evans, V. Petricevic, A. Delgado, R. R. Alfano, and F. Qiang, "Kilohertz Cr:forsterite regenerative amplifier," in *Conference on Lasers and Electro-Optics*, (1996), paper 127.

140. V. Shcheslavskiy, Noack, F., Petrov, V., Zhavoronkov N., "Femtosecond Regenerative Amplification in Cr:Forsterite," Applied Optics **38**, (1999).

VITA

M. Natali Çizmeciyan Sözüdoğru was born in Şişli, İstanbul on April 27, 1984. She received her BS degree in Physics from Marmara University in 2007. During her undergraduate studies, in 2005 and 2006, she also worked as a research assistant in the Laser Research Laboratory at Koç University. After graduating from the Master of Science program in Material Science and Engineering, in 2009, she was admitted to the doctorate program in same field at Koç University. Her research interests include mid-infrared solid-state lasers and non-linear optical spectroscopy of different materials.

List of Publications:

Published Journal Articles

1. H. Kalaycioglu, H. Cankaya, M. N. Cizmeciyan, A. Sennaroglu, and G. Ozen, "Spectroscopic investigation of Tm^{3+}: TeO_2-WO_3 glass," Journal of Luminescence **128**, 1501 (2008).
2. M. N. Cizmeciyan, H. Cankaya, A. Kurt, and A. Sennaroglu, "Kerr-lens mode-locked femtosecond Cr^{2+}:ZnSe laser at 2420 nm," Optics Letters **34**, 3056 (2009).
3. H. Cankaya, M. N. Cizmeciyan, E. Beyatli, A. T. Gorgulu, A. Kurt, and A. Sennaroglu, "Injection-seeded, gain-switched tunable Cr:ZnSe laser," Optics Letters **37**, 136 (2012).

4. M. N. Cizmeciyan, H. Cankaya, A. Kurt, and A. Sennaroglu, "Operation of femtosecond Kerr-lens mode-locked Cr:ZnSe lasers with different dispersion compensation methods," Applied Physics B-Lasers and Optics **106**, 887 (2012).

5. I. Hocaoglu, M. N. Cizmeciyan, R. Erdem, C. Ozen, A. Kurt, A. Sennaroglu, and H. Y. Acar, "Development of highly luminescent and cytocompatible near-IR-emitting aqueous Ag_2S quantum dots," Journal of Materials Chemistry **22**, 14674 (2012).

6. M. N. Cizmeciyan, J. W. Kim, S. Bae, B. H. Hong, F. Rotermund, and A. Sennaroglu, "Graphene mode-locked femtosecond Cr:ZnSe laser at 2500nm," Optics Letters **38**, 341 (2013).

7. S. Ozharar, I. Baylam, M. N. Cizmeciyan, O. Balci, E. Pince, C. Kocabas, and A. Sennaroglu, "Graphene mode-locked multipass-cavity femtosecond Cr^{4+}: forsterite laser," J. Opt. Soc. Am. B **30**, 1270 (2013).

8. I. Baylam, M. N. Cizmeciyan, S. Ozharar, E. O. Polat, C. Kocabas, and A. Sennaroglu, “Femtosecond pulse generation with a voltage controlled graphene saturable absorber,” Optics Letters, in press (2014).

Conference Proceedings

1. A. Sennaroglu, U. Demirbas, H. Cankaya, N. Cizmeciyan, A. Kurt, and M. Somer, "Chromium-doped zinc selenide gain media: from synthesis to pulsed mid-infrared laser operation," in SPIE Proceedings, (2010), paper 75981B.

2. M. N. Cizmeciyan, H. Cankaya, A. Kurt, and A. Sennaroglu, "Dispersion compensation schemes for femtosecond Kerr-lens mode-locked Cr:ZnSe lasers," in Advances in Optical Materials, (Optical Society of America, 2011), paper AMB1.

3. H. Cankaya, M. N. Cizmeciyan, E. Beyatli, A. T. Gorgulu, A. Kurt, and A. Sennaroglu, "Injection-seeded, narrow-line gain-switched Cr:ZnSe laser," in Lasers, Sources, and Related Photonic Devices, (Optical Society of America, 2012), paper AW4A.27.

4. I. Baylam, S. Ozharar, M. N. Cizmeciyan, O. Balci, E. Pince, C. Kocabas, and A. Sennaroglu, "Femtosecond Pulse Generation from an Extended Cavity Cr^{4+}:forsterite Laser using Graphene on YAG," in Advanced Solid-State Lasers Congress, (Optical Society of America, 2013), paper ATh3A.8.

5. M. N. Cizmeciyan, J. W. Kim, S. Bae, B. H. Hong, F. Rotermund, and A. Sennaroglu, "Graphene mode-locked Cr:ZnSe laser," in Advanced Solid-State Lasers Congress, (Optical Society of America, 2013), paper MW1C.4.

6. I. Baylam, M. N. Cizmeciyan, S. Ozharar, E. O. Polat, C. Kocabas, and A. Sennaroglu, "Graphene Supercapacitor as a Voltage Controlled Saturable Absorber for Femtosecond Pulse Generation," in CLEO: 2014, OSA Technical Digest (online) (Optical Society of America, 2014), paper STu1E.2.